Review

Hydrophobic and Tribological Properties of Biomimetic Interfaces

Kang Yang [1,2], Jun Tang [1,2,3,*], Jia Huang [4], Honglei Zhang [1,3], Hao Chen [1,2], Yahui Xiong [1,2,3], Ruili Wang [5], Chao Wu [1,2,3], Meimei Wang [1,2] and Hongliang Chen [1,2]

1   Department of Mechanical Engineering, Anyang Institute of Technology, Avenue West of Yellow River, Anyang 455000, China; angongyangkang@163.com (K.Y.); 13643602974@163.com (H.Z.); 18037676793@163.com (H.C.); yahui1228@foxmail.com (Y.X.); w2304262838@163.com (C.W.); wmmscau@163.com (M.W.); 19711097223@163.com (H.C.)
2   Key Laboratory of Functional Materials and Remanufacturing Technology of Aviation Equipments, Anyang Institute of Technology, Avenue West of Yellow River, Anyang 455000, China
3   School of Mechanical Engineering, Sichuan University of Science & Engineering, 180 # Xueyuan Street, Huixing Road, Zigong 643000, China
4   Department of Aeronautics and Astronautics, Nanchang Institute of Technology, Nanchang 330044, China; chenjingjingfzu@126.com
5   Faculty of Engineering, Huanghe Science and Technology University, Zhengzhou 450000, China; 201309111@hhstu.edu.cn
*   Correspondence: 18010708257@163.com; Tel./Fax: +86-372-2986271

Abstract: Bionic interfaces have received much attention owing to their attractive hydrophobic and tribological potential. Although a great deal of research has been carried out on biomimetic nanostructures, the basic theory, experimental application, and related techniques of hydrophobicity of biomimetic nanostructures, as well as the relationship between the state of lubricants and friction in tribology have not been fully explored. In this review, based on a brief discussion of the theory of hydrophobicity, the role of two-dimensional bionic structures in the wet state is introduced, and the wetting mechanism and applications are discussed. Then, the synergistic effects and mechanisms of bionic weaving and lubricants in the dry/wet friction state are investigated. In addition, the contribution of bionic structures to the fields of hydrophobicity and tribology further deepens the knowledge and enriches the practical applications of bionic surface weaving.

Keywords: biomimetic interfaces; hydrophobicity; tribology
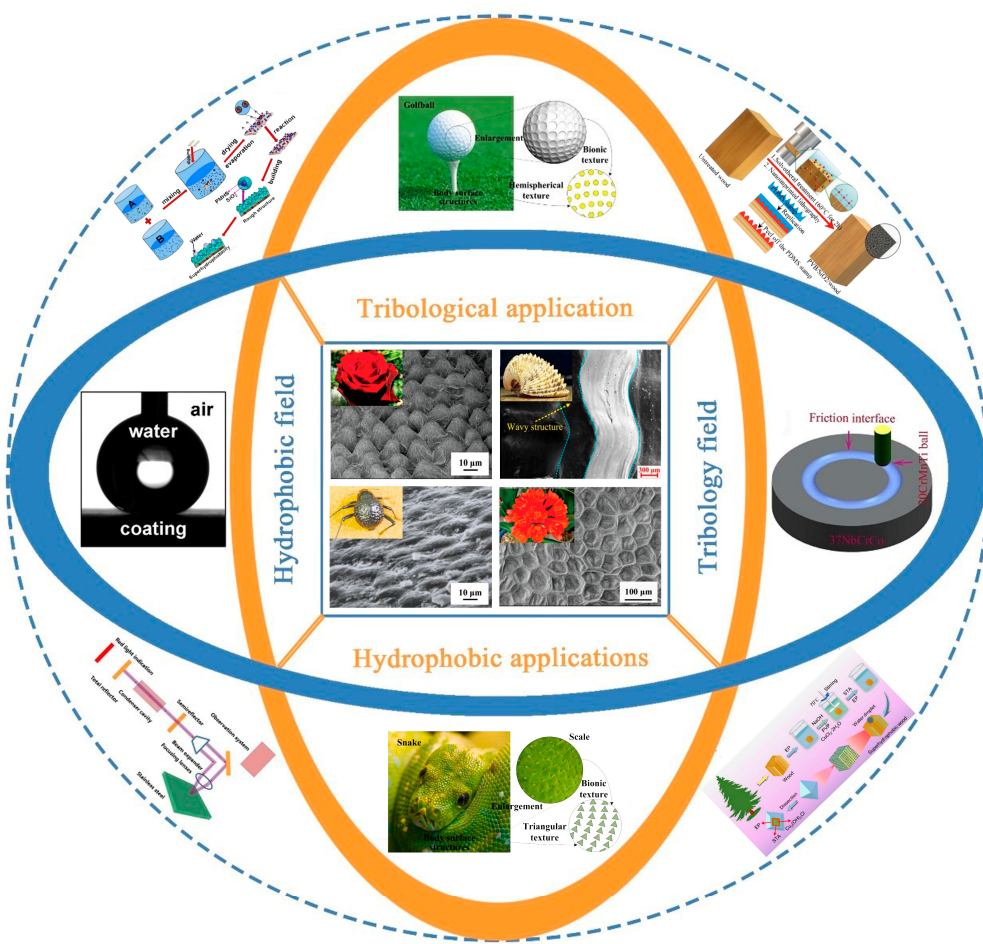
1. Introduction

As one of the most interesting science topics, bionics is an interdisciplinary subject that combines biology and technology [1–5]. According to relevant research, plants and animals have evolved over hundreds of millions of years, not only perfectly adapting to nature but also approaching perfection. Bionics attempts to solve technical problems by mimicking the functions of animals and plants in nature in terms of technology [6,7]. By reproducing the principles of biology, humans have not only discovered technical solutions but also solutions perfectly suited to nature's requirements. The surfaces of many plants and animals have evolved very specific structural forms, which have given them excellent and unique functions [8–10]. Examples include the self-cleaning properties of the surface of lotus leaves [11,12], the capability of geckos to walk freely on the walls [13–15], and the low-energy coating on the shark skin [16,17]. These unique and excellent functions enable plants and animals to survive and reproduce in the midst of the brutal competition in nature, which attracted extensive interest from researchers.

In general, the wettability and adhesion of a solid surface are determined by combining the chemical composition of the solid surface and the surface morphological structure [18,19]. Therefore, the modulation of wettability and adhesion can be achieved by changing the

chemical composition of the solid surface and the surface microstructure [20,21]. As shown in Figure 1, inspired by the 'lotus leaf effect' [20,22–25] and the 'rose effect' [26,27], the constructed superhydrophobic surface exhibits exceptional wettability and has emerged as a prominent research area in the current scientific frontier. With the development of research on super-hydrophobic surfaces, the classification of their states has been extended to four categories: the Young state, the Wenzel state [28], the Cassie state [29], and the transition state between Wenzel and Cassie [30]. The comprehension of diverse states is advantageous for the development of a surface capable of repelling water droplets and maintaining durability, thereby broadening the scope of application for superhydrophobic surfaces in both industrial and domestic settings [31,32].

Figure 1. Typical model of the morphology and application of bionanostructures in hydrophobic and friction fields [33–39].

Surface weaving techniques have attracted extensive attention due to their potential applications in hydrophobicity [40–42], tribology [43–45], adhesion [46], and others [47–50] at the micro/nano scale. Friction and wear often exist in the moving parts of mechanical systems, and these lead to significant energy loss and the failure of mechanical components, thus affecting the efficiency and lifetime of equipment [51,52]. According to statistics, the proportion of losses caused by friction and wear in the gross national product of industrialized countries is increasing every year. Therefore, it is essential to reduce the friction and wear between mechanical components [53]. The surface microstructure of a material is essential for controlling its surface composition, structure, and interfacial properties, thereby reducing friction and extending wear life [37].

Surface texturing can be very effective in decreasing friction and wear owing to the hydrodynamic effects of wear debris trapping, liquid lubricant oil reservoirs, and increased

load capacity [54,55]. In recent years, another significant aspect of surface textured solid lubricant reservoir has been identified. Solid lubricants stored in the weave can be released to the sliding interface, thereby increasing the wear life of sliding surfaces [56,57]. The usage of efficient lubricants in solid or liquid form is the most common and effective way to improve tribological performance [58]. Additionally, superlubrication is a crucial method for addressing frictional wear, where the friction between two surfaces approaches zero [59].

Superlubrication was first proposed by Hirano and Shinjo in the 1990s as an important means of essentially solving the aforementioned frictional wear, where friction between two surfaces is close to zero [59]. Theoretically, owing to the interference of miscellaneous factors and the limitations of measurement, superlubricity can be achieved with near-zero frictional wear, and a coefficient of friction of 0.01 or less is considered to be superlubricity [60]. In recent years, scholars have approximated carefully prepared c-face friction to zero at disproportionate contact, which is also referred to as structural superlubricity [61]. Furthermore, work has been dedicated to designing special nanostructures to obtain macroscopic superlubricity properties. This has significant physical and technical implications for realizing low friction and wear between moving parts.

Advanced applications of bionanostructures in the good fields of hydrophobicity and tribology on material surfaces have not yet been summarized. In this article, we concentrate on the experiments and mechanisms of bionanostructures in hydrophobic and hydrophobic water. The full paper is divided into four parts as follows. In the first section, a brief background of bionanostructures in hydrophobics and tribology is presented. In the second section, the research progress of bionanostructures in the field of hydrophobicity is discussed. In addition, the third section describes the research progress of bionic structures in tribology. Finally, the fourth section provides a summary and outlook on bionanostructures in hydrophobicity and tribology.

2. Hydrophobic Biomimetic Interfaces

It has been observed that Lotus leaves [62], water striders [63], dragonflies [64], butterflies [65], and taro leaves [66] are naturally endowed with particular hydrophobic performances [62–66]. On the basis of this phenomenon, the concept of superhydrophobicity is artificially defined. Investigations into the structure and material composition of plants and animals have led to unprecedented enthusiasm and rapid development in the study of hydrophobic surfaces [67–69]. Water droplets easily roll on these surfaces when the contact angle exceeds 150° and the corresponding sliding angle is less than 10°, offering excellent performances such as water repellency [70], self-cleaning [71–73], and anti-icing [74]. Low-surface-energy materials and micro/nanostructures are essential to achieve the ultrahydrophobicity properties. Superhydrophobicity materials can be prepared by forming micro- and nanostructures on the surface of low-surface-energy substances or by modifying low-surface-energy materials on the surface of micro- and nanostructures [75,76]. However, the chemical modification typically has poor thermal stability and mechanical stability and is easy to be impaired in harsh environments. In addition, they also influence inherent characteristics such as the surface conductivity and the reflectivity of materials [77]. Therefore, the design of outstanding bionanostructured surfaces is of great interest to the hydrophobic field [78–80]. In this section, the first subsection systematically investigates wettability theory. The second subsection conducts experiments on hydrophobic surfaces by preparing bionanostructures. The third subsection explores the wetting mechanism of hydrophobic surfaces in detail, while the last subsection concludes with a summary of the applications of hydrophobic surfaces.
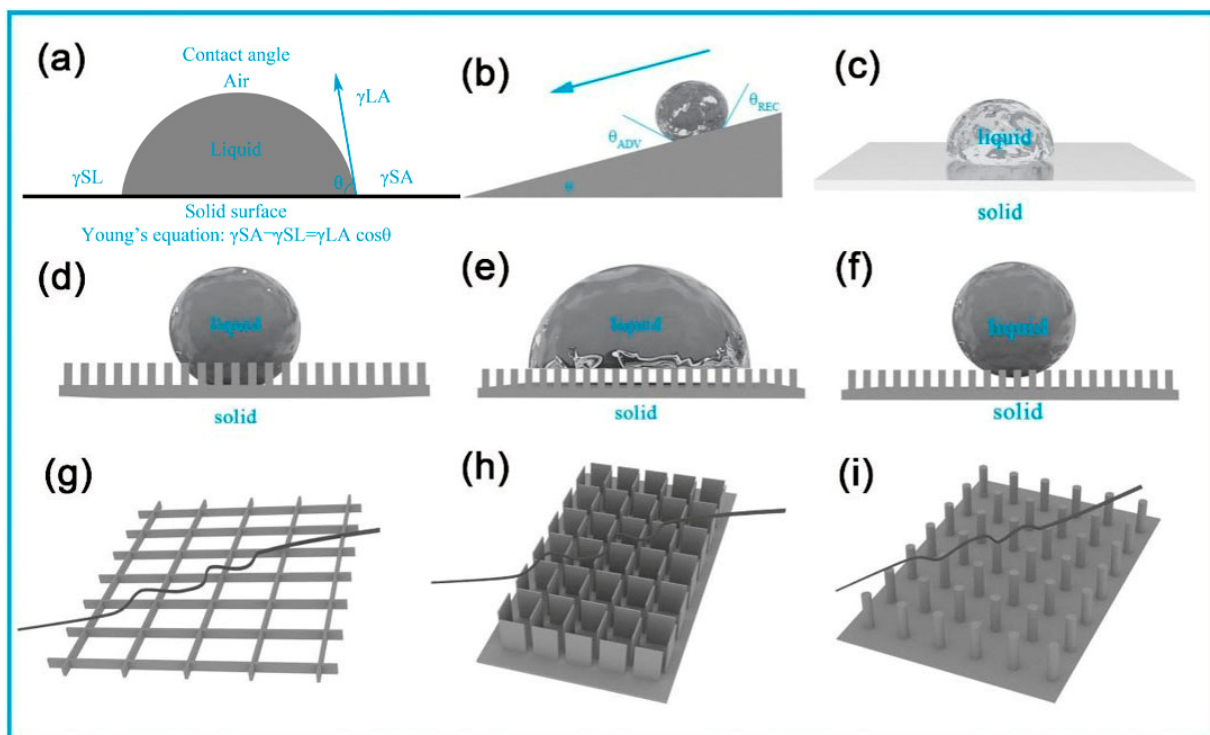
2.1. Theory of Hydrophobicity

Surface/interface is the transition region between phases in a multiphase system, in which the object it studies is the transition zone from one phase to another. Based on the different states of material aggregation, the surface/interface can be divided into the following five types: solid–gas, liquid–gas, solid–liquid, liquid–liquid, and solid–solid

interface. The transition areas of solid–gas and liquid–gas contact are called surfaces, while the physical transition zones of solid–liquid, liquid–liquid, and solid–solid contact are called interfaces. Surface and interface physicochemical phenomena occupy an important position in materials science. Due to the different physical structures and chemical compositions, the surface and interface of materials are significantly different from their internal bodies. Therefore, the study of surface–interface phenomena of materials is of great importance.

Furthermore, surface wettability is considered a crucial peculiarity of solid surfaces, which can represent the diffusion process of liquid on solid surfaces [81]. Numerous studies showed that the wettability of a solid surface was decided by its surface chemical composition, microscopic as well as macroscopic geometric structure [82,83]. Artificially adjusting and changing the chemical composition and surface morphology structure of a solid surface was the feasible strategy to transform the wettability of the solid surface. Furthermore, external influences such as light, heat, magnetic fields, heat and solvents also played a significant role in the wettability of solid surfaces.

At present, the wettability of solid materials is characterised by static contact angle (CA). As shown in Figure 2a, when the liquid dropped on the solid surface, when it was in equilibrium, tangent lines were made to the solid and liquid surfaces at the junction of solid–liquid–gas phases and the angle formed by the tangent lines was called static contact angle (θ). As shown in Table 1, four types of hydrophobic surfaces can be classified according to the magnitude of the static contact angle obtained on the surface of materials.

Figure 2. (**a**) Wetting behavior of horizontal surfaces; (**b**) wetting behavior of inclined surfaces; (**c–f**) the state of hydrophobic surfaces; (**g–i**) the state of the three-phase solid–liquid–gas contact section.

Table 1. Four types of hydrophobic surfaces.

Static Contact Angles	Infiltration Status	Surface	Illustrations
$\theta < 10°$	Complete wettability	Super hydrophilic surface	
$10° < \theta < 90°$	Wettability	Hydrophilic surface	
$90° < \theta < 150°$	Partial wettability	Hydrophobic surfaces	
$\theta > 150°$	Non-wettability	Superhydrophobic surfaces	

In addition, the wetting behavior of an inclined solid surface is usually expressed by sliding angle (SA, α) and contact angle hysteresis (CAH). The sliding angle is the minimum angle of inclination required for a droplet to be about to roll off the inclined surface when it is on the inclined surface. As shown in Figure 2b, the dynamic contact angle in front was referred to as the advancing contact angle (θ_{ADV}) and the dynamic contact angle behind was referred to as the receding contact angle (θ_{REC}). This difference between θ_{ADV} and θ_{REC} was the contact angle hysteresis ($\Delta\theta$) [84–87]. Generally speaking, the forward contact angle is greater than the backward contact angle. In general, the θ_{ADV} is larger than the θ_{REC}, and the CA of a solid surface is between the θ_{ADV} and θ_{REC}. The relationship between the CAH and the SA of a solid surface can be depicted by the following Equation (1) [88]:

$$mg(\sin \alpha)/w = \gamma_{LV}(\cos \theta_{REC} - \cos \theta_{ADV}) \tag{1}$$

Herein, m is the mass of the droplet, w is width of the droplet, g is the acceleration of gravity, α is the surface inclination angle required to make water droplets slide, γ_{LV} is the interfacial tension between liquid and gas. The equation shows that the magnitude of the CAH and SA of a solid surface reflects the adhesion of the solid surface to the liquid or the ease of droplet detachment from the solid surface [89,90]. Specifically, the reduction in CAH leads to a decrease in the SA [91]. The smaller values of these two parameters indicate that the droplet exhibits enhanced spreading on the solid surface, thereby facilitating its easy slide off the solid surface under external force. This is of great significance for some application fields, such as self-cleaning surfaces and droplet motion control.

Studies have shown that the force field of the molecules on the surface of the liquid is different from that of the molecules inside the liquid. The molecules in the liquid can cancel each other out because of the symmetrical forces of the same kind of molecules around them. However, unlike the internal molecules of the liquid, the liquid molecules in the surface layer are not completely surrounded by the same kind of molecules, and they are acted by both the internal molecules of the liquid and the gas molecules. At the gas–liquid interface, the gravitational force of gas molecules pointing to the gas phase is much smaller than that of molecules pointing to the inside of the liquid, so the force on the molecules at the gas–liquid interface is the gravitational force pointing to the inside of the liquid. If a molecule is moved from the inside of the liquid to the surface, the system will overcome the attraction between the molecules to perform work, which will increase the free enthalpy. On the contrary, when the molecules in the surface layer move into the liquid, the free enthalpy of the system will decrease. Because the system is more stable at low energy, the liquid surface always shows the phenomenon of automatic contraction.

As early as the 19th century, people started theoretical research on surface-wetting behavior. The essence of the wetting phenomenon is the interaction of solid, liquid, and gas interfaces, and this interaction is the result of the tension balance of these three interfaces. Figure 2g–i show two conditions in which the solid–liquid–gas three-phase contact section presents the curve: continuous (Figure 2g) and discontinuous (Figure 2h,i). If the contact line was continuous, the droplet did not roll easily on the solid surface and adhered easily

to the solid surface. If the contact line was discontinuous, the droplet rolled easily on the solid surface.

In 1804, British scientists such as Thomson Young first proposed the relationship between the static contact angle of an ideal solid surface (the surface of solid materials was absolutely smooth, and the chemical composition was consistent) and the surface tension (Young's equation) as exhibited in Equations (2)–(9) [92]:

$$\cos\theta_0 = (\gamma_{SV} - \gamma_{SL})/\gamma_{LV} \tag{2}$$

$$V = \frac{\pi R^3}{3}(1 - \cos\theta)^2(2 + \cos\theta) \tag{3}$$

$$S = 2\pi R^2(1 - \cos\theta) \tag{4}$$

$$G = \gamma_{LA}S - \pi(R\sin\theta)^2(\gamma_{SA} - \gamma_{SL}) \tag{5}$$

$$G = \left[\frac{9\pi V^2}{(1 - \cos\theta)(2 + \cos\theta)^2}\right]^{\frac{1}{3}} \times [2\gamma_{LA} - (\gamma_{SA} - \gamma_{SL})(1 + \cos\theta)] \tag{6}$$

$$\frac{dG}{d\theta} = \left[\frac{9\pi V^2}{(1 - \cos\theta)(2 + \cos\theta)^2}\right]^{\frac{1}{3}} \times (\gamma_{SA} - \gamma_{SL} - \gamma_{LA}\cos\theta)\sin\theta = 0 \tag{7}$$

$$\frac{dG}{d\theta} = 0 \tag{8}$$

$$(\gamma_{SA} - \gamma_{SL} - \gamma_{LA}\cos\theta) = 0 \tag{9}$$

Herein, θ is the CA of the solid surface; γ_{SV}, γ_{SL}, and γ_{LV} are the surface tension of solid–gas interface, solid–liquid interface, and liquid–gas interface, respectively; V is the volume of the droplet; R is the radius of the droplet; S is the area of contact between a droplet and air; and G is the Gibbs free energy of the droplet.

The contact angle can be utilized as a visual indicator to quantitatively assess the wetting behavior of a solid surface by a liquid, but it does not reflect the change in energy during the wetting process. From the point of view of energy, the energy of the surface atoms or molecules is always higher than the energy of the same atomic molecules inside, whether it is a solid or a liquid. In the case of liquids, there is always an attempt to reduce their surface area in order to reduce their total energy and, thus, put them in a more stable state. Thus, the surface properties of a solid or liquid are described quantitatively by its surface energy or surface tension. The formula verifies the correctness of Young's equation from the point of energy view.

It is generally accepted that surface energy is the work performed to increase the surface area of a solid or liquid per unit area at constant temperature and pressure. Surface tension and surface energy are numerically equivalent but have different meanings. Surface tension is for the action of the surface of a solid or liquid so that its surface area to reduce the unit length of the force. Both are indicated by the symbol γ. The contact process between liquid and solid is usually accompanied by the disappearance of two old interfaces and the formation of a new one. From a microscopic point of view, this is the result of a large number of molecules acting together in an attempt to decrease the total energy of the system. The process of wetting obeys the principle of energy minimisation. Thus, Equations (2)–(8) verify the correctness of Young's equation from an energy point of view.

Young's equation characterises the wetting behavior of the ideal solid surface. However, the ideal solid surface does not exist (Figure 2c); actual solid surfaces will possess a certain level of roughness. In 1936, the American scientist Wenzel further extended the application of Young's equation by proposing a wetting theory (Wenzel's theory) for rough solid surfaces [93]. As shown in Figure 2d, supposing that the structural size of a rough solid surface was smaller than the size of a water droplet, when the water droplet touched the solid surface, there was no air pocket between the droplet and the solid.

This type of solid interface was called a uniform interface; the contact angle of a water droplet at a uniform interface could be expressed by Wenzel's equation, as shown in Equations (10) and (11) [93–95]:

$$cos\theta = R_f cos\theta_0 \tag{10}$$

$$R_f = \frac{A_{SL}}{A_F} \tag{11}$$

Herein, θ is the contact angle value of the rough surface, θ_0 is the contact angle value of a smooth surface, R_f is the roughness factor, A_{SL} is the real solid–liquid area, A_F is a solid to its geometric projection area.

It can be inferred from Wenzel's equation that, for a material that is inherently hydrophobic ($\theta_0 > 90°$), augmenting the surface roughness R_f will make the surface more hydrophobic as the roughness factor R_f is a number greater than 1 [96]. For a material that is inherently hydrophilic ($\theta_0 < 90°$), augmenting the roughness of the surface will result in an increased hydrophilicity of the surface.

As Wenzel's theory supposes that the liquid is completely submerged within the rough structure of the solid surface and that a uniform solid–liquid interface is established beneath the liquid, the scope of application of Wenzel's formula was limited. In 1944, Cassie and Baxter further expanded Wenzel's theory. They assumed that the liquid droplet would not completely penetrate and soak into the rough structure of the surface but would be suspended above the rough structure so that a portion of the air pocket or air bubble would be bound between the solid and liquid surfaces, forming the composite solid–liquid–air interface, as shown in Figure 2e. The wettability of a rough solid surface in the Cassie wetting state can be described by the following Cassie-Baxter equation, as shown in Equations (12) and (13) [95,97–99]:

$$cos\theta = R_f cos\theta_0 - f_{LA}\left(R_f cos\theta_0 + 1\right) \tag{12}$$

$$f_{LA} \geq \frac{R_f cos\theta_0}{R_f cos\theta_0 + 1}(\theta_0 < 90°) \tag{13}$$

Herein, f_{LA} is the area percentage of the liquid–gas interface under a droplet in the whole structure. It can be deduced from Equation (11) that for a hydrophilic interface, the contact angle value increases with augmenting f_{LA}. If larger values of f_{LA} can be achieved, the surface can become super-sparse. However, there is also instability in the formation of air bubbles. Equation (12) shows that it makes a hydrophilic interface hydrophobic; the value of f_{LA} must satisfy Equation (13).

The conversion mechanism between Cassie and Wenzel is very important. This wetting transition is dominated by the competition between the energy barrier and external force [100,101]. When the energy of the droplet in Cassie mode is greater than that in Wenzel mode, the interface state of the liquid on the superhydrophobic surface changes from being suspended on the gas film to directly contacting the surface, thus making the material lose its waterproof function. Therefore, the Cassie–Wenzel conversion should be avoided by adjusting the microstructure parameters. Meanwhile, Nosonovsky and Bhushan proved the irreversibility of the transition from the Cassie-Baxter to the Wenzel mechanism by experimental data [102,103]. This transformation could be induced by applying pressure [104], voltage [105], light [106], and vibration [107], but the transformation from Wenzel to Cassie-Baxter had not been observed. The research showed that only when the net surface energy of Wenzel was equivalent to the Cassie-Baxter model or when the predicted contact angle value by the Cassie-Baxter model was consistent with the contact angle value predicted by Wenzel, this conversion would happen.

Lafuma and Quere think that in some cases, even if the energy is suitable, this transformation will not happen, and it is metastable [108]. Extrandl thinks that this mechanism of conversion from Cassie-Baxter to Wenzel is closely related to the weight of the droplets and proposes a contact line density model [109]. When the weight of the droplet exceeds

the corresponding surface tension on the triple intersection line, this conversion will occur. Patankar believes that how these two states happen depends on how droplets are formed, that is, the historical process of system formation [110]. Quere also believes that the curvature of the droplet (curvature relies on the pressure difference between the inside and outside of the droplet) can adjust and change this transition [111]. Nosonovsky and Bhushan think that this transformation is an unstable dynamic process and study the possible unstable factors [112]. Some people also think that the curvature of multi-scale roughness can determine the stability of the Cassie-Baxter wetting mode [113–115]. However, up to now, there is no clear theoretical conclusion on how this conversion mechanism happened. According to the theory put forward by Nosonovsky and Bhushan, due to the influence of adhesion lag, wetting consumes less energy than non-wetting, so there is an asymmetric relationship between wetting and non-wetting. Adhesion hysteresis is one of the causes of contact angle hysteresis, and it is also the cause of state transition hysteresis of Wenzel and Cassie-Baxter. They also pointed out that the Wenzel state is more likely to occur from the point of view of appropriate energy for the surface with relatively low roughness (for example, a large, inclined space between protrusions). However, the Cassie-Baxter state is more possible to occur for the surface with relatively large roughness [116]. (See Table 2).

Table 2. Summary of terminology for wetting properties.

Abbreviations or Symbols	Terminology	Unit Symbols
CA	contact angle	degree
SA	sliding angle	α
CAH	contact angle hysteresis	$\Delta\theta$
θ_{ADV}	advancing contact angle	degree
θ_{REC}	receding contact angle	degree

2.2. Experiments of Hydrophobicity

In the last decade, research on superhydrophobicity materials has developed rapidly and is receiving increasing attention from scientists [117–120]. Adequate research shows that an effective way to change the wettability of the solid surfaces is by artificially adjusting and changing the chemical composition [121] and surface morphology of solid surfaces [122]. On the one hand, by introducing a compound containing the hydroxyl (-OH) functional group onto the solid surface, the hydrophilicity of the solid surface can be enhanced, facilitating its wetting by liquids. On the other hand, micro-nanostructured surface morphology can augment the solid's surface area and modify its surface energy, thereby influencing its interaction with liquids. Therefore, scholars often alter the hydrophobicity of materials by controlling the preparation conditions to obtain micro- and nanostructures of different sizes and shapes, such as spherical [123], lamellar [124], cubic, polyhedral, and flower-like structures [125]. Some examples, which are extracted from recent studies, provide a summary of constructed superhydrophobicity nanosurfaces (see Table 3).

Ultraviolet (UV) curing enables the rapid conversion of solvent-free liquid formulations into solid films by UV irradiation. Polyurethane acrylate (PUA) resin with unsaturated carbon–carbon double bond (C-C) can go through radical polymerization under the action of a photoinitiator. However, compared to rough fabric surfaces, the establishment of multilayer structures on flat metal substrate surfaces required more inorganic particles. Furthermore, when sufficient inorganic particles were used to confer superhydrophobicity, these particles may hinder the crosslinking of the resin monomer, thus failing to maintain the original adhesion and mechanical stability of the resin. Zhang et al. [126] enhanced the interfacial bonding strength with PUA by grafting C-C bonds to the surface of particles hybridized by carbon nanotubes (CNTs) and SiO_2 through 3-methylpropylpropyl trimethoxy siloxane (MPS). In addition, the C-C and Si-O bonds in the added MPS further increased

the cross-linking density. Moreover, the prepared PUA/MPS/CNTs@SiO$_2$ coating was still hydrophobic after friction and wear experiments.

A major disadvantage of artificial surfaces is that their superhydrophobicity is greatly reduced after they are inevitably worn or scratched by small particles. The wear properties of polymer coatings can be further enhanced by introducing hard nanoparticles such as carbon nanotubes, graphene oxide, and SiO$_2$. Shi et al. [127] studied the preparation of polyphenylene sulfide, polytetrafluoroethylene, and silicon dioxide (PPS-PTFE/SiO$_2$) composite coatings with different SiO$_2$ contents by simple spray method. The water contact angles (WCAs) of the prepared coating ranged from 152° to 145°, which could be attributed to its fibrous mesh structure and low surface energy. The introduction of SiO$_2$ nanoparticles in the composite coating effectively ameliorated the wear resistance of the coating. In addition, PPS-PTFE/SiO$_2$ coating had preferable corrosion resistance towards AZ31 magnesium alloy.
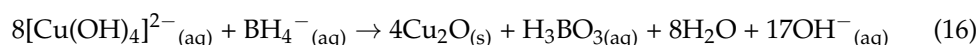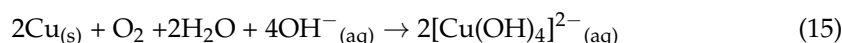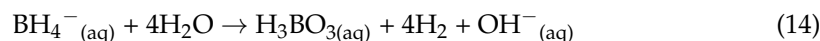
Besides the hydrophobic effect of preparing microstructure coating on the surface of the material, excellent hydrophobicity can also be achieved by the application of bionic microstructure on the surface of the material. The utilization of metal alloys in industrial machinery parts is widespread due to their exceptional mechanical properties and wear resistance. However, metal alloys are inclined to corrosion in humid environments and chlorine-containing solutions. As a result, its life and application areas are seriously limited. By optimizing the etching and electrodeposition time, Yu et al. [128] formed micron-plate structures, micron-sized papillary structures, and broccoli-like nanosphere nickel films on the brass surface. The modified structure had good water resistance, the static contact angle was $159.5 \pm 1.7°$, and the sliding angle was $3.3 \pm 0.6°$. After the surface energy was reduced by modification, the micro-nanocomposite structure could capture a large amount of air. Since air had perfect hydrophobicity, a large number of micro-nanocomposite structures bound to air were the main reason for the surface superhydrophobicity.

With the continuous advancement of science and technology, research on bionic interfaces has begun to expand from metallic element materials to non-metallic element materials. Single crystal silicon (sc-Si) possesses outstanding physical, chemical, mechanical, and semiconductor properties, which have shown approving outcomes in the design of lightweight applications such as electrical and electronic devices [129,130]. However, the poor hydrophobic characteristics of sc-Si render it unsuitable for complex environments. Researchers have been able to develop high-quality fleece structures on the surface of silicon substrates by dry etching [131,132], while photo-etching can readily create large-area mask patterns using photoresists [133]. Nevertheless, the aforementioned preparation methods do not meet the requirements of industrial applications because of their high cost and low efficiency. Chang et al. [134] developed a wet etching method to fabricate the hierarchical structures on the surfaces of sc-Si to improve hydrophobic properties, as shown in Table 3. The Fe(NO$_3$)$_3$/HF mixed solution was used to texture the surface of sc-Si through an oxidation–reduction reaction (Figure 3a). At the initial stage of the reaction, Fe^{3+} was reduced to Fe^{2+}, and Si was formally oxidized to SiO$_2$, which was then dissolved in a hydrofluoric acid (HF) solution to obtain micro-nanostructures with hemispherical etched pits and needle-like folds. The results indicated that the surface roughness of monocrystalline silicon substrate was the pivotal factor in determining its strength and hydrophobicity.

Analogously, Ahmad Kamal et al. [135] explored the effect of electrode distance (D$_E$) on hydrophobic behaviors of carbon nitride (CNx) thin films deposited on silicon substrate. With the decrease in D$_E$, the amount of nitrogen was increased, and the relative strength of the C=N→C=C and N-H→O-H bonds increased, which resulted in a change of the film property from hydrophilicity to superhydrophobicity. Furthermore, N atoms were added to the film structure to form fibrous nanostructures. Ahmad Kamal et al. [136] further explored the wetting behaviors of CNx nanostructures with various annealing temperatures (T$_A$) treatments. The exploration showed that as T$_A$ was increased to 700 °C, the CNx nanostructures provided a better contact angle of $158.1 \pm 1.5°$ if compared to

that of undisposed CNx nanostructures ($102.8 \pm 1.5°$). Moreover, the repeated drop coating tests showed that the films annealed at 700 °C provided excellent durability and retained superhydrophobicity properties after 10 drops of coating. This indicated that high annealing temperatures could eliminate defects in the nanostructure and further strengthen it, thus exhibiting excellent water resistance and self-cleaning performances, as well as high reusability of the nanostructure.
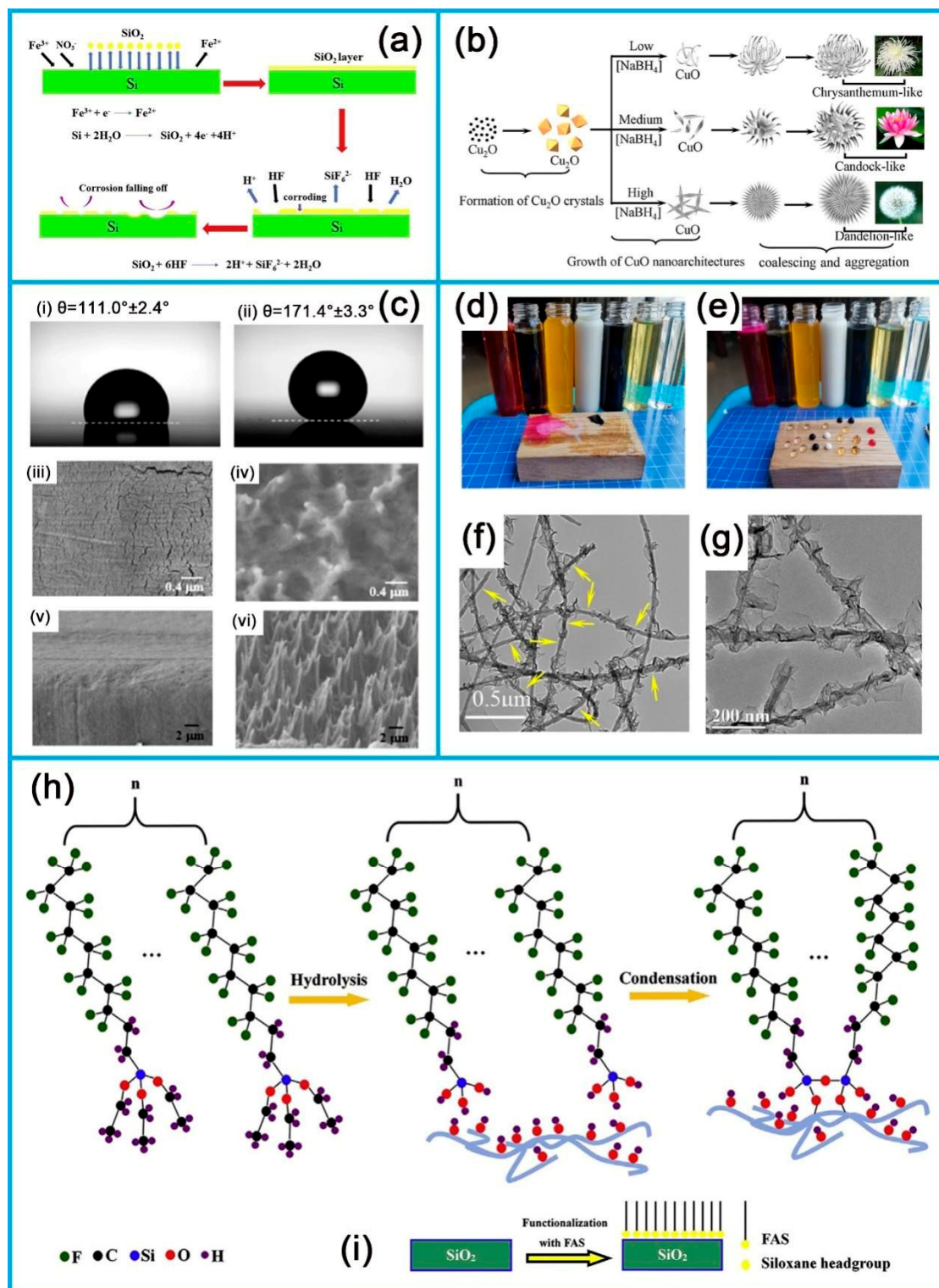
Recent studies have shown that nucleation and growth processes of inorganic films significantly affect their microstructure and shape. Fan et al. [137] prepared Cu_2O/CuO films with controllable flower shapes by direct crystallization assisted by sodium borohydride. Three types of Chrysanthemum-like, Candocl-like, and dandelion-like CuO microstructures were obtained by controlling the concentration of $NaBH_4$ (Figure 3b); the chemical reactions involved were thought to proceed as follows (Equations (14)–(17)):

$$BH_4^-{}_{(aq)} + 4H_2O \rightarrow H_3BO_{3(aq)} + 4H_2 + OH^-{}_{(aq)} \tag{14}$$

$$2Cu_{(s)} + O_2 + 2H_2O + 4OH^-{}_{(aq)} \rightarrow 2[Cu(OH)_4]^{2-}{}_{(aq)} \tag{15}$$

$$8[Cu(OH)_4]^{2-}{}_{(aq)} + BH_4^-{}_{(aq)} \rightarrow 4Cu_2O_{(s)} + H_3BO_{3(aq)} + 8H_2O + 17OH^-{}_{(aq)} \tag{16}$$

$$2Cu_2O_{(s)} + O_2 \rightarrow 4CuO_{(s)} \tag{17}$$

Herein, $NaBH_4$ was used as an alkaline catalyst and reductant to promote the growth of CuO nanostructures on Cu foil, as shown in Table 3. The hydrophobic experiment results showed that the surface wettability of CuO film changed from hydrophilic to hydrophobic by uncomplicated surface modification, which was attributed to sodium laurate being easy to self-assemble on the film surface and reducing the surface free energy.

In parallel, the self-assembled hierarchies have been an intensive and widespread subject of investigation in the field of hydrophobicity because of their fascinating physical and chemical properties [138–142]. As a result, three-dimensional (3D) hierarchical structures composed of nanostructured blocks (nanoplates, nanoparticles, nanoribbons, or nanorods) have been extensively explored [143–146]. The Bi_2S_3 flower-like layered nanostructures assembled by nanorods were successfully synthesized under hydrothermal conditions [147]. The contact angle of water at room temperature was measured by the Dataphysics OCA20 contact angle system. It could be clearly seen that the hydrophobic angle ($107.99°$) of flower-like layered nanostructures of Bi_2S_3 film was significantly higher than that of rod-like ($80.65°$) and sheet-like ($50.57°$) nanostructures. The results demonstrated that the prepared self-assembled films with nanostructure provided an effective strategy for improving hydrophobic properties.

In addition, the preparation process and processing parameters of the composites also affect the hydrophobic and hydrophilic transition of surfaces. The superhydrophilic surfaces with micro/nanostructures and passivated layers were developed on stainless steel surfaces by chemical etching and oxidation [148]. Subsequently, the superhydrophilic surfaces were easily changed to superhydrophobic surfaces via a self-assembled monolayer coating. The contact angle has been increased from ~0° for the raw stainless steel to $158.3°$ for the stainless steel with self-assembled monolayer coating. Furthermore, the reversible transition from superhydrophobicity to superhydrophilicity of ZnO thin films with diameters of 50–150 nm was controlled via alternating UV luminescence and dark storage [106]. The specific values for the wetting properties are presented in Table 3.
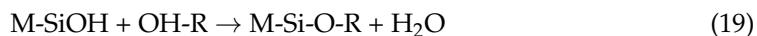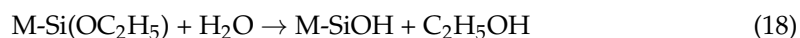
Figure 3. (**a**) Schematic diagram of preparation of stratification structure of sc-Si surface [134]; (**b**) growth mechanism diagram of three-dimensional hierarchical flower-like CuO architectures prepared with different concentrations of NaBH$_4$ [137]; (**c**) wetting behavior and surface characteristics of prepared superhydrophobicity PTFE sheets [149]; static behavior of water droplets on the surface of (**d**) the raw wood and (**e**) BMSW surface [150]; (**f**,**g**) TEM images of wicker-like SiC@graphene hierarchical structures [151]; (**h**,**i**) the schematic diagram of superhydrophobic treatment of SiO$_2$-coated SiC nanowires surfaces [152].

The successful synthesis of sic-based nanostructures with superhydrophobicity properties gradually attracted widespread attention from investigators in order to optimize hydrophobic properties in complex environments. The wicker-like SiC@graphene multidimensional nanostructures were prepared by the chemical vapor deposition method [151]. It could be seen that two representative graphene nanostructures, namely graphene nanoplane (yellow arrow in Figure 3f) and vast graphene nanoflakes (Figure 3g), were wrapped around the SiC nanowire core layer in turn. Polymers are extensively used as a combination of organic and inorganic components in the field of hydrophobic applications [153,154]. The nanostructured block copolymers (BCPs) based on methacryloisobutyl polyhedral oligomeric silsesquioxane (MAibPOSS) and trifluoroethyl methacrylate (TFEMA) were successfully synthesized via reversible addition–fragmentation chain transfer (RAFT) polymerization [155]. The core–shell and layered structures were obtained by dissolving BCPs in chloroform and tetrahydrofuran, respectively. After annealing, the contact angle of the BCPs coating on substrates increased from ~100° to ~128°, as recorded in Table 3.

Ryu et al. [149] produced the crown structures on a polytetrafluoroethylene (PTFE) sheet using a plasma treatment with argon and oxygen gases. The wetting behavior and surface features of the prepared superhydrophobicity PTFE sheet are shown in Figure 3c. The water contact angle (171.4° ± 3.3°) of the PTFE sheet treated by plasma was obviously higher than that of the bare PTFE sheet (111.0° ± 2.4°), as shown in Figure 3c(i,ii). The formation of nanometer sharp protrusions on the surface of the superhydrophobicity PTFE sheet was the key to excellent superhydrophobicity (Figure 3c(iii–vi)).

To date, the construction of the hydrophobic layer on the surface of the composite material is necessary to prevent the material from being adversely affected by its own large number of hydrophilic groups. Yang et al. [150] successfully prepared a hydrophobic micro/nanostructure similar to watercress leaves by coating Polyvinyl butyral/SiO_2 coating on the surface of the wood with the polydimethylsiloxane template secondary transfer replication technology. Additionally, the hydrophobic properties of virgin wood (Figure 3d) and biomimetic morphologies of superhydrophobic wood (BMSW) surfaces (Figure 3e) were examined using commonly used liquids. It could be clearly seen that the surface of the primitive wood shows no repulsion to these liquids. However, the droplets were standing on the prepared BMSW surface.

In addition to changing the surface nanostructure of the substrate, as described above, surface chemistry can also be changed to influence surface wettability [156]. Porous anodic aluminum oxide (PAA) has been extensively used in the systematic study of nanoscale material properties owing to its ability to precisely control pore size and pore spacing in the preparation process. Leese et al. [157] studied the wettability property of PAA coated with fluorosilane. It was also found that the contact angle of silylated PAAs (103 ± 2°) was significantly higher than that of pure PAAs (12 ± 2°). Moreover, the superhydrophobicity surface could be obtained by the chemical treatment of SiC nanowires coated with simple silica with fluoroalkylsilane (FAS) in ethanol solution at room temperature [152]. The hydrolysis equation of FAS in the preparation process (Figure 2h) was as follows:

$$M\text{-}Si(OC_2H_5) + H_2O \rightarrow M\text{-}SiOH + C_2H_5OH \tag{18}$$

$$M\text{-}SiOH + OH\text{-}R \rightarrow M\text{-}Si\text{-}O\text{-}R + H_2O \tag{19}$$

Herein, M is the hydrophobic group of the FAS, and R is the SiO_2-coated SiC nanowire surfaces. Based on the above-mentioned equations, a mass of silanol groups condenses with the hydroxyl groups on the SiO_2-coated SiC nanowire surfaces to form a stable chemical bond. After the condensation reaction, the binding of the FAS molecules to the SiO_2-coated SiC nanowire surfaces resulted in the exposure of the hydrophobic groups of the FAS molecules, effectively preventing water droplets from coming into contact with the surface (Figure 3i). It was noteworthy that the superhydrophobicity treatment of the surface did

not cause significant changes in the surface morphology, microstructure, and crystalline phase of the SiO$_2$-coated SiC nanowire.

Besides the single change of structure/chemical composition, modifications to both the structure and chemical composition of the composite surface have an important impact on the improvement of hydrophobic properties. Puukilainen et al. [18] added perfluoropolyether (PFPE) into melt polyolefin and used a nanoporous anodic aluminum oxide (AAO) mold insert to prepare a hydrophobic polyolefin (PO) surface with a nanopattern surface. The surface of PO showed ordered high aspect ratio nanostructures, and the contact angle increased by about 25% compared with untreated PFPE. Such remarkable improvement in the wettability performance could be attributed to chemical modification and nanostructure.

2.3. Hydrophobic Mechanism

In the previous two sections, the theoretical as well as experimental aspects of bionic structures in the field of hydrophobicity are described; however, the mechanisms of how specific functions are achieved under certain environmental conditions are not understood. This subsection provides a detailed description of the performance mechanism.
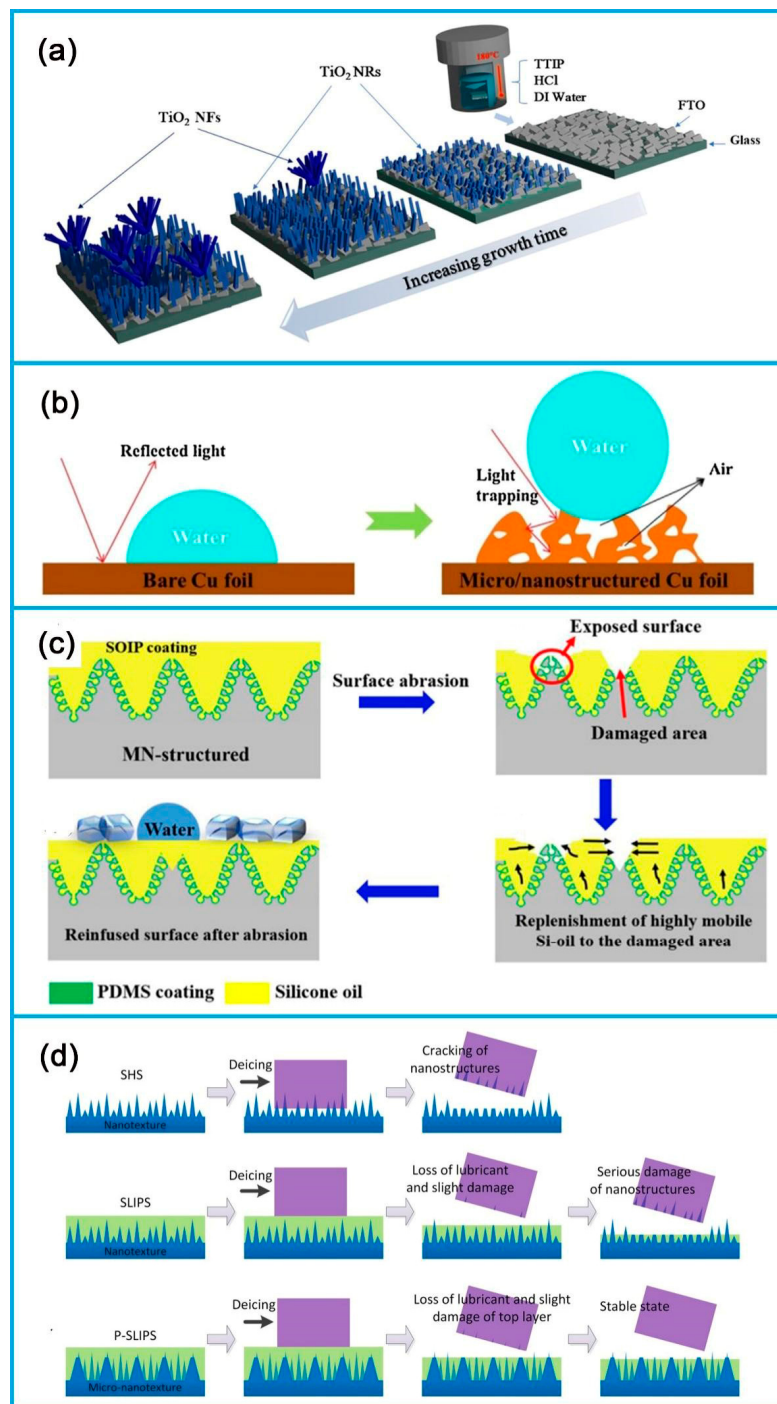
Based on Wenzel and Cassie's theory [93,98], lower surface energy and rough surfaces are the decisive factors in producing superhydrophobic surfaces. The superhydrophobicity MgAl-LDH modified melamine sponges (MA-LDH@MS) were prepared using an in situ growth method [158]. The hydrophobic experimental results indicated that the developed MA-LDH@MS was superhydrophobic; the detailed values of this CA are shown in Table 3. This was attributed to the fact that most of the hydrophile functional groups of MS are eliminated in the hydrothermal process, leading to a low surface energy, and MA-LDH was formed on the surface of MS, increasing the roughness of MS. Thus, the low surface energy and rough surface raise the water contact angle, leading to the superhydrophobicity surface of MA-LDH@MS.

Additionally, Zhao et al. [159] prepared a new superhydrophobic/super-oleophilic quartz sand surface for the selective separation of water and oil by constructing a siliceous rough structure and embellishing it with low-surface-energy hexadecyl-trimethoxysilane. The results showed that the contact angle of the liquid does determine the intrusion pressure. When the water was in contact with the modified quartz sand, the WCA was greater than 90°, the intrusion pressure was positive, and the water could not penetrate the quartz sand filter layer, while the opposite was true for oil. With the increase in the thickness of the quartz sand filter layer, the flux was decreased, and the separation efficiency was increased. Furthermore, the results of several tests manifested that the embellished quartz sand has good stability and reusability.

Porous polymer microspheres are widely used in applications because of their laminated morphology and vast surface area. Lv et al. [160] were the first group to construct a superhydrophobicity coating by using polystyrene (PS) microspheres as filler and beeswax as a hydrophobic agent. The relationship between the wettability of the coating and the porous morphology of the polystyrene microspheres was investigated. As the microspheres grew, the microsphere size increased, and the solid–liquid contact surface trapped a greater amount of air, resulting in an increase in CA and a decrease in CAH. Furthermore, as the size of the microspheres increased, the spacing between PS microspheres decreased with increasing PS microsphere volume to prevent water droplet intrusion. Thus, the opening of the porous surface and the reduction of the spacing between the PS microspheres are considered to be the two most important factors in improving the hydrophobicity of the coating.

Over the last few decades, hydrothermal reactions have made significant progress in the preparation of hydrophobic or superhydrophobicity coatings as an economical and environmentally friendly coating technology [161–163]. Mezzourh et al. grew high-purity rutile titanium dioxide nanorods (NRs) on fluorine-doped tin oxide (FTO)-coated glass substrates by a one-step hydrothermal method [164]. The effect of growth time on the structure and surface properties of the products was also investigated. Figure 4a shows

a schematic of the growth mechanism of TiO$_2$ nanorods on FTO substrates. When the reaction time was less than 1.5 h, the TiO$_2$ NRs were found to be arranged, but after 1.5 h, the nanoflowers (NFs) started to grow on the NR coating. Based on Wenzel's theory, these interesting roughness-graded TiO$_2$ NR structures would be beneficial for improving the wettability of the surface.

Figure 4. (**a**) Growth mechanism scheme of TiO$_2$ nanostructures on FTO substrate [164]. (**b**) Schematic diagram of antireflection and hydrophobicity enhancement of porous micro/nanostructured Cu foil [165]. (**c**) Schematic of MNS surface modified with SOIP coating [166]. (**d**) Diagram of damage process and lubricant losses on different surfaces during the icing/de-icing cycles [167].

Analogously, a simple hydrothermal method for preparing the layered porous micro/nanostructures on the surface of copper foils was proposed by Li et al. [165], as recorded in Table 3. A schematic diagram of the increased permeability and hydrophobicity of the porous micro/nanostructured copper foil is shown in Figure 4b. The enhancement of the antireflection and hydrophobicity of the copper foil can be attributed to the surface of the layered chemical porous micro/nanostructured surface. The contact pattern of micro/nanostructured copper surfaces can be described as a buffer layer formed by stagnant air, preventing the coating from being wetted. For micro/nanostructured surfaces, water droplets are mainly located on such air pockets and roll off easily when the surface is slightly tilted. In addition, such an air medium inhibits electron transfer between the electrolyte and the copper substrate, improving the corrosion resistance of the copper foil.

The surfaces of hydrophobic polyolefin (PO) were prepared by perfluoropolyether (PFPE) blends and nanostructures [18]. Chemical modification improved the hydrophobicity of polyethylene, and the contact angle between water and the surface was raised by about 10%. The nanostructure had a significant influence on the contact angle of the polyolefin with water. In particular, the masking process showed an ordered high spreading ratio nanostructure throughout the surface, which increased the contact angle by approximately 25%. This process has a guiding significance for preparing injection molded parts with good hydrophobicity.

Barthwal et al. [166] successfully prepared a lightweight, durable bionic superhydrophobicity slip anti-icing coating by infusing superhydrophobicity micro/nanostructured (MNS) aluminum with a non-toxic, inexpensive lubricating silicone oil. The MNS surfaces exhibited remarkable durability, exhibiting low ice adhesion (108 kPa) after 20 ice/de-icing cycles and wear experiments and long-term anti-icing after 4 months of exposure to the environment (55 ± 13 kPa). Based on these results, a schematic diagram of the silicone oil-infused polydimethylsiloxane (SOIP)-coated modified MNS surface was presented (Figure 4c). The existence of a bionanostructured micro/nanostructure on the MNS surface is like a mechanically stable reservoir, which captures excess silicone oil in the micro/nanocavity. The silicone oil lost from the surface during the icing/de-icing cycle is compensated for by the surface capillary action of excess silicone oil trapped in the micro/nanostructure cavity, resulting in excellent durability.

Similarly, Tan et al. [167] injected lubricants into microconical pores and porous nanostructures. The porous nanostructures maintain lubricant to form a smooth lubricating film, and the microcone pores protect the nanostructures, thereby increasing the Journal Pre-proof-23 durability of the lubricant injected surface. Damage processes and lubricant loss in different surfaces during the icing/de-icing cycles on different surfaces are illustrated in Figure 4d. During de-icing, the mechanical interlocking of ice and superhydrophobic surfaces (SHS) causes the nanostructures to crack. As the slider consumes lubricant during the icing/de-icing process, the nanostructure will be gradually exposed and broken, resulting in a rapid increase in the adhesion strength of the ice. The nanostructures on the p-slip are protected by the microcone pores and only minor damage occurs at the top layer at first. At this point, the adhesion strength of the ice tends to stabilize. The results show that the adhesion strength remains low and stable during the ice/de-icing process, and the durability of the p-slip is greatly improved.

As most metals are known to be hydrophilic, Yang et al. [168] pioneered the use of femtosecond laser raster scanning to obtain anisotropic superhydrophobic aluminum surfaces in the shape of rice leaves, as recorded in Table 3. The contact angle measurements, structural analysis, and spectroscopic detection were used to fully characterise the bionic surfaces and to understand the causes of anisotropic superhydrophobic surfaces. For hydrophobic-graded micro/nanostructured surfaces, the following Equations (20)–(24) could be used:

$$\cos\theta = \varnothing_s (r_s \cos\theta_0 + 1) - 1 \qquad (20)$$

$$r_s = \frac{S_{actual}}{S_{projected}} \qquad (21)$$
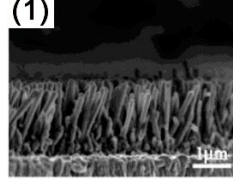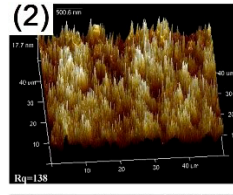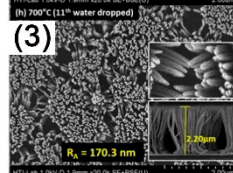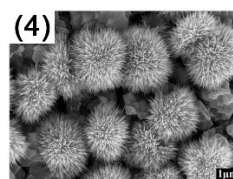
$$\varnothing_s = \frac{a}{a+b} \tag{22}$$

$$\sin\alpha = \frac{2kr_s\varnothing_s\sin\theta}{g}\left[\frac{3\pi^2}{m^2 p(2-3\cos\theta+\cos^3\theta)}\right]^{1/3} \tag{23}$$
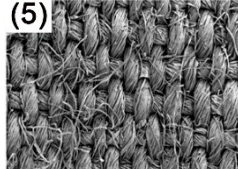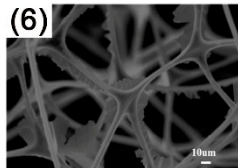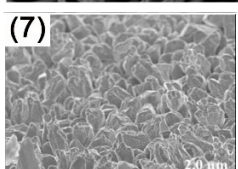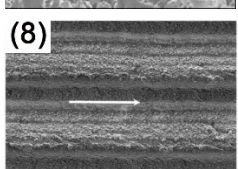
$$k = \left\{\frac{9m_0{}^2(2-33\cos\theta_0+\cos^3\theta_0)}{\pi^2}\right\}^{1/3}\frac{\sin\alpha_0\left(gp^{1/3}\right)}{6\sin\theta_0} \tag{24}$$

where θ is the contact angle, θ_0 is the plane contact angle, $\varnothing_s$ is the fraction of the projected area of the solid surface wetted by the liquid droplet. r_s is the roughness factor of surface structures. S_{actual}, as the actual surface area, can be directly measured with a 3D digital microscope; $S_{projected}$, as projected area, can be calculated according to the measurement chart. a is the width of the ridge (the distance between adjacent grooves), and b is the width of the groove. m_0 is the weight of the corresponding droplet. The sliding angle can be easily calculated by substituting the values. The slight difference between theoretical and experimental values is due to the oxidation of the metal.

Table 3. Summary of various materials and preparation strategies adopted to synthesize superhydrophobic surfaces.

Matrix	Low-Surface-Energy Material	Fabrication Technique	Major Properties	Summary	Morphology	Ref
Glass wafer	-	Sol-gel	Controllable wettability	CA = 161.2 ± 1.3°		[106]
sc-Si	Fe(NO$_3$)$_3$	Wet etching	Hydrophobicity	CA = 144.5°		[134]
Si (100) substrate	-	RF-PECVD	Waterproofness, self-cleaning property and reusability	CA = 158°		[136]
Cu foil	Sodium laurate	Direct crystallization	Hydrophobicity	CA = 156 ± 2°		[137]

Table 3. *Cont.*

Matrix	Low-Surface-Energy Material	Fabrication Technique	Major Properties	Summary	Morphology	Ref
BCPs	-	RAFT	Hydrophobicity	CA = 128°		[155]
MgAl-LDH	Melamine sponge	In situ growing	Superhydrophobicity	CA = 163.2°		[158]
Cu foil	-	Facile hydrothermal	Antireflection and hydrophobicity	CA = 142.6°		[165]
The structured aluminum	-	Femtosecond laser raster Scanning	Superhydrophobicity	CA = 153 ± 0.8°		[168]

2.4. Hydrophobic Applications

Numerous natural plants and animals have advanced special wetted surfaces to adapt to their habitats [169–171]. Inspired by nature, extensive bionic functional surfaces have been artificially manufactured and used for corrosion resistance, freeze-proofing, and oil–water separation [172,173]. In particular, superhydrophobic surfaces with anisotropic sliding properties are becoming increasingly popular in the fields of microfluidics, tissue engineering, and fluid repulsion. For example, in the field of daily household appliances, superhydrophobic surfaces can be applied to kitchen utensils and toilet facilities to make them have self-cleaning ability, thus reducing the frequency and workload of cleaning work. The anti-fog functional surface can be used for mirrors and automobile glass, which improves visibility and enhances safety. In the industrial field, the application of a superhydrophobic surface on the surface of ships and aircraft can reduce the frictional resistance of water, improve transportation efficiency, and reduce energy consumption. Superhydrophobic surfaces have garnered widespread notice from researchers due to their wide range of applications. Scholars have been able to directly influence the function of superhydrophobic surfaces by unveiling the dynamic behavior of water droplets on them to understand the key to their hydrophobic mechanism.

To date, there is still a great demand for a reliable and uninterrupted supply of electricity in countries around the world. Outdoor high-voltage insulators for power generation, transmission, and distribution systems offer an effective strategy for addressing this goal [174,175]. However, the tendency for airborne contaminants to accumulate on the surface of ordinary insulators is conducive to high surface energy generated by the strong electrostatic bonding between the various atoms in the material [176–178]. Particularly during light rain, fog, or mist, these contaminants can become wet and, thus, form a conductive layer through which leakage currents flow, causing the insulator surface to flash through the electrical system [179]. This can easily lead to contaminated flask accidents, resulting in

huge social and economic losses. Superhydrophobicity insulators, with their anti-fouling, self-cleaning, and delayed ice-covering properties, decrease the risk of insulator flashover accidents and ensure the safe transport of power systems [180–183].

The research demonstrated that durability is a fundamental requirement for achieving superhydrophobicity in silicone rubber used in outdoor insulation applications [184–186]. Boinovich et al. [187] have shown that the evolution of the contact angle of a superhydrophobicity surface in continuous connection with water over a certain period of time reveals the mechanism that causes the change in the contact angle of a superhydrophobicity material in continuous contact with water. This suggests that the variation in the contact angle of a hydrophobic material after a considerable period of contact with water has distinct influences on the application of superhydrophobicity materials.
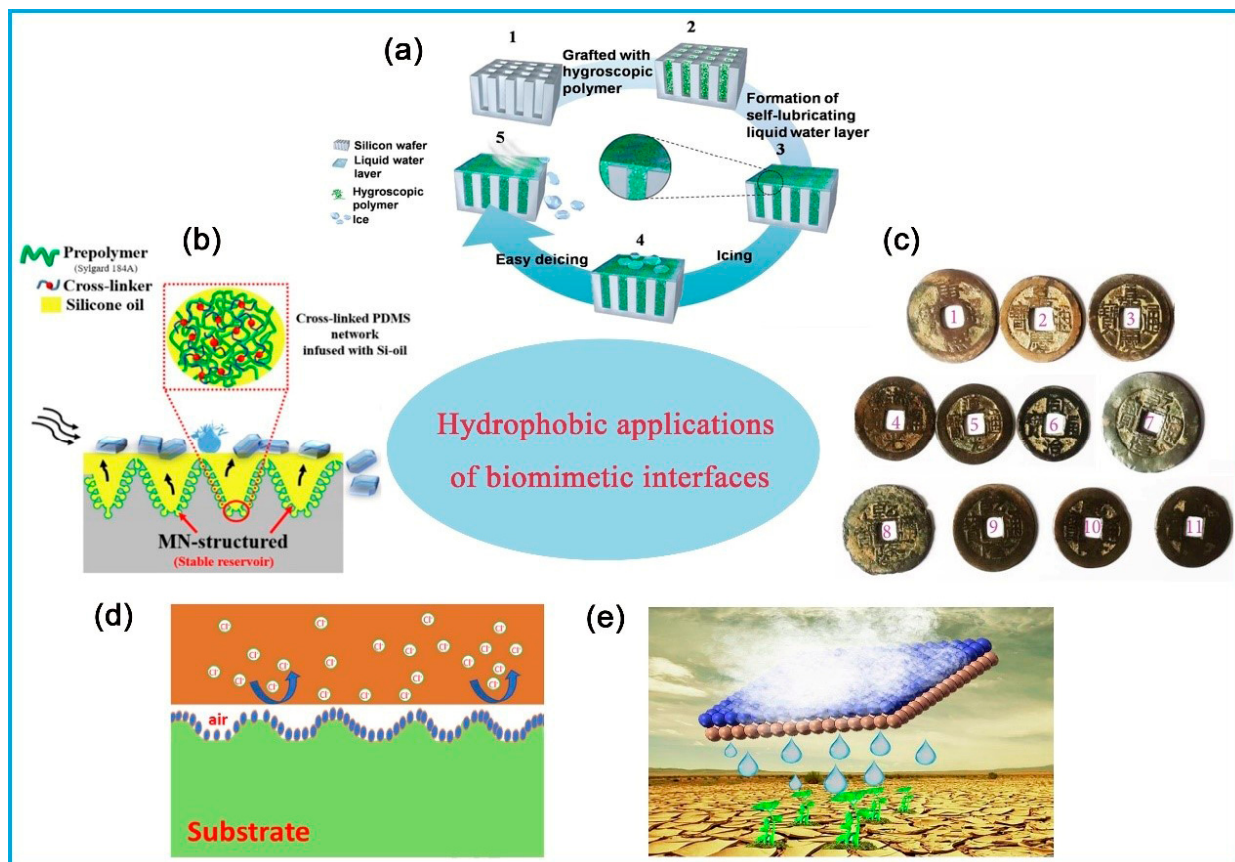
Similarly, the phenomenon of icing and ice accumulation on solid surfaces has serious implications for the operation and maintenance difficulties of aerospace [188,189], ground transportation [190], industrial machinery [191], and household appliances [192] during the cold environment. Over the past decades, techniques such as thermal [193], chemical [194], and mechanical methods [195] have been exploited to decrease or remove the formation of surface ice. At the same time, the high-cost, high-energy consumption and the introduction of environmentally polluting chemicals [191,196] have prevented widespread use. Inspired by the specific wettability of organisms in nature, the preparation of micro/nanosuperhydrophobic surfaces allows ice formation on hydrophobic surfaces to be readily removed by their own weight or by natural wind. Yang et al. [190] used ultrasonic chemical etching combined with boiling to prepare hydrangea-like micro- and nanostructured superhydrophobic surfaces on aluminum substrates. The results show that the freezing and frosting time of the surface is delayed at low temperatures owing to the presence of abundant micro- and nano-air pockets, and the actual solid–liquid contact area is reduced.

Chen et al. [188] successfully produced the anti-icing superhydrophobicity coating through jointing cross-linked hygroscopic polymers on the micro-pores of silicon wafer surfaces (Figure 5a). A microporous array was prepared on the substrate, as shown in Figure 5a, and a cross-linked hygroscopic polymer was synthesized via grafting free radical polymerization within the microporous pores. When the temperature drops, the network of hygroscopic polymers within the micropores swells deliquescently owing to water absorption or condensation. If the temperature is low enough to absorb enough water, the water-swollen polymer network within the micropores will bulge out of the micropores. Due to mutual attraction between the molecules, the swollen polymers fuse together to form a self-lubricating liquid water layer. Ice on the substrate surface could be blown away in the presence of strong winds. The anti-icing surfaces prepared are a guide to the design of anti-icing coatings with optimum performance.

Apart from the anti-icing properties of superhydrophobicity surface, surface durability is also a significant consideration [200]. Barthwal et al. [166] prepared the lightweight and durable biomimetic anti-slip and anti-icing coating by injecting non-toxic, sixpenny lubricating silicone oil onto the surface of a superhydrophobicity dual-scale micro- and nanostructured (MNS) aluminum. As shown in Figure 5b, the coating clearly retained the silicone oil in the structure, and the MNS surface coated with polydimethylsiloxane was a mechanically stable reservoir layer that stored the silicone oil in the micro-nano cavity. Therefore, this also compensated for existent silicone oils, which were lost from the surface owing to surface tension during the icing/de-icing process.

In addition, many reports have demonstrated the effective corrosion protection of superhydrophobic surfaces [201]. As an important engineering material, the corrosion protection of metals is one of the main concerns [202,203]. Prolonged exposure to contaminants and harsh operational environments (e.g., moisture) may result in the corrosion of metals, leading to a significant reduction in material service lifespan and even safety hazards [204–207]. Among these, copper coins [197], which were the currency in circulation in ancient times, received a tremendous amount of attention from the investigators

owing to their severely corroded surfaces, as shown in Figure 5c. The preparation of corrosion-resistant hydrophobic surfaces on alloy surfaces became a difficult challenge. Liang et al. [208] fabricated superhydrophobic surfaces on Al substrates using a solgel method, which was shown to be effective in improving corrosion protection owing to the synergistic effect between superhydrophobicity and silica-based films. Zheng et al. [209] reported that the surface of the micro-nanostructure possessed better mechanical stability and chemical durability against sand erosion. The corrosion current density of the superhydrophobic surface was reduced by three orders of magnitude, and the corrosion potential was in possession of a significant positive displacement of 0.93 V.

Figure 5. (**a**) Schematic diagram of preparation of superhydrophobicity surface [188]. (**b**) The schematic diagram of the MNS process of compensating for icing/de-icing by surface tension [166]. (**c**) Schematic diagram of representative copper coins in Qing Dynasty [197]. (**d**) Schematic diagram of the hierarchical micro/nanostructures capturing air layers [198]. (**e**) The model of fog replenishment [199].

The hydrophobic surfaces have been used in extensive applications. However, the preparation of hydrophobic surfaces with a wide range of excellent performances remains a difficult challenge. The hierarchical micro- and nanostructured superhydrophobic surfaces have been successfully prepared by a combination of sandblasting and chemical etching (Figure 5d) [198]. The wetting, droplet impact kinetics, freezing delay time, resistance to frost formation, superhydrophobicity stability, and corrosion resistance have been systematically compared and analyzed. The graded superhydrophobic surfaces have longer freezing delay times, better resistance to frosting, and significant corrosion resistance owing to the large number of air pockets captured by the micro- and nanostructures compared to the unstructured surface. These studies are beneficial for broadening the actual applications of superhydrophobic surfaces in certain harsh environments.

It is reported that a population exceeding one billion individuals will encounter severe water shortage in ten years, especially in arid areas [210–212]. In arid areas (the coastal

areas and desert areas) where the water content of fog is higher than that of rain, collecting rain by fog is a potential method to obtain fresh water. More scientists have prepared bionic fog-trapping materials and devices inspired by the Namib desert beetle [34], spider silk [213], and cactus [214], which are expected to resolve the problem of water scarcity in remote areas [215–217]. Currently, fog trapping can be categorized into three parts: water trapping, water supply, and water removal. Therefore, the surface morphology and wettability of bionanomaterials exert a significant impact on the fog collection [218–220]. Zhou et al. [199] prepared a micro- and nanostructured hydrophobic hybrid surface by a simple hydrothermal method. Figure 5e shows a simple model of fog replenishment. The optimal parameters for fog collection were selected by varying the size and tilt angle of the prepared copper foam. The hydrophobic surface has an efficient fog-trapping effect (~209% improvement) compared to the pristine surface.

Bionics is the investigation and simulation of functional properties required for biological systems. It concerns translating basic principles found in nature into human-made technologies. The lotus effect means that the lotus leaves exhibit extremely high water resistance and self-cleaning properties. Lotus leaves have small protrusions on the surface, covered with waxy hydrophobic crystals. These characteristics make plant leaves superhydrophobic. This effect comes from the non-uniform/compound wetting of the water, where the water droplets are located at the top of the protrusions and air is trapped between them, thus significantly decreasing the solid contact area with the water droplets. Hydrophobicity can be modified by different structures. Surface structure is essential for the transition from hydrophilic to hydrophobic state. The dual-scale hierarchy with branched nanostructures is an important factor in achieving superhydrophobicity. The superposition of hemispherical papillary nanostructures and dendritic nanostructures exerts a significant positive impact on decreasing frictional resistance. Lu et al. [221] conceived a new method for the preparation of two superhydrophobic surfaces with micro/nanobilayer hierarchical structures on copper substrates to research the impact of the contact angles of the corresponding layered micro/nanostructures and the coexistence of three phases on the lubrication process. The experimental results indicated that the layered surface made the matrix highly hydrophobic and can significantly decrease the friction resistance of the copper matrix. As the air was trapped by the concave and convex surfaces of the surface and moved vertically, the formation of a thin gas film between the fluid and the superhydrophobic wall was conducted, thereby enhancing lubrication performance. The hierarchical microstructure surface improved the total drag reduction effect of trapped air under liquid flow. The higher the quality of the hydrophobic surface, the more enhanced the lubrication property.

Surface graphization can effectively improve the hydrophobicity of epoxy coatings while decreasing surface attachment and friction without compromising the structural integrity and stiffness of epoxy coatings. Surface graphization can effectively improve the hydrophobicity of epoxy coatings while decreasing surface attachment and friction without compromising the structural integrity and stiffness of epoxy coatings. Through the Cassie-Baxter wetting mechanism, the addition of micropatterns on the coating surface can foster the transition of the hydrophilic epoxy surface to the superhydrophobic state. Under different normal forces, the micropattern reduces the contact area and, thus, is able to effectively influence the tribological properties of the surface. The incorporation of tiny patterns into the epoxy material mitigates the sticking of nails while reducing the overall shear force. The improvement of the hydrophobicity is achieved while simultaneously decreasing surface attachment and friction without compromising structural integrity.

The particular superhydrophobicity and the anisotropic friction characteristics for biologically inspired superhydrophobic surfaces facilitate directional superhydrophobicity and dynamic control of water transport. These properties are mainly due to the unique hierarchical morphological characteristics of biological scales. Zhao et al. [222] used a three-oblique beam laser ablation treatment to prepare a three-dimensional inclined bionic snake scale surface that could effectively realize anisotropic friction. The synergistic effect of the

nanomicrostructure and the intrinsic change of surface chemistry after laser irradiation showed unique superhydrophobicity along a specific direction. When the water droplet is wet and rolled on the surface, the contact area between the solid and liquid increases in the forward direction and decreases when moving in the opposite direction. The negative friction of the prepared surface was greater than the positive friction, and the air pockets at the interface were broken by water flow, leading to an increase in the surface adhesion.

Various chemically modified surfaces, such as boundary lubricant films/coatings, are employed to reduce intrinsic adhesion and friction by increasing the hydrophobicity and lubricity of the material. However, the method of chemical modification has some limitations. Bionic surface morphology modification can effectively reduce friction at the micro/nanoscale. Bionic patterned surfaces reduce intrinsic adhesion and friction by being hydrophobic and decreasing the physical contact area between the surfaces. Superhydrophobic surfaces are attributed to the synergistic effects of chemical and physical surface properties. The adhesive force between the liquid and the solid at the solid/liquid interface will facilitate diffusion, while the cohesive force of the liquid will bead it. The incorporation of micro- and/or nanopatterns onto the surface enhances the factual surface area but may decrease the nominal contact area with droplets located at the top of air pockets in rough surfaces. When the biomimetic surface is applied to nanoscale boundary lubricants, it shows a more significant ability to reduce surface forces, as well as improve wear resistance.

2.5. Bionic Interface Technology
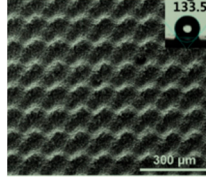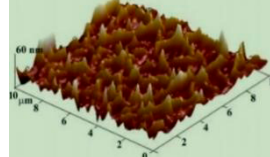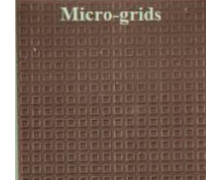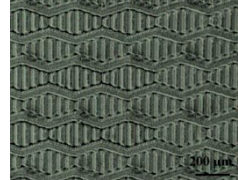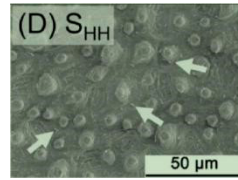
There are tens of thousands of micro/nanostructural patterns in natural species whose characteristics hide almost unlimited potential of technical ideas [223]. The research, development, and application of micro/nanostructural patterns open up new opportunities for innovative development of materials science and engineering applications [224]. Because of the application of inspiration from natural patterned surfaces in engineering, the diversity of bionic surface functions also shows many interesting phenomena, including friction and wear [225], lubrication, self-cleaning [226], hydrophobic [168,227], and antibacterial [228] phenomena. The functionality of bionic interface has attracted great interest from researchers and continuous experimental research and application of laser, nanoimprint [229] and 3D/4D printing technologies [230].

Natural rose petals are super hydrophobic and have high adhesion. Inspired by rose petals, Song et al. [227] used laser processing technology to construct periodic microcolumn structures on the surface of 304 stainless steel (SS) substrates in Table 4. Combined with the graphene film (G film) in chemical vapor deposition technology, the dense G film was transferred to the etched stainless steel (ESS), and the wettability of the SS surface was controlled. The integration of G film and rose petal structure achieved high adhesion and dehumidification of the composite surface, and the WCA of G/ESS reached 154.3°. In addition, the structural membrane can retain superhydrophobic characteristics under both acidic and alkaline conditions and has high adhesion to water. It is still a challenge to effectively gain an ideal superhydrophobic metal surface by conventional laser ablation techniques. Superhydrophobic metal surfaces represented by aluminum can be fabricated simply and efficiently by combining traditional laser ablation technology with surface engineering technology. Inspired by the lotus leaf, Zhao et al. [226] used nanosecond laser ablation technology to fabricate a lotus leaf-like three-stage composite microstructure with micro-protrusions, micro-agglomerates, and nanoparticles on the aluminum surface. The specific parameters are presented in Table 4. The change of wetness of laser-ablated aluminum surface from superhydrophilic to superhydrophobic was attributed to the formation of hydrophobic C-C/C-H species by organic adsorption. After heat treatment, the relative content of C-C/C-H species increases quickly, and the corresponding relative content of -OH species decreases quickly, resulting in a rapid hydrophobicity of the laser-ablated aluminum surface and excellent anti-wetting and self-cleaning performances. In addition, nanoparticles and large periodic spacing perform a crucial role in enhancing superhydrophobicity.

In addition to realizing the hydrophobicity of the material surface, the surface microstructure also performs a significant role in anti-fouling and shows obvious anti-wear [231,232]. He et al. [225] integrated 3D printing technology with subsurface-initiated open-loop metadecomposition polymerization (ROMP) to constitute the multi-scale brush-based anti-fouling surface shown in Table 4. A biomimetic shark structure substrate embedded with a ROMP initiator was fabricated using commercial acrylic resin 3D printing. The embedded poly (ionic liquid) brush was then grafted to a fabricated bionic shark by subsurface-initiated ROMP of a new ionic liquid monomer ([BNIm][Br]), including benzotriazole and imidazole groups. The results showed that a fabricated poly (ionic liquid) brush biomimetic surface also exhibits a fairly good anti-fouling property against microalgae (porphyrins and Durosia) owing to the synergistic effect between surface composition and microstructure. In addition, the polyionic liquid can be grafted to the surface and subsurface of the resin matrix and showed significant wear resistance. Dome-like structure is a kind of biological surface microstructure in nature, and its special structure provides inspiration for the design of impact-resistant structural materials. The majority of current biomimetic dome-like surface microstructural impact-resistant materials are directly molded by 3D printing technology. However, the samples obtained by this technique cannot be dynamically adjusted for impact resistance in various applications. The existing research shows that the 4D printing technology of metamaterials possesses extensive potential for application in the engineering field. Nevertheless, the majority of research on 4D printing technology is limited to shape memory materials. The dynamic bionic mechanical metamaterial of the dome structure array was prepared by 4D printing technology, as shown in Table 4, and different responses and deformations were produced by programming the designed structure mode and different thermal stimulation modes [233]. With the increase in the number of circular elements, the structure exhibits enhanced pressure-bearing capacity and energy absorption performance. In addition, the combined structure of circular elements with different diameters can fit complex surfaces effectively and may be fit for special applications.

With an increasing awareness of physical health, the emergence of bioceramic and bionic scaffolds provides more options for the application of traditional polymers and metals in medicine [234]. Despite the superior mechanical and physical properties of bioceramics, their antibacterial and tribological properties are very limited in practical applications. The microgrid texture on the surface of bioceramics can make it have hydrophobicity and improve the wear resistance effectively. In addition, surface texture has particular advantages in improving the antibacterial behavior of the materials. To enhance the property of the 3 mol% yttria-stabilized tetragonal zirconia polycrystal, Xu et al. [235] used laser ablation to fabricate three surface textures: microgrid, microfeather, and microgroove. The experimental results showed that the micro-grid texture had good wear resistance properties. Compared to the groove texture, the micro-feather texture exhibited a superior friction reduction effect. Bacterial adhesion and propagation were disrupted owing to alterations in surface wettability and the presence of roughness. Therefore, surface texture played a significant role in decreasing the amount of friction and wear at the contact interface. The greater the density of the surface texture, the lower the contact area with the friction parts.

Table 4. Preparation method and summary of bionic interface technology.

Bionic Object	Matrix	Preparative Technique	Result	Structure	Comparison
Rose petal-like microscale structure [227]	304 stainless-steel	Laser etching and chemical vapor deposition	WCA ~ 133.5°		Simple process, low cost, and fast etching rate
Mussel-inspired [224]	Polypropylene plate	Adhesion technology and thiol chemistry	SWCA ~ 39°		Simple and versatile
Butterfly wings, peacock tail feathers, and dolphin skins [235]	3 mol% yttria-stabilized tetragonal zirconia polycrystal	Laser ablation method	WCA >150° COF ~ 0.179		High machining efficiency and noncontact
Sharklet [225,231]	Commercial photosensitive acrylic resin	3D printing	WCA ~ 61° COF ~ 0.17		High efficiency, high manufacturing flexibility, well machining repeatability, high accuracy, and strongenvironmental adaptability
	Al_2O_3/TiC ceramic	Laser surface texturing	WCA ~ 76.3° COF ~ 0.07		
Lotus leaf [229]	UV-curable waterborne polyurethane acrylate	UV nanoimprint lithography	After wear WCA >150°		Efficient, environmentally friendly, energy-saving, enabling, and economical

3. Biomimetic Interfaces in the Tribology

Similar to hydrophobic surfaces, the microstructure of friction interface is in possession of a considerable influence on their friction and wear behavior. As the increasing demand for working efficiency, service life, and application accuracy of mechanical systems, controlling friction and wear has aroused great interest for researchers [236–238]. To date, a variety of well-designed or additive-induced microstructures have been extensively investigated to realize the desired friction reduction and anti-wear optimization for moving parts [239,240]. In this section, massive efforts on developing the ideal frictional microstructure to achieve excellent tribological performances are summarized, some of which are highlighted in Table 5.

3.1. Dry Friction

An irregular surface texture was initially proposed to optimize tribological performances in the 1960s [241]. Subsequently, surface texturing was applied in the tribology field to achieve wistful friction-reducing and wear-resisting performances. With regard to biomimetic microstructure design systems, the synergistic effects of surface texture and nanoadditive have increasingly aroused extensive concerns [242–245]. Maldonado-Cortés et al. [246] studied the role of laser surface texturing channels and nano-TiO$_2$ particles on the tribological performances of tool steel. Superior tribological performances were observed in the sample with horizontal microchannels compared with those with vertical textured channels, corresponding to a wear reduction of up to 89.8%. Nanolubricants containing TiO$_2$ further amplified this improvement (57.8%), which rendered the composites to exhibit attractive friction and wear behaviors. Therefore, the synergistic effect of the biomimetic microstructure and lubricant is significant for worn surfaces.

Inspired by the rapid development of nanotechnology, the application of surface micro/nano-texturing in the field of tribology enables the structure and function of materials to be controlled at the nanoscale [247]. For miniaturized systems, owing to the larger surface area to volume ratio of devices, problems raised by adhesive force and friction force are still open to researchers. Steck et al. [248] fabricated deformation-resistant nanotextured surfaces. Figure 6a provided the schematic of the preparation of IP-DIP/Al$_2$O$_3$ core–shell nanostructures (CSNs), in which IP-DIP was a specially customized negative photoresist. As shown in Figure 6a(i,ii), IP-DIP nanodot arrays were fabricated on glass substrate silica, and nano-Al$_2$O$_3$ was uniformly coated on these nanodots (Figure 6a(iii)). After the scratch tests, the friction coefficient was increased by 80% via printing IP-DIP nano-dots on a silicon substrate, but for IP-DIP/Al$_2$O$_3$ CSNs systems, the friction coefficient was lowered substantially to 35% below that of the bare silica substrate. Furthermore, minimal nanostructure deformation was detected in such a texture when the contact pressure was greater than 20 GPa. The presence of nano-Al$_2$O$_3$ endowed the nanodot array with significantly reduced surface adhesion and improved carrying capacity, leading to the splendid tribological behaviors of the textured surface.

Compared with zero-dimensional (0D) nanoadditives, one-dimensional (1D) additives are in possession of a greater aspect ratio; this characteristic performs a vital role in the structural evolution of composites [249–251]. The dispersion and structural characteristics of nanoadditives have been increasingly regarded as the key parameters for controlling the friction and wear of composites [252–254]. The well-dispersed 1D additives perform a vital role in the grain structure of metal-based composites [255]. The effect of MWCNT on the microstructural evolution of aluminum-based surface composites was experimentally investigated [256]. The presence of multiwall carbon nanotubes (MWCNT) led to significant grain refinement due to their grain boundary pinning action, resulting in the impediment for grain growth during the dynamic recrystallization process. The fine and compact grain structure endowed the composite the significant improvements in hardness, impact toughness, and corresponding anti-wear performance. Huang et al. [257] further reported the sliding wear behaviors of AZ61 magnesium alloy reinforced with CNTs. The detailed value of such friction coefficient is shown in Table 5. The grain size was noticed to reduce as the content of CNTs increased up to 1 wt.%. The CNTs were pinned up at grain boundaries and retarded the grain growth, which led to grain refinement of composites, thus increasing the strength. The mass wear rate of the 1 wt.%-CNT/AZ61 composite was reduced 7% when compared with the unreinforced alloy. In addition to metal-based composites, 1D additives can also significantly enhance the structure of polymer-based composites, thus significantly reducing the adhesive wear and plow wear of the composites [258–260]. In the study of Wu et al. [259], the friction and wear properties of carbon fiber (CF)-reinforced PTFE composite coating were investigated via ball-on-disk friction and wear tester. The results showed that after testing of applied load of 10 N, when the mass fraction of CF was 20%, the friction coefficient remained relatively stable at about 0.17, and the wear rate significantly decreased to 2.74×10^{-4} mm^3/Nm. The specific values,

such as wear rate and the friction coefficient, are recorded in Table 5. Excellent tribological properties may be attributed to the formation of a continuous and uniform transfer film, thus preventing the large-area damage of the composite coating. Additionally, after surface modification in the treatment of HNO_3 followed by coupling agent, the dispersibility of carbon nanofiber (CNF) in PTFE composites could be further improved, and the wear resistance of CNF/PTFE composites was enhanced [260]. The related values of the excellent wear resistance have been recorded in Table 5.
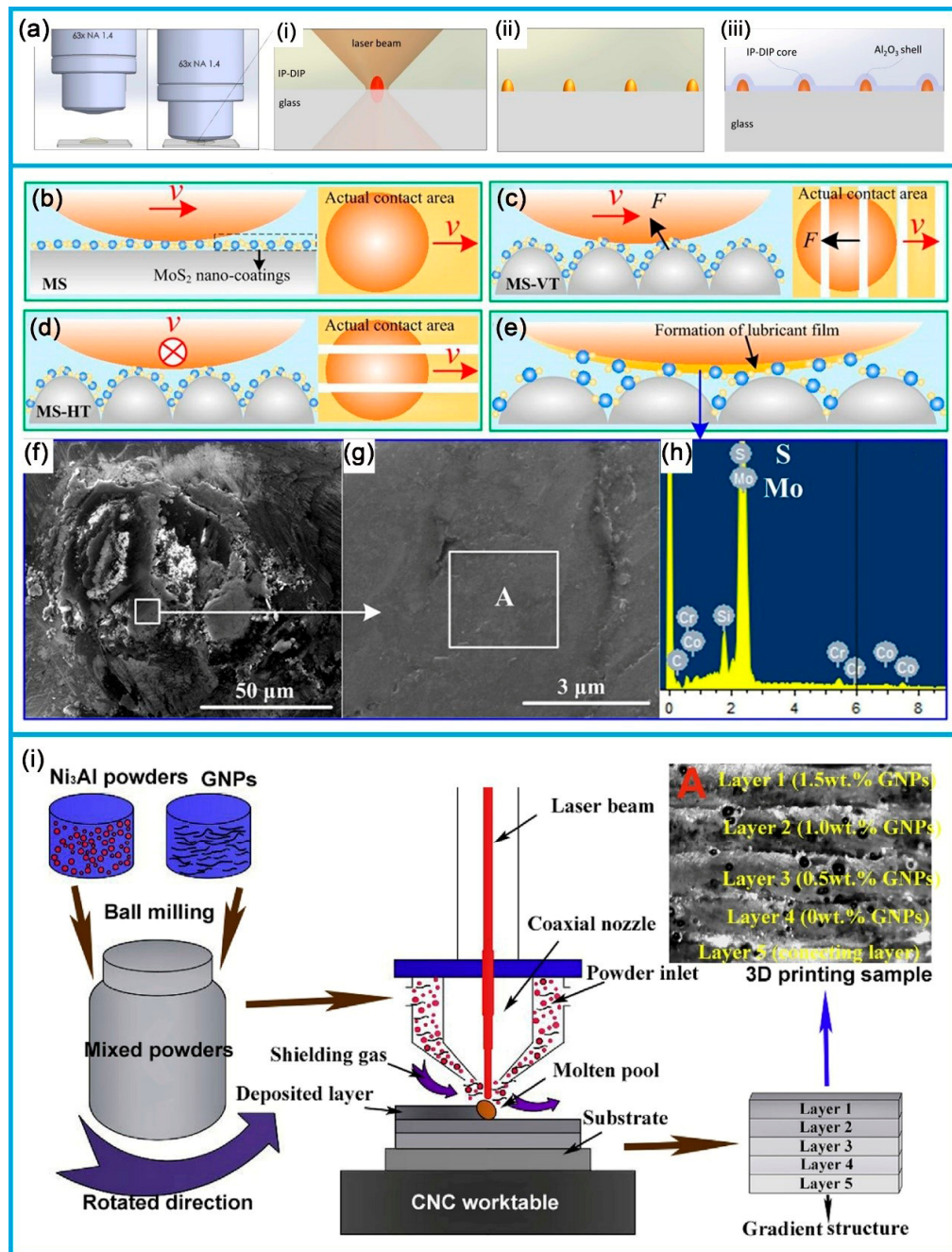
However, the defects in microstructure are still obstacles to the optimization of behaviors of friction and wear for the aforementioned nanocomposites [261]. Driven by such questions, research has been strongly concentrated on the combination of well-designed microstructure and two-dimensional (2D) nanoadditives for exhibiting outstanding tribological characteristics and excellent mechanical properties [262]. Chen et al. [263] successfully fabricated the micro-textured surface with nano-MoS_2 coatings. The results of tribological tests are documented in Table 5, implying that the friction coefficient of the micro-textured surface with nano-MoS_2 coatings was 22.6% lower than that of the untextured specimen. Li et al. [264] studied the effect of surface textures and nano-WS_2 films on the friction and wear properties of ZrO_2 coatings. The combination of WS_2 films and grid-like grooves endowed the ZrO_2 coatings with excellent tribological performances. This texture contributed to prolonging the wear life of WS_2 film and improving its lubricating effect. For the case of texture/WS_2 systems, the friction coefficient and counterpart ball wear rate were reduced by ~16% and ~92%, respectively, if compared to untreated ZrO_2 coatings. Explorations on the tribological properties of microgrooves coated with a few layers of graphene on steel surfaces have been carried out [265]. The graphene lubrication with proper groove area ratios (35%) demonstrated an obvious improvement in the friction behavior, and the low coefficient of friction, around 0.22, remained for 870 sliding cycles. Such friction-reducing behavior was primarily associated with the effectiveness of wear debris interception for microgrooves and the formation of a protective carbon layer.

It is worth mentioning that the surface micro-texture of materials is the key to controlling the surface composition and interfacial properties to minimise friction and extend wear-proof life [268]. Wu et al. [269] reported the macro-tribological performances of Pt cylinder arrays and graphene on the SiO_2/Si substrate. As for the Pt/graphene/SiO_2/Si systems, graphene served as an adhesion layer between Pt arrays and the substrate, performing a support role for Pt cylinders. Correspondingly, the Pt cylinders provided a strong pinning effect for effectively preventing the graphene from sliding during wear. Hence, the synergistic action between graphene and Pt cylinders endowed the SiO_2/Si observable improvement in macro-tribological performances. Surface texture is a feasible way to improve the tribological behavior of films, but it still remains a challenge in precisely controlling the texture size and seeking an appropriate size for promoting the tribological behavior.

Analogously, Xing et al. [266] systematically evaluated the tribological performances of laser-induced periodic surface structures (LIPSS) coated with nano-MoS_2 films. Comparisons on the friction behaviors of nano-grooves parallel (HT) or perpendicular (VT) to the sliding direction were conducted in the cases with or without MoS_2 (MS) coating. Figure 6b–e illustrate the synergistic lubrication mechanism of texture and MoS_2 coating in detail. For the nano-MoS_2-coated samples (MS, MS-VT, and MS-HT), the formation of lubricant film on the contact interfaces performed a dominant role in the friction reduction (Figure 6e). SEM and EDS analyses of the counterpart in Figure 6f–h confirmed that such film was composed of MoS_2, and the conformal groove structures in MS-HT combined with the lubrication film reduced the actual contact area and adhesion force, thus providing a reliable strategy for generating the optimal friction behavior.

Furthermore, Chen et al. [270] put forward a method for preparing pit texture with tunable size on the surface of graphene-containing carbon film by ion etching through a filter. Test results revealed that this texture greatly contributed to improving the tribological performances of carbon film. Table 5 provides detailed test conditions and tribological performances. Among various texture diameters (10, 60, and 120 µm) and

depths (10, 30, and 60 nm), the combination of a 30 nm depth and a 10 μm diameter gave the carbon film the longest wear life and the optimal friction coefficient. The corresponding friction coefficient was reduced by 73.9%, and the wear life was increased by 40 times compared with the initial carbon film. The proposed wear mechanism was that the formation of a transfer film containing graphene reduced interfacial adhesion and shear, thus leading to a remarkable improvement in the tribological behaviors of the carbon film.

Figure 6. (**a**) Schematic of the preparation IP-DIP/Al$_2$O$_3$ core–shell nanostructure [248]. (**b–e**) Schematic diagram of friction mechanism of MS, MS-VT, MS-HT samples; (**f–h**) SEM/EDS of the counter sample. Reprinted with permission [266]. (**i**) Schematic of fabrication for functionally gradient materials; representative images of optical microscopy [267].

Besides the aforementioned surface texture, advanced functionally graded structures have also been demonstrated to be a feasible approach to optimizing the friction and

wear properties of composites [271,272]. The multilayer graded structure attaches great benefit to improving toughness and decreasing stress concentration while keeping internal strength requirements [273,274]. Lu et al. [267] fabricated gradient structure of graphene nanoplatelet-reinforced Ni$_3$Al composites (GNMMCs) using laser melting deposition. A schematic of the deposition system for fabricating such functional composites has been illustrated in Figure 6i. As shown in this figure, the content of graphene in composites from layer 1 to layer 4 was 1.5 wt.%, 1.0 wt.%, 0.5 wt.%, and 0 wt.%, respectively. The rotating sliding tests at 30 N revealed that GNMMCs possessed better tribological properties in comparison with homogeneous Ni$_3$Al/graphene composites (NMCs). Hence, 2D nanoadditives played a key role in effectively perfecting the hardness distribution of GNMMCs, which was regarded as the root of excellent tribological properties.
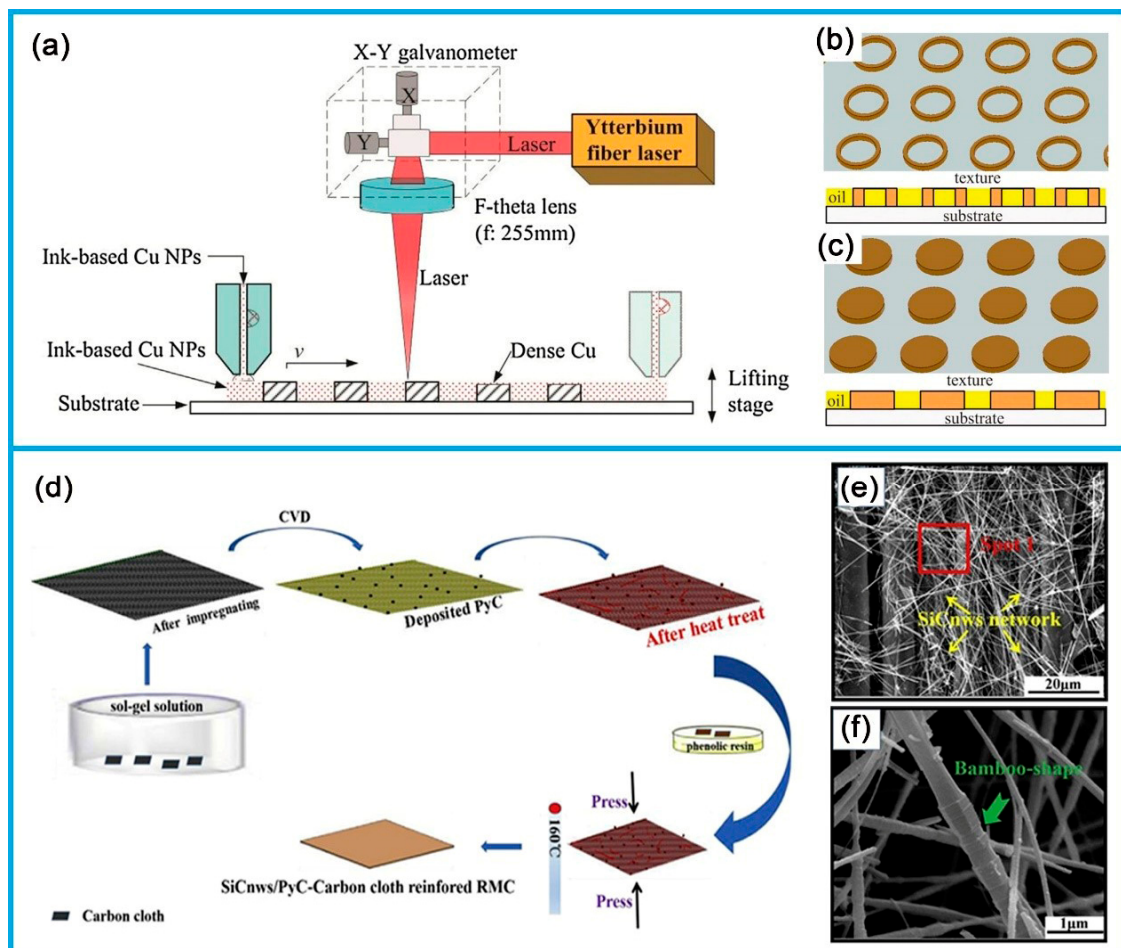
3.2. Wet Friction

In contrast to dry friction, friction between two objects is called wet friction when there is enough liquid between the two contacting surfaces that the two objects do not come into direct contact [275,276]. Advanced materials and surface textures are the two main branches of friction reduction research. To date, various geometrical weaves have been intensively studied, and a wide variety of friction-reducing weaves have been prepared by various processes such as machining, photolithography, etching, ion beam weaving, and laser weaving [277–281]. Shallow holes are artificially distributed on the friction surface, and these act as fluid reservoirs to retain the lubricating film between the mating parts. The fluid film also reduces the increase in temperature during abnormal operation. The shape, size, depth, and distribution of the prepared shallow pores are key factors in reducing friction [282].

Wang et al. [283] reported a process for selective laser melting of ink-printed (SLM-IP) nano-Cu particles to fabricate the dense surface texture on the metallic surface. The experimental set-up of SLM-IP metal nanoparticles is presented in Figure 7a. The disc texture surface (DTS) and ring texture surface (RTS) was designated as the friction testing samples, as shown in Figure 7b,c. In the test under a normal load of 5 N, a sliding speed of 500 rpm, and with the lubricant in an oil, DTS was in possession of a relatively low coefficient of friction compared to RTS and the untreated substrate. This was attributable to the larger effective area of DTS compared to RTS and the lubricating role of the 0D nanoadditive. The dimensional characteristics of surface texture directly affected its friction-reduction properties. Based on such a conclusion, Wang et al. [284] further investigated the role of area ratio on the tribological behaviors of textured matrix. And convex square textures of 400 μm × 400 μm with different spacing (300 μm and 600 μm) were prepared. The specific tribological behaviors and test conditions are recorded in Table 5. The experimental result demonstrated that the friction coefficient of the sample with a spacing of 300 μm was smaller than that of the 600 μm texture. The proposed lubrication mechanism was that the effective contact area of the tribo-pairs decreased with the reduction of spacing, implying that the presence of surface texture played a role in maintaining the distance. Meanwhile, due to the lubrication of soft nanoadditive, excellent tribological performance was observed on the textured composite. Note that although the printed textures exhibited a low friction coefficient, their insufficient adhesion strength remained an obstacle to further improving wear resistance.

Based on the recent exploration of polymer matrix composites, the morphological characteristics of nanoadditives are important for their binding to the matrix structure [286]. The tribological behaviors of single-walled carbon nanotube (SWCNT) reinforced PTFE was reported by Vail et al. [287]. The result demonstrated PTFE nanocomposites filled with 5 wt.% SWCNTs exhibited excellent tribological properties: the wear resistance is increased by more than 20 times the unfilled polymer, as shown in Table 5. Although a dramatic improvement in wear resistance had been obtained, the friction reduction ability was limited due to the lacked surface characteristics of nanotubes. Further investigation demonstrated that high aspect ratio carbon nanotubes (HARC) possessed a morphology

more similar to polymer chains if compared to the low aspect ratio CNTs [288], leading to stronger interaction between HARC and the polymer. The tight binding of HARCs to polymer and their self-entangled compacted structures hindered the removal of wear debris and the relative movement of polymer chains. Hence, observable decreases in friction coefficients and wear rates were detected. The detailed value for such a friction coefficient is recorded in Table 5.

Figure 7. (**a**) Experimental device for SLM-IP metal nanoparticles; textures shape: (**b**) ring texture surface (rTS), (**c**) disc texture surface (dTS) [283]. (**d**) Experimental methods for the preparation of PyC/SiCnws-CFRRMC; micromorphology of in situ grown SiCnws on CF at low magnification (**e**) and at high magnification (**f**) [285].

Taking into account the increasingly advanced surface modification technology, pyrogenic carbon-modified silicon carbide nanowires (PyC/SiCnws) have been proven to be the ideal candidates for improving the tribological behaviors of carbon fiber-reinforced resin matrix composites (CFRRMC) [285]. Figure 7d amply displayed the process of the experiment for fabricating PyC/SiCnws-CFRRMC. The overall morphology of in situ synthetic, in Figure 7e, indicated that a large number of bamboo-like SiCnws (Figure 7f) were randomly distributed on the surface of carbon fiber (CF) to form a network structure. Such structure demonstrated a feasible method to enhance wettability and interfacial adhesion strength between CF and resin, as well as tribological properties. The detailed values of the wear rate and friction coefficient are presented in Table 5.

Based on the superior-natured ceramics, which are characterised by their lightness, thermal insulation, and high strength, research in recent years has strongly concentrated on developing the full potential of ceramic-based composites in tribology [289]. However, high brittleness was still an obstacle for ceramics to obtain excellent wear-resisting performance.

The toughening effect provided by the 1D nanoadditives played a leading role in inhibiting the growth of wear-induced cracks. Candelario et al. [290] studied the roles of CNTs on the wear behaviors of SiC-nanoceramics. Thanks to the addition of the CNTs, the friction and the wear of nanoceramics decreased by 53% and ~93.2%, respectively. The values of the friction coefficient and the wear rate have been concretely presented in Table 5. A proposed wear mechanism for the highly desirable tribological performances of SiC/CNTs was the synergistic effect of the lubrication and toughening functions provided by CNTs. The former reduced the severity of the sliding-contact conditions; the latter reinforced the nanostructure, thereby hindering the propagation and coalescence of the short cracks that eventually nucleate at grain boundaries.

Superhydrophobic surfaces have significant technological potential in various applications. Tribological properties play an important role in many applications that require waterproofing performance. The progress of nanotechnology has stimulated the development of new materials and surface design, such as the application of the "lotus effect". These surfaces require hydrophobic surfaces and interfaces with low adhesion and friction. In micro/nanoscale applications, the two key surface characteristics of materials are non-wetting and low actual contact area. An essential factor in controlling adhesion and friction in dry/wet contact is the actual contact area. The actual contact area depends on the surface roughness and mechanical properties of the material surface and needs to be reduced. As the roughness increases, the number of concave and convex surfaces in contact decreases, leading to a decrease in the actual contact area. Introducing roughness increases hydrophobicity or hydrophilicity, respectively. Under different humidity conditions, the decrease in contact area results in a decrease in the value of adhesion force and friction coefficient from the film to the lotus type [291].
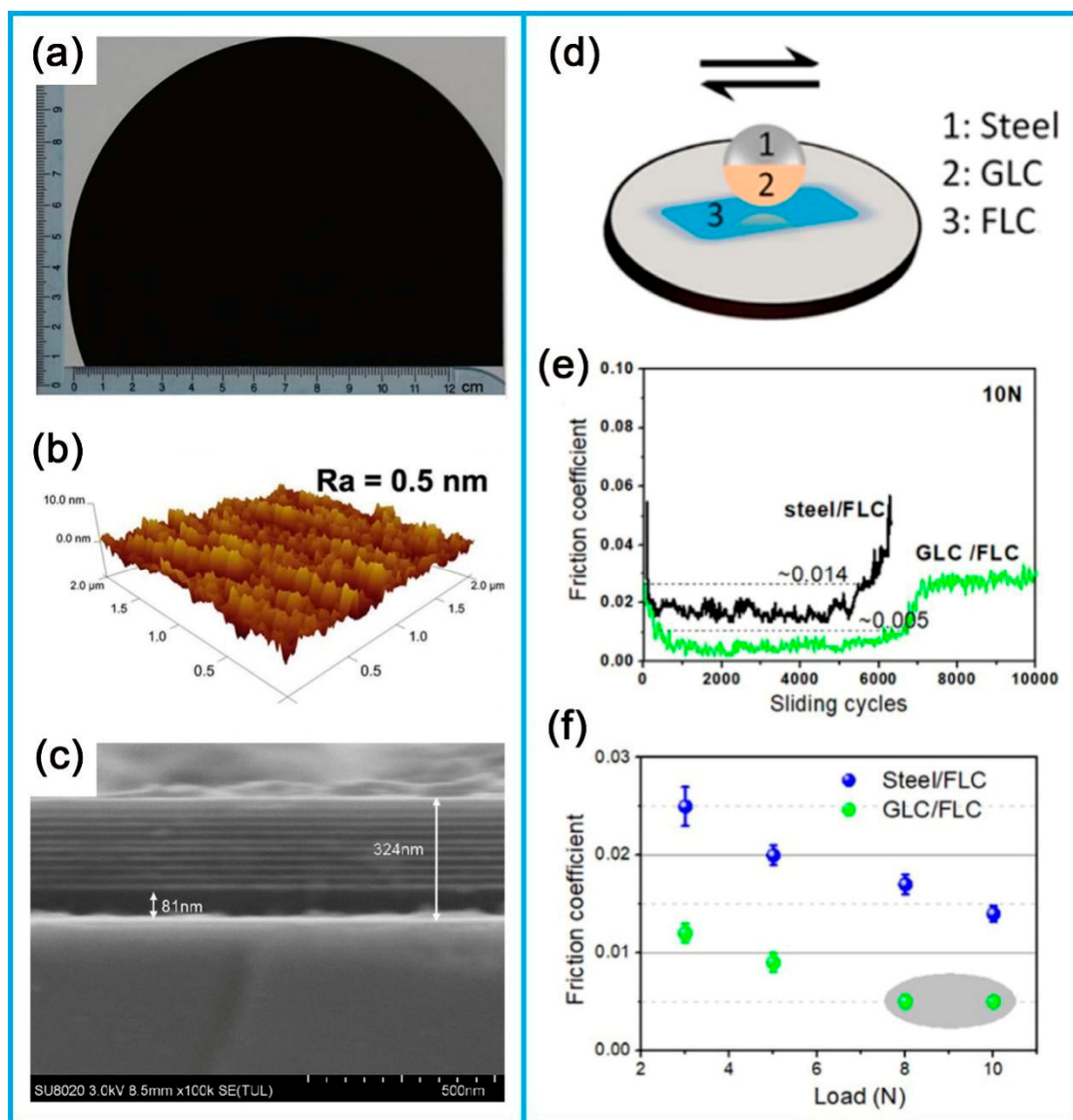
3.3. Ultra-Lubrication

According to statistics, the energy consumption caused by friction accounts for about 33% of the global energy consumption, and more than 60% of mechanical materials losses are caused by wear [292,293]. It is, therefore, imperative to design mechanical systems with very low friction properties and to establish superlubrication mechanisms [294]. Driven by the issues, ultra-lubrication has become an active topic in many domains and has garnered considerable attention from many research groups. An adequate approach is to precipitate protective coatings or thin films on the surface of mechanical parts to reduce friction and improve wear resistance properties [295,296].

Carbon-based thin films have excellent thermal, optical, mechanical, and electronic performances [297–299]. In particular, diamond-like carbon (DLC) films have attracted scientific and technological attention owing to their outstanding performances, such as their low friction coefficient, excellent anti-wear properties, and high chemical inertness [300–302]. In addition, the properties that can be obtained at low temperatures with this deposition process, which can be grown on wide substrates, resulted in the widespread adoption of DLC films in industry [303,304]. In addition, various methods, such as doping with metallic and non-metallic elements, heat treatment, and the addition of nanostructures, have been used to enhance the frictional and mechanical performances of DLC films [305–307]. The ultra-lubrication of such film was further demonstrated by Cao et al. [308] to be dependent on the forming of onion-like structures in the contact interface. Figure 8a,b show the optical and local morphology of the film, respectively. It enabled the observation of a uniform, dense, hydrogenated, amorphous carbon film deposited on the silicon substrate. However, the ultra-lubrication of fullerene-like hydrogenated carbon (FL-C:H) films can only be measured at room temperature.

Therefore, Wang et al. [309] annealed FL-C:H thin films under nitrogen protection. The tribological experiments were conducted under the conditions of a load of 32 N, sliding stroke of 5 mm, and sliding frequency of 2 Hz. The results showed that the film still had ultra-lubrication properties after annealing treatment, and the friction coefficients were

lower than 0.01. The reductions in friction coefficients were ascribed to the fact that curved graphene could form spiral graphene between contact surfaces.

Figure 8. (**a**) Optical diagram of hydrogenated amorphous carbon film containing nanodiamond particles deposited on Si substrate; (**b**) AFM images of local morphologies (2 μm × 2 μm) for the film [308]. (**c**) FESEM image of cross-section for GL/MoS$_2$-200 [310]. (**d**) Schematic diagram of GLC and fullerene-like carbon pair; (**e**) friction coefficient of the pair at 10 N; (**f**) friction coefficient of the pair with increasing load during the stabilization process [311].

Two-dimensional structures have attracted considerable attention owing to weaker shear strength between layers, conferring good tribological properties to the corresponding composites. Martin et al. [312] gained ultra-low friction coefficients of less than 0.002 for the MoS$_2$ films at high vacuum conditions, observed the wear debris by transmission electron microscopy, and found that the MoS$_2$ crystals overlap and rotate at an angle during friction. Thus, the disproportionate contact between the MoS$_2$ crystals may be a real cause for the ultra-lubrication. Chhowalla et al. [313] successfully fabricated films composed of fullerene-like MoS$_2$ spherical particles with friction coefficients as low as 0.003 in the humid air. The cause of ultra-lubrication of the fullerene-like MoS$_2$ films was that the curved S-Mo-S structure effectually prevented surface oxidation and protected laminate structure.

Graphite and MoS$_2$ had very analogous lamellar structures with complementary physical performances [314]. Under certain circumstances, ultra-lubrication could be achieved with crystalline graphite due to the disproportionate contact between the atomic sheets [315]. It is important to note that although the multilayer structure exhibits an ultra-low coefficient of friction, its lack of load-bearing capacity and wear resistance is still not adapted for the actual working conditions.

As most devices operated in humid air, Gong et al. [310] was the first organization, which used water molecules in the air to participate in friction to achieve superlubrication on an engineering scale. Graphiticlike amorphous carbon with short-range graphene sheets and MoS$_2$ (GL/MoS$_2$) hierarchically structure films were fabricated using the combination of pulsed current plasma chemical vapor deposition and medium frequency unbalanced magnetron sputtering. The coefficient of friction for films as a function of sliding time in moist air with contact loads of 2 N and 10 N and a sliding speed of 0.2 m/s was given in Figure 8c. The coefficient of friction of the GL/MoS$_2$ samples became smaller and smaller as the temperature increased from 200 °C to 600 °C, as shown in Table 5. In particular, changing the contact load from 2 N to 10 N resulted in an extremely low friction coefficient of approximately 0.004 for GL/MoS$_2$ at 600 °C.

Similar to the carbon nanostructures described above, researchers proposed to achieve macroscopic superlubrication through the formation of the spherical geometry at the sliding interface to induce nanodot contact [316]. Thus, Li et al. [311] explored the sliding interface of friction pairs consisting of graphite and fullerene-like hydrogenated carbon films (Figure 8d) into graphene nanoscrolls with enhanced macroscopic superlubricity (~0.005). A decreasing trend of COF as an augmenting load could be observed (Figure 8f). In particular, ultra-low friction could be achieved until the graphite-like carbon (GLC) is worn under a load of 8 N (Figure 8e). The strategy of depositing GLC on steel balls enabled longer wear lifespan and lower friction coefficients in dry N$_2$ gas to be obtained (Figure 8d,e).

Unlike in the past, where friction was reduced by adding lubricants and designing microstructures, the focus of technology is now shifting towards environmentally friendly green lubrication. Nurmi et al. [317] proposed a new concept of green lubrication, which used a bimolecular layer of water and surrounding air as a lubricant between hydrophilic and superhydrophobic surfaces to achieve superlubrication. The formation of the lubricating bilayer was achieved by utilizing the unique characteristics of two surfaces: the hydrophilic surface ensured the adhesion and complete diffusion of the lubricating water layer, while the superhydrophobic surface was responsible for maintaining the air layer and reduced friction. This directly reduces the contact angle hysteresis force and may cause more slip to reduce the viscous force. The rough surface formed a smooth interface with air, which reduced friction and provided better performance. Superhydrophobic lubrication was suitable for different sizes and shapes.

3.4. Application of Frictions

Friction is an integral part of extensive fields such as biology, materials science, and mechanical engineering [318,319]. Therefore, the usage of solid and/or liquid lubricants is efficient and effective in decreasing friction and minimising energy loss [320–322]. Alloys have a coefficient of friction of up to 0.5–0.8 at dry friction conditions and have poor tribological properties. The poor tribological properties of alloys arise when in contact with other metallic materials owing to severe adhesive wear, plastic deformation, and metal abrasion. Surface modification methods are, therefore, essential to enhance the tribological performances of the alloys.

Surface microweaving is a feasible surface modification approach for improving tribological properties and reducing fuel consumption. Surface microweaving has been successfully used for mechanical seals [55,323], thrust bearings [324], and cylinder liners/piston rings [325]. Numerous works demonstrated that tribological property can be effectively improved by appropriate surface microweaving [245,326]. In recent years, graphene and its related materials as potential solid lubricants have been explored because

they show great potential in decreasing friction from the nano- to macroscale [327,328]. The use of several layers of graphene as lubricants can significantly reduce friction and wear on sliding steel surfaces in air [329]. In addition to lubrication, they have shown promising potential in various applications such as hydrogen storage, adsorbents, catalyst carriers, and fillers for high-strength structural materials, which has sparked significant interest in graphene nanosheets (GNS) [330]. GNS are helical multilayer structures with unbonded layers, open ends, and adjustable core dimensions formed by rolling continuous sheets of single-layer graphene. The structural features, as well as the exceptional electronic, thermal, anticorrosive, and mechanical properties of graphene, render it appealing for a wide range of applications, including lubrication, hydrogen storage, water and ion channels, supercapacitors, batteries, sensors, and electronic devices [330].

With the development of synthetic technologies, the industrial production of carbon nanotube (CNT) sheets has reached a considerable level, making them suitable for the development of ultra-lightweight structural materials [331]. To translate the specific mechanical performances of individual carbon nanotubes [332] onto thin sheets of carbon nanotubes, researchers have made considerable efforts to manipulate the carbon nanotubes by stretching them in random orientations, which are characteristic of pristine carbon nanotubes [333]. Recent atomic resolution transmission electron microscopy has revealed a large number of folded CNTs on stretched-thin sheets that are aligned, populated, and free of catalyst particles. The high concentration of oriented carbon nanotubes prepared is of interest for the development of super-strong composites, which are expected to compete with carbon fibers.

Achieving low friction and wear between moving surfaces has significant physical and technological benefits, as they are directly related to the efficiency, life, and accuracy of mechanical systems [310,334,335]. Superlubricity, a method of eliminating sliding friction first proposed by Hirano in the 1990s, is an important means of essentially solving friction and wear [59]. Until now, the superlubricity phenomenon has been observed in one-dimensional (carbon nanotubes, graphene nanoscrolls) and two-dimensional (highly oriented pyrolytic graphite (HOPG), MoS_2 monolayers, graphene, etc.) materials [61,336–338]. In these materials, a carefully prepared C-plane exhibits near-zero friction under incommensurate contact, which is also referred to as structure superlubricity [61]. However, most industrial applications require additional performances such as larger size, load-carrying capacity, and environmental as well as humidity stability [337,338]. Diamond-like carbon (DLC) can significantly reduce the coefficient of friction (~0.01 in dry and vacuum environments), extend the life of moving parts, meet industrialization requirements, and is the most promising material for structural superlubrication [339]. In recent years, efforts have been made to design special nanostructures in DLC to realize macroscopic superlubricity. Nanostructure DLC films benefitted from special nanostructures, including fullerene-like carbon [340,341], graphene sheets [342], and dual nanostructures [343], have made obvious progress in low friction wear. Among carbon-based structures, the fullerene family is considered to have significant applications as advanced nanolubricants owing to their unique spherical structure and high chemical stability [344].

Table 5. Synergistic tribological performances of microstructure and nanoadditives.

Matrix/Structure	Reinforcement	Tested Conditions	Tribological Results	
			COF	Wear
SiC-nanoceramic	CNT [290]	Si_3N_4 ball (ball-on-three-disks, 150 N, 100 rpm, paraffin oil)	0.12	Wear rate: ~9.6×10^{-10} mm^3/mN
AZ61 magnesium alloy	CNTs [257]	block (ring on block, 50 N, 140 rpm speed, 10 min)	~0.22	Volumetric loss: 0.96 mm^3

Table 5. *Cont.*

Matrix/Structure	Reinforcement	Tested Conditions	Tribological Results	
			COF	Wear
PTFE coating	CF [259]	1045 steel ball (ball-on-disk, 10 N, 200 rpm, 30 min)	~0.175	Wear rate: ~2.74×10^{-4} mm^3/Nm
PTFE	CNF [260]	45 steel (ring-on-ring, 200 N, 30 min, 25 °C, 1.4 m/s, humidity: $50 \pm 5\%$)	~0.16	Volumetric loss: ~9.7 mm^3
PTFE	SWCNT [287]	304 stainless steel (linear reciprocating friction, 250 N, 50.8 mm/s, 25.4 mm)	~0.19	Wear rate: ~3.0×10^{-5} mm^3/Nm
UHMWPE	CNT [288]	EN-31 forged steel ball (ball-on-disc, 5 N, 200 rpm, 120 min)	~0.12	Wear rate: ~9.46×10^{-5} mm^3/Nm
Dimple texture	Nano-MoS$_2$ [263]	Nodular cast iron pin (pin-on-disc, 10 N, 0.05 m/s, 20 °C)	0.48	Wear rate: ~3.5×10^{-6} mm^3/Nm
Pit texture	Graphene [270]	Si$_3$N$_4$ ball (pin-on-disk, 1 N, 180 rpm, RT)	~0.06	Wear life: 12,000 cycles
The convex textures	Copper nanoparticles [284]	Stainless steel ball (pin-on-disc, 20 N, oil lubrication, RT)	~0.12	NM
Network structure	SiCnws [285]	Steel ball (ball-on-disks, 120 min, lubricating oil, RT)	~0.22971	Wear rate: ~0.08171×10^{-6} mm^3/Nm
Onion structure	Nanodiamond particles [308]	Al$_2$O$_3$ ball (2.89 Gpa, 1800s)	~0.009	NM
Hierarchical structure	Graphene sheets and MoS$_2$ [310]	Al$_2$O$_3$ ball (ball-on-disc, 10 N, 0.2 m/s, RT)	~0.004	NM

RT = room temperature; NM = not mentioned.

4. Conclusions and Outlooks

The stunning surfaces are created by nature for scientists to emulate. In recent years, bionic structures have also made considerable progress in hydrophobic and tribological fields. This paper first describes surface wettability, the factors affecting wettability properties, and wettability models. The wettability of the surface can be powerfully regulated by factors such as surface chemistry, free energy, morphology, and liquid properties. The structure, morphology, and shape of the material have a dramatic impact on the chemical and physical properties of materials. The hydrophobic effects, mechanisms, and applications of biomimetic structures are discussed based on the above-mentioned bio-microstructural principles. The development of both superhydrophobicity and surface functionality on these surfaces is achieved through precise surface chemistry and meticulously organized surface structures. This indicates that bionanomaterials are registering significant progress in the laboratory, but a number of difficulties, such as durability, complexity of technical operation, and cost, need to be addressed before they can be commercialized.

In addition, the design of a biomimetic structure offers a wide range of applications for controlling friction and wear. The research, development, and improvement of the performance of engineered tribological substrates have gained significant attention in recent years in bionic tribology research through investigating the mechanisms of friction reduction, anti-adhesion, anti-wear, and the efficient lubrication of biological systems, drawing upon successes and laws of biology from metrology, physics, materials science, and control. Rationally designing geometric patterns with specific dimensions and arrangements can reduce the friction and wear performances of the part surface, which facilitates surface

weaving to reduce the actual contact area between the wear surfaces and reduce and stabilize the friction force and friction coefficient. Furthermore, lubricants, owing to their excellent performances, show approving tribological performance even under demanding conditions, including high temperatures and vacuums. The combination of biomimetic weaves and lubricants inspired by biological structures can result in remarkable tribological properties. The potential of surface weaving and solid lubricant coating technologies hold great promise; however, their limitations become particularly apparent under conditions of high load and low speed. Under these conditions, surface woven and solid lubricated coatings may wear rapidly, which may cause the formation of wear debris, thereby accelerating wear and part failure and leading to the deterioration of the frictional wear performances of the material. Several successful tribological applications of biomimetic structures in materials are presented. The results of this study will contribute to a better comprehension of the frictional behavior of composite interfaces and, thus, broaden the applications of composites in diverse industries. The work in this article will contribute to the development of the next generation of bionic tribological applications with superior tribological performances.

Author Contributions: The main work of K.Y. and J.T. was the construction and writing of this paper; H.Z. and J.H. modified the content of the article. H.C. (Hao Chen), Y.X. and R.W. ameliorated the grammar of the article. C.W., M.W. and H.C. (Hongliang Chen) sorted and consulted the relevant literature. All authors have read and agreed to the published version of the manuscript.

Conflicts of Interest: The authors declare that they have no known competing financial interests or personal relationships that could have appeared to influence the work reported in this paper.

References

1. Liu, Y.; Qi, Y.; Sun, H.; Han, N.; Zhou, J.; Song, J.; Zou, M. Bionic design of thin-walled tubes inspired by the vascular structure of bamboo. *Thin-Walled Struct.* **2023**, *186*, 110689. [CrossRef]
2. Zhang, R.; Sun, X.; Han, D.; Zhang, R.; Zhang, H.; Ma, J.; Wen, L.; Zou, M. A bionic mechanical foot with adaptive variable postures travelling on sand. *J. Terramechanics* **2023**, *107*, 61–74. [CrossRef]
3. Jiang, J.; Yao, Z.; Li, Z.; Lu, Y.; Yao, Q.; Gong, X.; Fu, X.; Duan, F. Recognition method for the bionic camouflage cetacean whistle modulated by CPMFSK signals. *Appl. Acoust.* **2023**, *207*, 109326. [CrossRef]
4. Yan, Z.; Yang, H.; Zhang, W.; Lin, F.; Gong, Q.; Zhang, Y. Bionic fish tail design and trajectory tracking control. *Ocean Eng.* **2022**, *257*, 111659. [CrossRef]
5. Sun, S.; Zhi, Y.; Li, X.; Guo, Z. Numerical investigation on cavitating wake dynamic of a propeller with bionic tubercle leading-edge. *Ocean Eng.* **2022**, *252*, 111240. [CrossRef]
6. Liu, H.; Wang, X.; Lu, Y.; Yan, Y.; Zhao, W.; Wu, X.; Zhang, Z. Application and optimal design of the bionic guide vane to improve the safety serve performances of the reactor coolant pump. *Nucl. Eng. Technol.* **2022**, *54*, 2491–2509. [CrossRef]
7. Huang, S.; Qiu, H.; Wang, Y. Aerodynamic performance of horizontal axis wind turbine with application of dolphin head-shape and lever movement of skeleton bionic airfoils. *Energy Convers. Manag.* **2022**, *267*, 115803. [CrossRef]
8. Wang, B.; Zhu, J.; Xie, T.; Fu, L.; Yang, W.; Li, D.; Zhou, L. A new Cu-W bionic shell pearl multilayer structure. *Surf. Coat. Technol.* **2023**, *461*, 129433. [CrossRef]
9. Wang, Z.; Meng, L.; Li, X.; Li, J. Fabrication of core-shell Ni@C@PANI nanocomposite-based bionic coating with multi-bands EWM adaptability inspired by porous structure of pachliopta aristolochiae wings. *Prog. Org. Coat.* **2023**, *179*, 107498. [CrossRef]
10. Sun, X.; Xu, J.; Qi, Z. Mechanism properties of a bird-neck bionic rigid-flexible structure. *Fundam. Res.* **2022**, *in press*. [CrossRef]
11. Wang, L. A critical review on robust self-cleaning property of lotus leaf. *Soft Matter* **2023**, *19*, 1058–1075. [CrossRef] [PubMed]
12. Wan, J.; Li, H.; Xu, L.; Yan, J.; Liao, Y.; Wang, X. PDA/PEI-induced in-situ growth of a lotus leaf-like TiO$_2$ nanoparticle film on N-halamine cotton fabric for photocatalytic, self-cleaning and efficient antibacterial performance. *Cellulose* **2023**, *30*, 3953–3972. [CrossRef]
13. Sun, J.; Bauman, L.; Yu, L.; Zhao, B. Gecko-and-inchworm-inspired untethered soft robot for climbing on walls and ceilings. *Cell Rep. Phys. Sci.* **2023**, *4*, 101241. [CrossRef]

14. Duan, J.; Wang, B.; Ji, B.; Sun, W.; Wang, Z.; Dai, Z. Control Strategy of Stable Climbing Mechanics for Gecko-Inspired Robot on Vertical Arc Surface. *IEEE Instrum. Meas. Mag.* **2023**, *26*, 48–56. [CrossRef]

15. Zhang, Z.; Chu, Z.; Zhang, B.; Cui, J. Inchworm-Gecko Inspired Robot with Adhesion State Detection and CPG Control. In *Cognitive Systems and Information Processing*; Sun, F., Cangelosi, A., Zhang, J., Yu, Y., Liu, H., Fang, B., Eds.; Springer Nature: Singapore, 2023; pp. 70–84.

16. Sharma, S.K.; Grewal, H.S. Tribological Behavior of Bioinspired Surfaces. *Biomimetics* **2023**, *8*, 62. [CrossRef] [PubMed]

17. Dean, B.; Bhushan, B. Shark-skin surfaces for fluid-drag reduction in turbulent flow: A review. Philosophical Transactions of the Royal Society A: Mathematical. *Phys. Eng. Sci.* **2010**, *368*, 4775–4806.

18. Puukilainen, E.; Koponen, H.-K.; Xiao, Z.; Suvanto, S.; Pakkanen, T.A. Nanostructured and chemically modified hydrophobic polyolefin surfaces. *Colloids Surf. A Physicochem. Eng. Asp.* **2006**, *287*, 175–181. [CrossRef]

19. Zheng, R.; Tshabalala, M.A.; Li, Q.; Wang, H. Construction of hydrophobic wood surfaces by room temperature deposition of rutile (TiO_2) nanostructures. *Appl. Surf. Sci.* **2015**, *328*, 453–458. [CrossRef]

20. Barthlott, W.; Neinhuis, C. Purity of the sacred lotus, or escape from contamination in biological surfaces. *Planta* **1997**, *202*, 1–8. [CrossRef]

21. Schulz, B.; Frommer, W.B. A plant ABC transporter takes the lotus seat. *Science* **2004**, *306*, 622–625. [CrossRef]

22. Su, H.; Luan, B.; Dong, Y.; Zhang, X.; Liu, Z.; Wang, C. Lotus leaf-like Ni-decorated SiC with combined superhydrophobicity and enhanced microwave absorption performance. *Colloids Surf. A Physicochem. Eng. Asp.* **2022**, *650*, 129602. [CrossRef]

23. Yoo, D.; Kim, S.J.; Joung, Y.; Jang, S.; Choi, D.; Kim, D.S. Lotus leaf-inspired droplet-based electricity generator with low-adhesive superhydrophobicity for a wide operational droplet volume range and boosted electricity output. *Nano Energy* **2022**, *99*, 107361. [CrossRef]

24. Klicova, M.; Oulehlova, Z.; Klapstova, A.; Hejda, M.; Krejcik, M.; Novak, O.; Mullerova, J.; Erben, J.; Rosendorf, J.; Palek, R.; et al. Biomimetic hierarchical nanofibrous surfaces inspired by superhydrophobic lotus leaf structure for preventing tissue adhesions. *Mater. Des.* **2022**, *217*, 110661. [CrossRef]

25. Yang, J.; Long, F.; Wang, R.; Zhang, X.; Yang, Y.; Hu, W.; Liu, L. Design of mechanical robust superhydrophobic Cu coatings with excellent corrosion resistance and self-cleaning performance inspired by lotus leaf. *Colloids Surf. A Physicochem. Eng. Asp.* **2021**, *627*, 127154. [CrossRef]

26. Shao, Y.; Zhao, J.; Fan, Y.; Wan, Z.; Lu, L.; Zhang, Z.; Ming, W.; Ren, L. Shape memory superhydrophobic surface with switchable transition between "Lotus Effect" to "Rose Petal Effect". *Chem. Eng. J.* **2020**, *382*, 122989. [CrossRef]

27. Ebert, D.; Bhushan, B. Wear-resistant rose petal-effect surfaces with superhydrophobicity and high droplet adhesion using hydrophobic and hydrophilic nanoparticles. *J. Colloid Interface Sci.* **2012**, *384*, 182–188. [CrossRef] [PubMed]

28. Gao, D.; Xin, B.; Zhang, Z.; Wang, Y.; Yu, W.; Hou, C.; Jiang, Y.; Huang, P.; Xu, W. Study on the Preparation of Special Wettability Nanofiber Membranes and Its Application in Oil-water Separation. *J. Phys. Conf. Ser.* **2023**, *2437*, 12037. [CrossRef]

29. Nosonovsky, M.; Bhushan, B. Superhydrophobic surfaces and emerging applications: Non-adhesion, energy, green engineering. *Curr. Opin. Colloid Interface Sci.* **2009**, *14*, 270–280. [CrossRef]

30. Huang, F.; Motalleh, B.; Wang, D.; Cornelius, C.J. Tailoring intrinsic hydrophobicity and surface energy on rough surface via low-T Cassie–Wenzel wetting transition method. *AIChE J.* **2023**, *69*, e17908. [CrossRef]

31. Drelich, J.; Marmur, A. Physics and applications of superhydrophobic and superhydrophilic surfaces and coatings. *Surf. Innov.* **2014**, *2*, 211–227. [CrossRef]

32. Yin, K.; Yang, S.; Dong, X.; Chu, D.; Duan, J.-A.; He, J. Ultrafast achievement of a superhydrophilic/hydrophobic janus foam by femtosecond laser ablation for directional water transport and efficient fog harvesting. *ACS Appl. Mater. Interfaces* **2018**, *10*, 31433–31440. [CrossRef] [PubMed]

33. Feng, L.; Zhang, Y.; Xi, J.; Zhu, Y.; Wang, N.; Xia, F.; Jiang, L. Petal effect: A superhydrophobic state with high adhesive force. *Langmuir* **2008**, *24*, 4114–4119. [CrossRef]

34. Parker, A.R.; Lawrence, C.R. Water capture by a desert beetle. *Nature* **2001**, *414*, 33–34. [CrossRef]

35. Qin, S.; Shi, X.; Xue, Y.; Zhang, K.; Huang, Q.; Wu, C.; Ma, J.; Shu, J. Coupling effects of bionic textures with composite solid lubricants to improve tribological properties of TC4 alloy. *Tribol. Int.* **2022**, *173*, 107691. [CrossRef]

36. Wang, Z.; Fu, Q.; Wood, R.J.; Wu, J.; Wang, S. Influence of bionic non-smooth surface texture on tribological characteristics of carbon-fiber-reinforced polyetheretherketone under seawater lubrication. *Tribol. Int.* **2020**, *144*, 106100. [CrossRef]

37. Yang, K.; Ma, H.; Zhao, W.; Li, X.; Liu, H. Investigation of the preparation and tribological behavior of a frictional interface covered with sinusoidal microchannels containing SnAgCu and Ti_3SiC_2. *Tribol. Int.* **2020**, *150*, 106368. [CrossRef]

38. Zhou, J.; Zhao, G.; Li, J.; Chen, J.; Zhang, S.; Wang, J.; Walsh, F.C.; Wang, S.; Xue, Y. Electroplating of non-fluorinated superhydrophobic Ni/WC/WS2 composite coatings with high abrasive resistance. *Appl. Surf. Sci.* **2019**, *487*, 1329–1340. [CrossRef]

39. Liu, X.; Liang, Y.; Zhou, F.; Liu, W. Extreme wettability and tunable adhesion: Biomimicking beyond nature? *Soft Matter* **2012**, *8*, 2070–2086. [CrossRef]

40. Jucius, D.; Guobienė, A.; Grigaliūnas, V. Surface texturing of polytetrafluoroethylene by hot embossing. *Appl. Surf. Sci.* **2010**, *256*, 2164–2169. [CrossRef]

41. Khan, A.; Wang, Z.; Sheikh, M.A.; Whitehead, D.J.; Li, L. Laser micro/nano patterning of hydrophobic surface by contact particle lens array. *Appl. Surf. Sci.* **2011**, *258*, 774–779. [CrossRef]

42. Marchetto, D.; Rota, A.; Calabri, L.; Gazzadi, G.C.; Menozzi, C.; Valeri, S. Hydrophobic effect of surface patterning on Si surface. *Wear* **2010**, *268*, 488–492. [CrossRef]

43. Zhao, W.; Wang, L.; Xue, Q. Design and fabrication of nanopillar patterned Au textures for improving nanotribological performance. *ACS Appl. Mater. Interfaces* **2010**, *2*, 788–794. [CrossRef] [PubMed]

44. Zhang, X.; Zhong, X.; Meng, X.; Yi, G.; Jia, J. Adhesion and friction studies of nano-textured surfaces produced by self-assembling Au nanoparticles on silicon wafers. *Tribol. Lett.* **2012**, *46*, 65–73. [CrossRef]

45. Ding, Q.; Wang, L.; Wang, Y.; Wang, S.; Hu, L.; Xue, Q. Improved tribological behavior of DLC films under water lubrication by surface texturing. *Tribol. Lett.* **2011**, *41*, 439–449. [CrossRef]

46. Man, H.C.; Chiu, K.; Guo, X. Laser surface micro-drilling and texturing of metals for improvement of adhesion joint strength. *Appl. Surf. Sci.* **2010**, *256*, 3166–3169. [CrossRef]

47. Luo, K.; Wang, C.; Li, Y.; Luo, M.; Huang, S.; Hua, X.; Lu, J. Effects of laser shock peening and groove spacing on the wear behavior of non-smooth surface fabricated by laser surface texturing. *Appl. Surf. Sci.* **2014**, *313*, 600–606. [CrossRef]

48. Maksimov, S. An integral method to study textures of nanosized crystallites in an electron microscope column. *Inorg. Mater.* **2009**, *45*, 1598–1609. [CrossRef]

49. Daniel, M.-C.; Astruc, D. Gold nanoparticles: Assembly; supramolecular chemistry; quantum-size-related properties, and applications toward biology, catalysis, and nanotechnology. *Chem. Rev.* **2004**, *104*, 293–346. [CrossRef]

50. Hu, H.; Chen, H.; Yu, S.; Chen, J.; Wu, G.; Meng, F.; Qu, J.; Li, Y.; Zhu, H.; Xiao, J.Q. Textured Co nanowire arrays with controlled magnetization direction. *J. Magn. Magn. Mater.* **2005**, *295*, 257–262. [CrossRef]

51. Wang, S.; Pang, X.; Guo, X.; Cheng, C.; Liu, Y.; Zhang, Y. Mechanical and tribological properties of WC particles reinforced Cu-20Zn matrix composites. *Powder Technol.* **2022**, *406*, 117571. [CrossRef]

52. Yang, K.; Zhang, F.; Chen, Y.; Zhang, H.; Xiong, B.; Chen, H. Recent progress on carbon-based composites in multidimensional applications. *Compos. Part A Appl. Sci. Manuf.* **2022**, *157*, 106906. [CrossRef]

53. Chen, Y.; Yang, K.; Lin, H.; Zhang, F.; Xiong, B.; Zhang, H.; Zhang, C. Important contributions of multidimensional nanoadditives on the tribofilms: From formation mechanism to tribological behaviors. *Compos. Part B Eng.* **2022**, *234*, 109732. [CrossRef]

54. Chouquet, C.; Gavillet, J.; Ducros, C.; Sanchette, F. Effect of DLC surface texturing on friction and wear during lubricated sliding. *Mater. Chem. Phys.* **2010**, *123*, 367–371. [CrossRef]

55. Tang, W.; Zhou, Y.; Zhu, H.; Yang, H. The effect of surface texturing on reducing the friction and wear of steel under lubricated sliding contact. *Appl. Surf. Sci.* **2013**, *273*, 199–204. [CrossRef]

56. Yang, K.; Ma, H.; Cao, S.; Li, X.; Li, A.; Cao, Z. Analysis of friction interfaces with sinusoidal microchannels and the hybrid lubrication mechanisms of a tribo-film. *Appl. Surf. Sci.* **2020**, *525*, 146502. [CrossRef]

57. Yang, K.; Zhang, F.; Ma, Y.; Cao, Z.; Ma, H.; Zhang, C.; Liang, Y. Simple synthesis of the composite coating and the lubrication mechanisms of the spherical SnAgCu–Al$_2$O$_3$. *Wear* **2020**, *462–463*, 203514. [CrossRef]

58. Yang, K.; Ma, H.; Wang, L.; Cao, Z.; Zhang, C. Analysis of self-regulating tribological functions of the MgAl microchannels prepared in the Ti alloys. *Tribol. Int.* **2021**, *154*, 106717. [CrossRef]

59. Hirano, M.; Shinjo, K. Atomistic locking and friction. *Phys. Rev. B* **1990**, *41*, 11837. [CrossRef]

60. Matta, C.; Joly-Pottuz, L.; Bouchet, M.D.B.; Martin, J.; Kano, M.; Zhang, Q. Goddard III, Superlubricity and tribochemistry of polyhydric alcohols. *Phys. Rev. B* **2008**, *78*, 85436. [CrossRef]

61. Yang, J.; Liu, Z.; Grey, F.; Xu, Z.; Li, X.; Liu, Y.; Urbakh, M.; Cheng, Y.; Zheng, Q. Observation of high-speed microscale superlubricity in graphite. *Phys. Rev. Lett.* **2013**, *110*, 255504. [CrossRef]

62. Zhou, S.; Wang, W.; Xu, X. Robust superhydrophobic magnetic melamine sponge inspired by lotus leaf surface for efficient continuous oil-water separation. *Sep. Purif. Technol.* **2023**, *311*, 123251. [CrossRef]

63. Ji, X.-Y.; Wang, J.-W.; Feng, X.-Q. Role of flexibility in the water repellency of water strider legs: Theory and experiment. *Phys. Rev. E* **2012**, *85*, 21607. [CrossRef] [PubMed]

64. Xu, J.; Liu, W.; Shang, W.; Chen, J.; Lian, J. Drop impact dynamic and directional transport on dragonfly wing surface. *Friction* **2023**, *11*, 737–747. [CrossRef]

65. Fang, Y.; Sun, G.; Bi, Y.; Zhi, H. Multiple-dimensional micro/nano structural models for hydrophobicity of butterfly wing surfaces and coupling mechanism. *Sci. Bull.* **2015**, *60*, 256–263. [CrossRef]

66. Li, J.; Guo, Z.; Liu, W. Biomimetic Superhydrophobic Materials Construct from Binary Structure: A Review on Design. Properties, and Applications. *Adv. Mater. Interfaces* **2023**, *10*, 2201847. [CrossRef]

67. Chen, X.; Wang, M.; Xin, Y.; Huang, Y. One-step fabrication of self-cleaning superhydrophobic surfaces: A combined experimental and molecular dynamics study. *Surf. Interfaces* **2022**, *31*, 102022. [CrossRef]

68. Xue, C.-H.; Jia, S.-T.; Zhang, J.; Ma, J.-Z. Large-area fabrication of superhydrophobic surfaces for practical applications: An overview. *Sci. Technol. Adv. Mater.* **2010**, *11*, 33002. [CrossRef]

69. Wang, H.; Zhu, Y.; Hu, Z.; Zhang, X.; Wu, S.; Wang, R.; Zhu, Y. A novel electrodeposition route for fabrication of the superhydrophobic surface with unique self-cleaning, mechanical abrasion and corrosion resistance properties. *Chem. Eng. J.* **2016**, *303*, 37–47. [CrossRef]

70. Scarratt, L.R.; Hoatson, B.S.; Wood, E.S.; Hawkett, B.S.; Neto, C. Durable superhydrophobic surfaces via spontaneous wrinkling of teflon AF. *ACS Appl. Mater. Interfaces* **2016**, *8*, 6743–6750. [CrossRef]

71. Cully, P.; Karasu, F.; Müller, L.; Jauzein, T.; Leterrier, Y. Self-cleaning and wear-resistant polymer nanocomposite surfaces. *Surf. Coat. Technol.* **2018**, *348*, 111–120. [CrossRef]

72. Yang, Z.; Wang, L.; Sun, W.; Li, S.; Zhu, T.; Liu, W.; Liu, G. Superhydrophobic epoxy coating modified by fluorographene used for anti-corrosion and self-cleaning. *Appl. Surf. Sci.* **2017**, *401*, 146–155. [CrossRef]

73. Guo, Z.; Chen, X.; Li, J.; Liu, J.-H.; Huang, X.-J. ZnO/CuO hetero-hierarchical nanotrees array: Hydrothermal preparation and self-cleaning properties. *Langmuir* **2011**, *27*, 6193–6200. [CrossRef] [PubMed]

74. Wu, X.; Silberschmidt, V.V.; Hu, Z.-T.; Chen, Z. When superhydrophobic coatings are icephobic: Role of surface topology. *Surf. Coat. Technol.* **2019**, *358*, 207–214. [CrossRef]

75. Wang, Z.; Sun, Z.; Chen, X.; Zou, W.; Jiang, X.; Sun, D.; Yu, M. Color fastness enhancement of dyed wood by Si-sol@PDMS based superhydrophobic coating. *Colloids Surf. A Physicochem. Eng. Asp.* **2022**, *651*, 129701. [CrossRef]

76. Zhao, J.; Sun, R.; Liu, C.; Mo, J. Application of ZnO/epoxy resin superhydrophobic coating for buoyancy enhancement and drag reduction. *Colloids Surf. A Physicochem. Eng. Asp.* **2022**, *651*, 129714. [CrossRef]

77. Cao, L.; Liu, J.; Xu, S.; Xia, Y.; Huang, W.; Li, Z. Inherent superhydrophobicity of Sn/SnOx films prepared by surface self-passivation of electrodeposited porous dendritic Sn. *Mater. Res. Bull.* **2013**, *48*, 4804–4810. [CrossRef]

78. Bhattacharya, P.; Gohil, S.; Mazher, J.; Ghosh, S.; Ayyub, P. Universal, geometry-driven hydrophobic behaviour of bare metal nanowire clusters. *Nanotechnology* **2008**, *19*, 75709. [CrossRef] [PubMed]

79. Yang, Z.; Liu, X.; Tian, Y. Insights into the wettability transition of nanosecond laser ablated surface under ambient air exposure. *J. Colloid Interface Sci.* **2019**, *533*, 268–277. [CrossRef] [PubMed]

80. Zhang, Z.; Gu, Q.; Jiang, W.; Zhu, H.; Xu, K.; Ren, Y.; Xu, C. Achieving of bionic super-hydrophobicity by electrodepositing nano-Ni-pyramids on the picosecond laser-ablated micro-Cu-cone surface. *Surf. Coat. Technol.* **2019**, *363*, 170–178. [CrossRef]

81. Lin, Y.; Li, T.; Liu, S.; Shi, Q.; Xu, K.; Zhang, Z.; Wu, J. Interfacial mechanical properties of tetrahydrofuran hydrate-solid surfaces: Implications for hydrate management. *J. Colloid Interface Sci.* **2023**, *629*, 326–335. [CrossRef]

82. Jiang, L.; Wang, R.; Yang, B.; Li, T.; Tryk, D.; Fujishima, A.; Hashimoto, K.; Zhu, D. Binary cooperative complementary nanoscale interfacial materials. *Pure Appl. Chem.* **2000**, *72*, 73–81. [CrossRef]

83. Lu, Y. Temperature Dependent Anti-Icing Performance of the Microstructure Surface: Wettability Change and Ice Nucleation. *Coatings* **2023**, *13*, 1485. [CrossRef]

84. Koch, B.M.; Amirfazli, A.; Elliott, J.A. Modeling and measurement of contact angle hysteresis on textured high-contact-angle surfaces. *J. Phys. Chem. C* **2014**, *118*, 18554–18563. [CrossRef]

85. Blake, T.; Fernández-Toledano, J.; De Coninck, J. A possible way to extract the dynamic contact angle at the molecular scale from that measured experimentally. *J. Colloid Interface Sci.* **2023**, *629*, 660–669. [CrossRef]

86. Kumar, P.; Harvie, D.J. Contact Angle Hysteresis on Rough Surfaces Part II: Energy Dissipation via Microscale Interface Dynamics. *arXiv* **2023**, arXiv:2303.09149.

87. Iliev, S.; Pesheva, N.; Iliev, P. Contact angle hysteresis on random self-affine rough surfaces in Wenzel's wetting regime: Numerical study. *Phys. Rev. E* **2023**, *107*, 24802. [CrossRef]

88. Ford, R.; Furmidge, C. Studies at phase interfaces: II. The stabilization of water-in-oil emulsions using oil-soluble emulsifiers. *J. Colloid Interface Sci.* **1966**, *22*, 331–341. [CrossRef]

89. Furmidge, C. Studies at phase interfaces. *I. The sliding of liquid drops on solid surfaces and a theory for spray retention. J. Colloid Sci.* **1962**, *17*, 309–324.

90. Chen, W.; Fadeev, A.Y.; Hsieh, M.C.; Öner, D.; Youngblood, J.; McCarthy, T.J. Ultrahydrophobic and ultralyophobic surfaces: Some comments and examples. *Langmuir* **1999**, *15*, 3395–3399. [CrossRef]

91. Mao-Gang, G.; Yuan-Yue, L.; Xiao-Liang, X. A new model for the formation of contact angle and contact angle hysteresis. *Chin. Phys. B* **2010**, *19*, 106801. [CrossRef]

92. Young, T., III. An essay on the cohesion of fluids. *Philos. Trans. R. Soc. Lond.* **1805**, *95*, 65–87.

93. Wenzel, R.N. Resistance of solid surfaces to wetting by water. *Ind. Eng. Chem.* **1936**, *28*, 988–994. [CrossRef]

94. Bhushan, B. Bioinspired structured surfaces. *Langmuir* **2012**, *28*, 1698–1714. [CrossRef] [PubMed]

95. Bhushan, B.; Jung, Y.C.; Koch, K. Micro-, nano-and hierarchical structures for superhydrophobicity, self-cleaning and low adhesion. Philosophical Transactions of the Royal Society A: Mathematical. *Phys. Eng. Sci.* **2009**, *367*, 1631–1672.

96. Myronyuk, O.; Baklan, D.; Vasilyev, G.S.; Rodin, A.M.; Vanagas, E. Wetting patterns of liquid-repellent femtosecond laser textured aluminum surfaces. *Coatings* **2022**, *12*, 1852. [CrossRef]

97. Ran, C.; Ding, G.; Liu, W.; Deng, Y.; Hou, W. Wetting on nanoporous alumina surface: Transition between Wenzel and Cassie states controlled by surface structure. *Langmuir* **2008**, *24*, 9952–9955. [CrossRef] [PubMed]

98. Cassie, A.; Baxter, S. Wettability of porous surfaces. *Trans. Faraday Soc.* **1944**, *40*, 546–551. [CrossRef]

99. Milne, A.J.B.; Amirfazli, A. The Cassie equation: How it is meant to be used. *Adv. Colloid Interface Sci.* **2012**, *170*, 48–55. [CrossRef]

100. Cai, T.-M.; Jia, Z.-H.; Yang, H.-N.; Wang, G. Investigation of Cassie-Wenzel wetting transitions on microstructured surfaces. *Colloid Polym. Sci.* **2016**, *294*, 833–840. [CrossRef]

101. Murakami, D.; Jinnai, H.; Takahara, A. Wetting transition from the Cassie–Baxter state to the Wenzel state on textured polymer surfaces. *Langmuir* **2014**, *30*, 2061–2067. [CrossRef]

102. Nosonovsky, M.; Bhushan, B. Patterned nonadhesive surfaces: Superhydrophobicity and wetting regime transitions. *Langmuir* **2008**, *24*, 1525–1533. [CrossRef] [PubMed]

103. Jung, Y.C.; Bhushan, B. Dynamic effects of bouncing water droplets on superhydrophobic surfaces. *Langmuir* **2008**, *24*, 6262–6269. [CrossRef] [PubMed]

104. Nosonovsky, M.; Bhushan, B. Energy transitions in superhydrophobicity: Low adhesion, easy flow and bouncing. *J. Phys. Condens. Matter* **2008**, *20*, 395005. [CrossRef]

105. Krupenkin, T.N.; Taylor, J.A.; Schneider, T.M.; Yang, S. From rolling ball to complete wetting: The dynamic tuning of liquids on nanostructured surfaces. *Langmuir* **2004**, *20*, 3824–3827. [CrossRef] [PubMed]

106. Feng, X.; Feng, L.; Jin, M.; Zhai, J.; Jiang, L.; Zhu, D. Reversible super-hydrophobicity to super-hydrophilicity transition of aligned ZnO nanorod films. *J. Am. Chem. Soc.* **2004**, *126*, 62–63. [CrossRef] [PubMed]

107. Bormashenko, E.; Pogreb, R.; Whyman, G.; Erlich, M. Cassie—Wenzel wetting transition in vibrating drops deposited on rough surfaces: Is the dynamic cassie—Wenzel wetting transition a 2d or 1d affair? *Langmuir* **2007**, *23*, 6501–6503. [CrossRef] [PubMed]

108. Lafuma, A.; Quéré, D. Superhydrophobic states. *Nat. Mater.* **2003**, *2*, 457–460. [CrossRef]

109. Extrand, C.W. Model for contact angles and hysteresis on rough and ultraphobic surfaces. *Langmuir* **2002**, *18*, 7991–7999. [CrossRef]

110. Patankar, N.A. Transition between superhydrophobic states on rough surfaces. *Langmuir* **2004**, *20*, 7097–7102. [CrossRef]

111. Gao, N.; Yan, Y. Modeling superhydrophobic contact angles and wetting transition. *J. Bionic Eng.* **2009**, *6*, 335–340. [CrossRef]

112. Nosonovsky, M.; Bhushan, B. Stochastic model for metastable wetting of roughness-induced superhydrophobic surfaces. *Microsyst. Technol.* **2006**, *12*, 231–237. [CrossRef]

113. Nosonovsky, M.; Bhushan, B. Roughness optimization for biomimetic superhydrophobic surfaces. *Microsyst. Technol.* **2005**, *11*, 535–549. [CrossRef]

114. Ishino, C.; Okumura, K. Nucleation scenarios for wetting transition on textured surfaces: The effect of contact angle hysteresis. *EPL (Europhys. Lett.)* **2006**, *76*, 464. [CrossRef]

115. Bormashenko, E.; Bormashenko, Y.; Stein, T.; Whyman, G.; Pogreb, R.; Barkay, Z. Environmental scanning electron microscopy study of the fine structure of the triple line and Cassie—Wenzel wetting transition for sessile drops deposited on rough polymer substrates. *Langmuir* **2007**, *23*, 4378–4382. [CrossRef]

116. Bhushan, B.; Jung, Y.C. Natural and biomimetic artificial surfaces for superhydrophobicity, self-cleaning, low adhesion, and drag reduction. *Prog. Mater. Sci.* **2011**, *56*, 1–108. [CrossRef]

117. Quan, Y.-Y.; Chen, Z.; Lai, Y.; Huang, Z.-S.; Li, H. Recent advances in fabricating durable superhydrophobic surfaces: A review in the aspects of structures and materials. *Mater. Chem. Front.* **2021**, *5*, 1655–1682. [CrossRef]

118. Parvate, S.; Dixit, P.; Chattopadhyay, S. Superhydrophobic surfaces: Insights from theory and experiment. *J. Phys. Chem. B* **2020**, *124*, 1323–1360. [CrossRef]

119. Zeng, Q.; Zhou, H.; Huang, J.; Guo, Z. Review on the recent development of durable superhydrophobic materials for practical applications. *Nanoscale* **2021**, *13*, 11734–11764. [CrossRef]

120. Wang, D.; Sun, Q.; Hokkanen, M.J.; Zhang, C.; Lin, F.-Y.; Liu, Q.; Zhu, S.-P.; Zhou, T.; Chang, Q.; He, B. Design of robust superhydrophobic surfaces. *Nature* **2020**, *582*, 55–59. [CrossRef]

121. Li, J.; Du, F.; Liu, X.; Jiang, Z.; Ren, L. Superhydrophobicity of Bionic Alumina Surfaces Fabricated by Hard Anodizing. *J. Bionic Eng.* **2011**, *8*, 369–374. [CrossRef]

122. Zhao, D.; Tian, Q.; Wang, M.; Jin, Y. Study on the Hydrophobic Property of Shark-Skin-Inspired Micro-Riblets. *J. Bionic Eng.* **2014**, *11*, 296–302. [CrossRef]

123. Najafian, H.; Manteghi, F.; Beshkar, F.; Salavati-Niasari, M. Efficient degradation of azo dye pollutants on ZnBi38O58 nanostructures under visible-light irradiation. *Sep. Purif. Technol.* **2018**, *195*, 30–36. [CrossRef]

124. Sun, X.; Yang, S.; Xue, B.; Huo, K.; Li, X.; Tian, Y.; Liao, X.; Xie, L.; Qin, S.; Xu, K. Super-hydrophobic poly (lactic acid) by controlling the hierarchical structure and polymorphic transformation. *Chem. Eng. J.* **2020**, *397*, 125297. [CrossRef]

125. Wang, X.; He, Y.; Liu, X.; Zhu, J. Synthesis of hierarchical flower-like particles and its application as super-hydrophobic coating. *Powder Technol.* **2017**, *319*, 408–414. [CrossRef]

126. Zhang, X.; Lin, D.; Liu, Z.; Yuan, S.; Wang, X.; Wang, H.; Wang, J. Fabrication of mechanically stable UV-curing superhydrophobic coating by interfacial strengthening strategy. *J. Alloys Compd.* **2021**, *886*, 161156. [CrossRef]

127. Shi, L.; Hu, J.; Lin, X.; Fang, L.; Wu, F.; Xie, J.; Meng, F. A robust superhydrophobic PPS-PTFE/SiO$_2$ composite coating on AZ31 Mg alloy with excellent wear and corrosion resistance properties. *J. Alloys Compd.* **2017**, *721*, 157–163. [CrossRef]

128. Yu, Z.; Zhou, C.; Liu, R.; Zhang, Q.; Gong, J.; Tao, D.; Ji, Z. Fabrication of superhydrophobic surface with enhanced corrosion resistance on H62 brass substrate. *Colloids Surf. A Physicochem. Eng. Asp.* **2020**, *589*, 124475. [CrossRef]

129. Peng, K.; Hu, J.; Yan, Y.; Wu, Y.; Fang, H.; Xu, Y.; Lee, S.; Zhu, J. Fabrication of single-crystalline silicon nanowires by scratching a silicon surface with catalytic metal particles. *Adv. Funct. Mater.* **2006**, *16*, 387–394. [CrossRef]

130. Werner, J.H.; Dassow, R.; Rinke, T.; Köhler, J.; Bergmann, R. From polycrystalline to single crystalline silicon on glass. *Thin Solid Film.* **2001**, *383*, 95–100. [CrossRef]

131. Nositschka, W.; Beneking, C.; Voigt, O.; Kurz, H. Texturisation of multicrystalline silicon wafers for solar cells by reactive ion etching through colloidal masks. *Sol. Energy Mater. Sol. Cells* **2003**, *76*, 155–166. [CrossRef]

132. Macdonald, D.; Cuevas, A.; Kerr, M.J.; Samundsett, C.; Ruby, D.; Winderbaum, S.; Leo, A. Texturing industrial multicrystalline silicon solar cells. *Sol. Energy* **2004**, *76*, 277–283. [CrossRef]

133. Niinobe, D.; Morikawa, H.; Hiza, S.; Sato, T.; Matsuno, S.; Fujioka, H.; Katsura, T.; Okamoto, T.; Hamamoto, S.; Ishihara, T. Large-size multi-crystalline silicon solar cells with honeycomb textured surface and point-contacted rear toward industrial production. *Sol. Energy Mater. Sol. Cells* **2011**, *95*, 49–52. [CrossRef]

134. Chang, Z.; Sun, Y.; Xu, J.; Zong, X.; Tang, Q.; Guo, L.; Ren, L.; Cheng, W.-H. Hydrophobic nanostructures fabricated by ferric nitrate etching method on single crystalline silicon surface. *Colloids Surf. A Physicochem. Eng. Asp.* **2019**, *583*, 123999. [CrossRef]

135. Kamal, S.A.A.; Ritikos, R.; Rahman, S.A. Wetting behaviour of carbon nitride nanostructures grown by plasma enhanced chemical vapour deposition technique. *Appl. Surf. Sci.* **2015**, *328*, 146–153. [CrossRef]

136. Kamal, S.A.A.; Ritikos, R.; Rahman, S.A. Enhancement of self-cleaning properties and durability of super-hydrophobic carbon nitride nanostructures by post-annealing treatment. *Surf. Coat. Technol.* **2021**, *409*, 126912. [CrossRef]

137. Fan, G.; Li, F. Effect of sodium borohydride on growth process of controlled flower-like nanostructured Cu_2O/CuO films and their hydrophobic property. *Chem. Eng. J.* **2011**, *167*, 388–396. [CrossRef]

138. Yin, Y.; Alivisatos, A.P. Colloidal nanocrystal synthesis and the organic–inorganic interface. *Nature* **2005**, *437*, 664–670. [CrossRef] [PubMed]

139. Wang, D.; Lieber, C.M. Lieber, Nanocrystals branch out. *Nat. Mater.* **2003**, *2*, 355–356. [CrossRef] [PubMed]

140. Wang, Z.L. Self-assembled nanoarchitectures of polar nanobelts/nanowires. *J. Mater. Chem.* **2005**, *15*, 1021–1024. [CrossRef]

141. Burda, C.; Chen, X.; Narayanan, R.; El-Sayed, M.A. Chemistry and properties of nanocrystals of different shapes. *Chem. Rev.* **2005**, *105*, 1025–1102. [CrossRef]

142. Xia, Y.; Yang, P.; Sun, Y.; Wu, Y.; Mayers, B.; Gates, B.; Yin, Y.; Kim, F.; Yan, H. One-dimensional nanostructures: Synthesis; characterization; applications. *Adv. Mater.* **2003**, *15*, 353–389. [CrossRef]

143. Rhodes, K.H.; Davis, S.A.; Caruso, F.; Zhang, B.; Mann, S. Hierarchical assembly of zeolite nanoparticles into ordered macroporous monoliths using core—Shell building blocks. *Chem. Mater.* **2000**, *12*, 2832–2834. [CrossRef]

144. Kim, F.; Kwan, S.; Akana, J.; Yang, P. Langmuir—Blodgett nanorod assembly. *J. Am. Chem. Soc.* **2001**, *123*, 4360–4361. [CrossRef]

145. Fan, X.; Meng, X.M.; Zhang, X.H.; Shi, W.S.; Zhang, W.J.; Zapien, J.A.; Lee, C.S.; Lee, S.T. Dart-Shaped Tricrystal ZnS Nanoribbons. *Angew. Chem.* **2006**, *118*, 2630–2633. [CrossRef]

146. Tiwari, J.N.; Tiwari, R.N.; Kim, K.S. Zero-dimensional, one-dimensional, two-dimensional and three-dimensional nanostructured materials for advanced electrochemical energy devices. *Prog. Mater. Sci.* **2012**, *57*, 724–803. [CrossRef]

147. Chen, Z.; Cao, M. Synthesis, characterization, and hydrophobic properties of Bi2S3 hierarchical nanostructures. *Mater. Res. Bull.* **2011**, *46*, 555–562. [CrossRef]

148. Park, B.; Hwang, W. A facile fabrication method for corrosion-resistant micro/nanostructures on stainless steel surfaces with tunable wettability. *Scr. Mater.* **2016**, *113*, 118–121. [CrossRef]

149. Ryu, J.; Kim, K.; Park, J.; Hwang, B.G.; Ko, Y.; Kim, H.; Han, J.; Seo, E.; Park, Y.; Lee, S.J. Nearly perfect durable superhydrophobic surfaces fabricated by a simple one-step plasma treatment. *Sci. Rep.* **2017**, *7*, 1–8. [CrossRef] [PubMed]

150. Yang, Y.; Shen, H.; Qiu, J. Fabrication of biomimetic robust self-cleaning superhydrophobic wood with canna-leaf-like micro/nanostructure through morph-genetic method improved water-, UV-, and corrosion resistance properties. *J. Mol. Struct.* **2020**, *1219*, 128616. [CrossRef]

151. Meng, A.; Tian, W.; Wang, Y.; Zhang, M.; Li, Z.; Li, Q.; Tan, S. Wicker-like SiC@graphene multidimensional nanostructures and their robust stable super-hydrophobic property against harsh conditions for self-cleaning application. *Mater. Charact.* **2021**, *179*, 111389. [CrossRef]

152. Zhao, J.; Li, Z.; Zhang, M.; Meng, A. Super-hydrophobic surfaces of SiO_2-coated SiC nanowires: Fabrication, mechanism and ultraviolet-durable super-hydrophobicity. *J. Colloid Interface Sci.* **2015**, *444*, 33–37. [CrossRef]

153. Chen, H.; Zheng, X.; Jiang, Q.; Li, X. Hydrophobic Modified Nanosized Crosslinked Polymer Microspheres. *Asian J. Chem.* **2014**, *26*, 5412–5414. [CrossRef]

154. Haas, K.-H.; Rose, K. Hybrid inorganic/organic polymers with nanoscale building blocks: Precursors, processing, properties and applications. *Rev. Adv. Mater. Sci.* **2003**, *5*, 47–52.

155. Ponnupandian, S.; Chakrabarty, A.; Mondal, P.; Hoogenboom, R.; Lowe, A.B.; Singha, N.K. POSS and fluorine containing nanostructured block copolymer; Synthesis via RAFT polymerization and its application as hydrophobic coating material. *Eur. Polym. J.* **2020**, *131*, 109679. [CrossRef]

156. Sabbah, A.; Vandeparre, H.; Brau, F.; Damman, P. Self-Cleaning Surfaces Prepared By Microstructuring System. *Phys. Procedia* **2011**, *21*, 193–197. [CrossRef]

157. Leese, H.; Bhurtun, V.; Lee, K.P.; Mattia, D. Wetting behaviour of hydrophilic and hydrophobic nanostructured porous anodic alumina. *Colloids Surf. A Physicochem. Eng. Asp.* **2013**, *420*, 53–58. [CrossRef]

158. He, R.; Liu, S.; Wang, R.; Fu, T.; Zhang, R.; Zhang, Q.; Zhou, Y. In situ modification of melamine sponge by MgAl-LDH with super-hydrophobicity and excellent harsh environment tolerance for high flux emulsion separation. *Sep. Purif. Technol.* **2022**, *291*, 120916. [CrossRef]

159. Zhao, J.; Deng, Y.; Dai, M.; Wu, Y.; Ali, I.; Peng, C. Preparation of super-hydrophobic/super-oleophilic quartz sand filter for the application in oil-water separation. *J. Water Process Eng.* **2022**, *46*, 102561. [CrossRef]

160. Lv, C.; Liao, X.; Zou, F.; Tang, W.; Xing, S.; Li, G. Generating porous polymer microspheres with cellular surface via a gas-diffusion confined scCO2 foaming technology to endow the super-hydrophobic coating with hierarchical roughness. *Chem. Eng. J.* **2022**, *442*, 136192. [CrossRef]

161. Li, X.; Wang, J.; You, J.; Yu, P.; Li, X.; Xue, G.; Chen, H.; Xu, X.; van Agtmaal, S.; Alvarez, P.J.J. Hazardous waste dewatering and dry mass reduction through hydrophobic modification by a facile one-pot, alkali-assisted hydrothermal reaction. *Water Res.* **2019**, *155*, 225–232. [CrossRef]

162. Wang, G.; Song, D.; Qiao, Y.; Cheng, J.; Liu, H.; Jiang, J.; Ma, A.; Ma, X. Developing super-hydrophobic and corrosion-resistant coating on magnesium-lithium alloy via one-step hydrothermal processing. *J. Magnes. Alloys* **2021**, *11*, 1422–1439. [CrossRef]

163. Wang, G.; Jiang, J.; Qiao, Y.; Gu, L.; Klu, E.E.; Gong, X.; Ma, A.; Song, D. Enhanced super-hydrophobicity and corrosion resistance of the one-step hydrothermal synthesized coating on the Mg-9Li alloy: Role of the solid-solution treated substrate. *J. Alloys Compd.* **2022**, *921*, 166044. [CrossRef]

164. Mezzourh, H.; Moumen, S.B.; Amjoud, M.; Mezzane, D.; El Amraoui, Y.; Marbati, B.; Lahmar, A.; Jouiad, M.; El Marssi, M. Effect of growth time on structural and surface properties of TiO_2 nanostructures deposited by single-step hydrothermal method. *Mater. Today Proc.* **2022**, *51*, 2053–2058. [CrossRef]

165. Li, M.; Su, Y.; Hu, J.; Yao, L.; Wei, H.; Yang, Z.; Zhang, Y. Hierarchically porous micro/nanostructured copper surfaces with enhanced antireflection and hydrophobicity. *Appl. Surf. Sci.* **2016**, *361*, 11–17. [CrossRef]

166. Barthwal, S.; Lee, B.; Lim, S.-H. Fabrication of robust and durable slippery anti-icing coating on textured superhydrophobic aluminum surfaces with infused silicone oil. *Appl. Surf. Sci.* **2019**, *496*, 143677. [CrossRef]

167. Tan, X.; Zhang, Y.; Liu, X.; Xi, S.; Yan, Z.; Liu, Z.; Shi, T.; Liao, G. Employing micro pyramidal holes and porous nanostructures for enhancing the durability of lubricant-infused surfaces in anti-icing. *Surf. Coat. Technol.* **2021**, *405*, 126568. [CrossRef]

168. Yang, L.; Shen, X.; Yang, Q.; Liu, J.; Wu, W.; Li, D.; Du, J.; Zhang, B.; Fan, S. Fabrication of biomimetic anisotropic super-hydrophobic surface with rice leaf-like structures by femtosecond laser. *Opt. Mater.* **2021**, *112*, 110740. [CrossRef]

169. Chen, H.; Zhang, P.; Zhang, L.; Liu, H.; Jiang, Y.; Zhang, D.; Han, Z.; Jiang, L. Continuous directional water transport on the peristome surface of Nepenthes alata. *Nature* **2016**, *532*, 85–89. [CrossRef] [PubMed]

170. Liu, Y.; Zhang, K.; Yao, W.; Liu, J.; Han, Z.; Ren, L. Bioinspired structured superhydrophobic and superoleophilic stainless steel mesh for efficient oil-water separation. *Colloids Surf. A Physicochem. Eng. Asp.* **2016**, *500*, 54–63. [CrossRef]

171. Liu, Y.; Liu, W.; Wang, G.; Huo, J.; Kong, H.; Wang, W.; Wang, D.; Song, Z. A facile one-step approach to superhydrophilic silica film with hierarchical structure using fluoroalkylsilane. *Colloids Surf. A Physicochem. Eng. Asp.* **2018**, *539*, 109–115. [CrossRef]

172. Guo, Z.; Liu, W.; Su, B.-L. Superhydrophobic surfaces: From natural to biomimetic to functional. *J. Colloid Interface Sci.* **2011**, *353*, 335–355. [CrossRef] [PubMed]

173. Hancock, M.J.; Sekeroglu, K.; Demirel, M.C. Bioinspired directional surfaces for adhesion, wetting, and transport. *Adv. Funct. Mater.* **2012**, *22*, 2223–2234. [CrossRef] [PubMed]

174. Yan, Z.; Liang, X.; Cotton, I.; Emersic, C. Suppression of surface charge on micro-and nano-structured superhydrophobic silicone rubber. *IEEE Trans. Dielectr. Electr. Insul.* **2018**, *25*, 1095–1102. [CrossRef]

175. Wang, G.; Zhou, J.; Wang, M.; Zhang, Y.; Zhang, Y.; He, Q. A superhydrophobic surface with aging resistance, excellent mechanical restorablity and droplet bounce properties. *Soft Matter* **2020**, *16*, 5514–5524. [CrossRef] [PubMed]

176. Ogbonna, V.E.; Popoola, P.I.; Popoola, O.M.; Adeosun, S.O. A comparative study on the failure analysis of field failed high voltage composite insulator core rods and recommendation of composite insulators: A review. *Eng. Fail. Anal.* **2022**, *138*, 106369. [CrossRef]

177. Francis, U.U.; Philip, A.N. Degradation of epoxy reinforced Banana fibers and eggshell particles hybrid composite high-voltage insulators via accelerated UV aging processes. *Chem. Data Collect.* **2022**, *38*, 100842. [CrossRef]

178. Ibrahim, M.E.; Selim, F.; Abd-Elhady, A.M. Partial discharge performance improvement of covered conductor (CC)/high voltage insulator based electrical distribution systems. *Electr. Power Syst. Res.* **2022**, *202*, 107601. [CrossRef]

179. Salem, A.A.; Abd-Rahman, R.; Ishak, M.T.B.; Lau, K.Y.; Abdul-Malek, Z.; Al-ameri, S.; Al-Gailani, S.A.; Ghoneim, S.S. Influence of contamination distribution in characterizing the flashover phenomenon on outdoor insulator. *Ain Shams Eng. J.* **2023**, *14*, 102249. [CrossRef]

180. Li, Y.; Jin, H.; Nie, S.; Zhang, P.; Gao, N. Dynamic behavior of water droplets and flashover characteristics on a superhydrophobic silicone rubber surface. *Appl. Phys. Lett.* **2017**, *110*, 201602. [CrossRef]

181. Lei, S.; Wang, F.; Fang, X.; Ou, J.; Li, W. Icing behavior of water droplets impinging on cold superhydrophobic surface. *Surf. Coat. Technol.* **2019**, *363*, 362–368. [CrossRef]

182. Peng, W.; Gou, X.; Qin, H.; Zhao, M.; Zhao, X.; Guo, Z. Creation of a multifunctional superhydrophobic coating for composite insulators. *Chem. Eng. J.* **2018**, *352*, 774–781. [CrossRef]

183. Peng, W.; Gou, X.; Qin, H.; Zhao, M.; Zhao, X.; Guo, Z. Robust Mg (OH) 2/epoxy resin superhydrophobic coating applied to composite insulators. *Appl. Surf. Sci.* **2019**, *466*, 126–132. [CrossRef]

184. Chen, L.; Guo, F.; Yang, T.; Hu, T.; Bennett, P.; Yang, Q.; Liu, D. Aging characteristics and self-healing properties of laser-textured superhydrophobic silicone rubber for composite insulators. *Polym. Degrad. Stab.* **2021**, *192*, 109693. [CrossRef]

185. Wang, G.; Li, A.; Li, K.; Zhao, Y.; Ma, Y.; He, Q. A fluorine-free superhydrophobic silicone rubber surface has excellent self-cleaning and bouncing properties. *J. Colloid Interface Sci.* **2021**, *588*, 175–183. [CrossRef] [PubMed]

186. Li, A.; Wang, G.; Ma, Y.; Zhao, C.; Zhang, F.; He, Q.; Zhang, F. Study on preparation and properties of superhydrophobic surface of RTV silicone rubber. *J. Mater. Res. Technol.* **2021**, *11*, 135–143. [CrossRef]

187. Boinovich, L.; Emelyanenko, A.M.; Pashinin, A.S. Analysis of long-term durability of superhydrophobic properties under continuous contact with water. *ACS Appl. Mater. Interfaces* **2010**, *2*, 1754–1758. [CrossRef]

188. Chen, J.; Dou, R.; Cui, D.; Zhang, Q.; Zhang, Y.; Xu, F.; Zhou, X.; Wang, J.; Song, Y.; Jiang, L. Robust prototypical anti-icing coatings with a self-lubricating liquid water layer between ice and substrate. *ACS Appl. Mater. Interfaces* **2013**, *5*, 4026–4030. [CrossRef]
189. Pike, W. Extreme warm frontal icing on 25 February 1994 causes an aircraft accident near Uttoxeter. *Meteorol. Appl.* **1995**, *2*, 273–279. [CrossRef]
190. Wenxuan, Y.; Yuan, Y.; Guoyong, L.; Bing, Z.; Rongkai, Y. The anti-icing/frosting aluminum surface with hydrangea-like micro/nano structure prepared by chemical etching. *Mater. Lett.* **2018**, *226*, 4–7. [CrossRef]
191. Kraj, A.G.; Bibeau, E.L. Phases of icing on wind turbine blades characterized by ice accumulation. *Renew. Energy* **2010**, *35*, 966–972. [CrossRef]
192. Momen, G.; Jafari, R.; Farzaneh, M. Ice repellency behaviour of superhydrophobic surfaces: Effects of atmospheric icing conditions and surface roughness. *Appl. Surf. Sci.* **2015**, *349*, 211–218. [CrossRef]
193. Kong, L.; Li, Y.; Kong, X.; Ji, Z.; Wang, X.; Zhang, X. A novel flexible and fluoride-free superhydrophobic thermal energy storage coating for photothermal energy conversion. *Compos. Part B Eng.* **2022**, *232*, 109588. [CrossRef]
194. Zhang, Y.; Zhang, Z.; Yang, J.; Yue, Y.; Zhang, H. Fabrication of superhydrophobic surface on stainless steel by two-step chemical etching. *Chem. Phys. Lett.* **2022**, *797*, 139567. [CrossRef]
195. Zhu, P.; Zhu, L.; Ge, F.; Wang, G.; Zeng, Z. Sprayable superhydrophobic coating with high mechanical/chemical robustness and anti-corrosion. *Surf. Coat. Technol.* **2022**, *443*, 128609. [CrossRef]
196. Hellstén, P.P.; Salminen, J.M.; Jørgensen, K.S.; Nystén, T.H. Use of potassium formate in road winter deicing can reduce groundwater deterioration. *Environ. Sci. Technol.* **2005**, *39*, 5095–5100. [CrossRef] [PubMed]
197. Yin, X.; Yang, K.; Zhang, H.; Xiong, B.; Duan, M.; Wang, M.; Hao, Y. Important Explorations on Surface Corrosion of the Copper Coins Sourced from the Qing Dynasty. *Scanning* **2022**, *2022*, 1647217. [CrossRef] [PubMed]
198. Wang, G.; Shen, Y.; Tao, J.; Luo, X.; Jin, M.; Xie, Y.; Li, Z.; Guo, S. Facilely constructing micro-nanostructure superhydrophobic aluminum surface with robust ice-phobicity and corrosion resistance. *Surf. Coat. Technol.* **2017**, *329*, 224–231. [CrossRef]
199. Zhou, H.; Jing, X.; Guo, Z. Excellent fog droplets collector via an extremely stable hybrid hydrophobic-hydrophilic surface and Janus copper foam integrative system with hierarchical micro/nanostructures. *J. Colloid Interface Sci.* **2020**, *561*, 730–740. [CrossRef]
200. Shen, Y.; Wu, Y.; Tao, J.; Zhu, C.; Chen, H.; Wu, Z.; Xie, Y. Spraying fabrication of durable and transparent coatings for anti-icing application: Dynamic water repellency, icing delay, and ice adhesion. *ACS Appl. Mater. Interfaces* **2018**, *11*, 3590–3598. [CrossRef]
201. Xiong, J.; Sarkar, D.K.; Chen, X.-G. Superhydrophobic honeycomb-like cobalt stearate thin films on aluminum with excellent anti-corrosion properties. *Appl. Surf. Sci.* **2017**, *407*, 361–370. [CrossRef]
202. Ishizaki, T.; Saito, N. Rapid formation of a superhydrophobic surface on a magnesium alloy coated with a cerium oxide film by a simple immersion process at room temperature and its chemical stability. *Langmuir* **2010**, *26*, 9749–9755. [CrossRef] [PubMed]
203. Ishizaki, T.; Masuda, Y.; Sakamoto, M. Corrosion resistance and durability of superhydrophobic surface formed on magnesium alloy coated with nanostructured cerium oxide film and fluoroalkylsilane molecules in corrosive NaCl aqueous solution. *Langmuir* **2011**, *27*, 4780–4788. [CrossRef] [PubMed]
204. Wang, P.; Zhang, D.; Qiu, R.; Hou, B. Super-hydrophobic film prepared on zinc as corrosion barrier. *Corros. Sci.* **2011**, *53*, 2080–2086. [CrossRef]
205. Liu, T.; Yin, Y.; Chen, S.; Chang, X.; Cheng, S. Super-hydrophobic surfaces improve corrosion resistance of copper in seawater. *Electrochim. Acta* **2007**, *52*, 3709–3713. [CrossRef]
206. Ishizaki, T.; Sakamoto, M. Facile formation of biomimetic color-tuned superhydrophobic magnesium alloy with corrosion resistance. *Langmuir* **2011**, *27*, 2375–2381. [CrossRef] [PubMed]
207. Wang, J.; Li, D.; Liu, Q.; Yin, X.; Zhang, Y.; Jing, X.; Zhang, M. Fabrication of hydrophobic surface with hierarchical structure on Mg alloy and its corrosion resistance. *Electrochim. Acta* **2010**, *55*, 6897–6906. [CrossRef]
208. Liang, J.; Hu, Y.; Wu, Y.; Chen, H. Facile formation of superhydrophobic silica-based surface on aluminum substrate with tetraethylorthosilicate and vinyltriethoxysilane as co-precursor and its corrosion resistant performance in corrosive NaCl aqueous solution. *Surf. Coat. Technol.* **2014**, *240*, 145–153. [CrossRef]
209. Zheng, S.; Li, C.; Fu, Q.; Xiang, T.; Hu, W.; Wang, J.; Ding, S.; Liu, P.; Chen, Z. Fabrication of a micro-nanostructured superhydrophobic aluminum surface with excellent corrosion resistance and anti-icing performance. *Rsc Adv.* **2016**, *6*, 79389–79400. [CrossRef]
210. Seckler, D.W. *World Water Demand and Supply, 1990 to 2025: Scenarios and Issues*; International Water Management Institute (IWMI): Colombo, Sri Lanka, 1998; Volume 19.
211. Seckler, D.; Barker, R.; Amarasinghe, U. Water scarcity in the twenty-first century. *Int. J. Water Resour. Dev.* **1999**, *15*, 29–42. [CrossRef]
212. Chakraborti, R.K.; Kaur, J.; Kaur, H. Water shortage challenges and a way forward in India. *J. -Am. Water Work. Assoc.* **2019**, *111*, 42–49. [CrossRef]
213. Zheng, Y.; Bai, H.; Huang, Z.; Tian, X.; Nie, F.-Q.; Zhao, Y.; Zhai, J.; Jiang, L. Directional water collection on wetted spider silk. *Nature* **2010**, *463*, 640–643. [CrossRef] [PubMed]
214. Yang, J.-L.; Song, Y.-Y.; Zhang, X.; Zhang, Z.-Q.; Cheng, G.-G.; Liu, Y.; Lv, G.-J.; Ding, J.-N. Research progress of bionic fog collection surfaces based on special structures from natural organisms. *RSC Adv.* **2023**, *13*, 27839–27864. [CrossRef] [PubMed]

215. Song, D.; Bhushan, B. Optimization of bioinspired triangular patterns for water condensation and transport. *Philos. Trans. R. Soc. A* **2019**, *377*, 20190127. [CrossRef] [PubMed]

216. Peng, Y.; He, Y.; Yang, S.; Ben, S.; Cao, M.; Li, K.; Liu, K.; Jiang, L. Magnetically induced fog harvesting via flexible conical arrays. *Adv. Funct. Mater.* **2015**, *25*, 5967–5971. [CrossRef]

217. Song, K.; Kim, G.; Oh, S.; Lim, H. Enhanced water collection through a periodic array of tiny holes in dropwise condensation. *Appl. Phys. Lett.* **2018**, *112*, 71602. [CrossRef]

218. Zhong, L.; Zhu, H.; Wu, Y.; Guo, Z. Understanding how surface chemistry and topography enhance fog harvesting based on the superwetting surface with patterned hemispherical bulges. *J. Colloid Interface Sci.* **2018**, *525*, 234–242. [CrossRef] [PubMed]

219. Andrews, H.; Eccles, E.; Schofield, W.; Badyal, J. Three-dimensional hierarchical structures for fog harvesting. *Langmuir* **2011**, *27*, 3798–3802. [CrossRef] [PubMed]

220. Lu, Y.; Yu, L.; Zhang, Z.; Wu, S.; Li, G.; Wu, P.; Hu, Y.; Li, J.; Chu, J.; Wu, D. Biomimetic surfaces with anisotropic sliding wetting by energy-modulation femtosecond laser irradiation for enhanced water collection. *RSC Adv.* **2017**, *7*, 11170–11179. [CrossRef]

221. Lu, Y. Superior lubrication properties of biomimetic surfaces with hierarchical structure. *Tribol. Int.* **2018**, *119*, 131–142. [CrossRef]

222. Zhao, Y.; Su, Y.; Hou, X.; Hong, M. Directional sliding of water: Biomimetic snake scale surfaces. *Opto-Electron. Adv.* **2021**, *4*, 21000801–21000812. [CrossRef]

223. Stratakis, E.; Bonse, J.; Heitz, J.; Siegel, J.; Tsibidis, G.D.; Skoulas, E.; Papadopoulos, A.; Mimidis, A.; Joel, A.C.; Comanns, P.; et al. Laser engineering of biomimetic surfaces. *Mater. Sci. Eng. R Rep.* **2020**, *141*, 100562. [CrossRef]

224. Niu, Z.; Zhao, Y.; Sun, W.; Shi, S.; Gong, Y. Biomimetic surface modification of polypropylene by surface chain transfer reaction based on mussel-inspired adhesion technology and thiol chemistry. *Appl. Surf. Sci.* **2016**, *386*, 41–50. [CrossRef]

225. He, B.; Du, Y.; Wang, B.; Wang, X.; Ye, Q.; Liu, S. Grafting embedded poly(ionic liquid) brushes on biomimetic sharklet resin surface for anti-biofouling applications. *Prog. Org. Coat.* **2021**, *157*, 106298. [CrossRef]

226. Zhao, S.; Du, H.; Ma, Z.; Xiao, G.; Liu, J.; Jiang, Y.; Hu, S.; Zhao, H.; Wen, C.; Ren, L. Efficient fabrication of ternary coupling biomimetic superhydrophobic surfaces with superior performance of anti-wetting and self-cleaning by a simple two-step method. *Mater. Des.* **2022**, *223*, 111145. [CrossRef]

227. Song, Y.; Liu, Y.; Jiang, H.; Zhang, Y.; Han, Z.; Ren, L. Biomimetic super hydrophobic structured graphene on stainless steel surface by laser processing and transfer technology. *Surf. Coat. Technol.* **2017**, *328*, 152–160. [CrossRef]

228. Hwang, J.-J.; Wu, C.-Y.; Hung, Y.-H.; Li, M.-X.; Luo, K.-H.; Jia, H.-W.; Balitaan, J.N.I.; Lin, S.-R.; Yeh, J.-M. Biomimetic PMMA coating surface and its application on inhibition of bacterial attachment and anti-biofilm performance. *Surf. Interfaces* **2023**, *36*, 102548. [CrossRef]

229. Zhang, H.; Gan, J.; Wu, Y.; Wu, Z. Biomimetic high water adhesion superhydrophobic surface via UV nanoimprint lithography. *Appl. Surf. Sci.* **2023**, *633*, 157610. [CrossRef]

230. Wang, Z.; Han, L.; Zhou, Y.; Cai, J.; Sun, S.; Ma, J.; Wang, W.; Li, X.; Ma, L. The combination of a 3D-Printed porous Ti–6Al–4V alloy scaffold and stem cell sheet technology for the construction of biomimetic engineered bone at an ectopic site. *Mater. Today Bio* **2022**, *16*, 100433. [CrossRef] [PubMed]

231. Li, X.; Deng, J.; Yue, H.; Ge, D.; Zou, X. Wear performance of electrohydrodynamically atomized WS2 coatings deposited on biomimetic shark-skin textured surfaces. *Tribol. Int.* **2019**, *134*, 240–251. [CrossRef]

232. Deng, W.; Liu, Y.; Rui, Y.; Lu, G.; Liu, J. Construction of superhydrophobic surfaces via dual-scale modified particles and digital light processing 3D printing techniques. *Prog. Org. Coat.* **2023**, *181*, 107570. [CrossRef]

233. Li, G.; Tan, L.; Ren, L.; Zheng, A.; Li, Y.; He, Z.; Wang, K.; Han, Z.; Liu, Q.; Wu, W.; et al. Biomimetic 4D printing of dome-shaped dynamic mechanical metamaterials. *J. Mater. Res. Technol.* **2023**, *24*, 4047–4059. [CrossRef]

234. Pugliese, R.; Graziosi, S. Biomimetic scaffolds using triply periodic minimal surface-based porous structures for biomedical applications. *SLAS Technol.* **2023**, *28*, 165–182. [CrossRef] [PubMed]

235. Xu, J.; Zhang, X.; Dai, J.; Yu, D.; Ji, M.; Chen, M. Biomimetic microtextured surfaces to improve tribological and antibacterial behaviors of 3Y-TZP ceramics. *J. Mater. Res. Technol.* **2023**, *23*, 1360–1374. [CrossRef]

236. Ismail, M.F.; Azmi, W.H.; Mamat, R.; Ali, H.M. Thermal and Tribological Properties Enhancement of PVE Lubricant Modified with SiO2 and TiO2 Nanoparticles Additive. *Nanomaterials* **2023**, *13*, 42. [CrossRef] [PubMed]

237. Pan, C.; Gu, Y.; Chang, J.; Wang, C. Recent Patents on Friction and Wear Tester. *Recent Pat. Eng.* **2023**, *17*, 86–102. [CrossRef]

238. Afonso, I.S.; Nobrega, G.; Lima, R.; Gomes, J.R.; Ribeiro, J.E. Conventional and Recent Advances of Vegetable Oils as Metalworking Fluids (MWFs): A Review. *Lubricants* **2023**, *11*, 160. [CrossRef]

239. Xu, X.; Guo, P.; Tiong, L.C.O.; Zuo, X.; Li, X.; Lee, K.-R.; Cui, P.; Ke, P.; Wang, A. Role of dimple textured surface on tribological properties of Ti/Al-codoped diamond-like carbon films. *Thin Solid Film.* **2020**, *708*, 138136. [CrossRef]

240. Tong, J.; Liu, S.; Peng, R.; Sun, H.; Jiang, S. Development of a micro/nano composite super-hydrophobic silicon surface with nail-shaped texture/dual self-assembly monolayers and its wetting behavior. *Appl. Surf. Sci.* **2021**, *544*, 148803. [CrossRef]

241. Hamilton, D.B.; Walowit, J.A.; Allen, C.M. A Theory of Lubrication by Microirregularities. *J. Basic Eng.* **1966**, *88*, 177–185. [CrossRef]

242. Gyawali, G.; Joshi, B.; Tripathi, K.; Kim, S.-H.; Lee, S.W. Effect of microtexturing on tribological performance of Ni/Ni–SiC composite coatings. *Surf. Eng.* **2015**, *31*, 701–707. [CrossRef]

243. Vlădescu, S.-C.; Medina, S.; Olver, A.V.; Pegg, I.G.; Reddyhoff, T. The transient friction response of a laser-textured, reciprocating contact to the entrainment of individual pockets. *Tribol. Lett.* **2016**, *62*, 19. [CrossRef]

244. Xu, D.; Wu, W.; Malhotra, R.; Chen, J.; Lu, B.; Cao, J. Mechanism investigation for the influence of tool rotation and laser surface texturing (LST) on formability in single point incremental forming. *Int. J. Mach. Tools Manuf.* **2013**, *73*, 37–46. [CrossRef]

245. Nakano, M.; Korenaga, A.; Korenaga, A.; Miyake, K.; Murakami, T.; Ando, Y.; Usami, H.; Sasaki, S. Applying micro-texture to cast iron surfaces to reduce the friction coefficient under lubricated conditions. *Tribol. Lett.* **2007**, *28*, 131–137. [CrossRef]

246. Maldonado-Cortés, D.; Peña-Parás, L.; Barrios-Saldaña, V.; Cruz-Bañuelos, J.S.; Adamiak, M. Synergistic effect on the tribological properties of tool steel through the use of laser surface texturing channels and nanoparticles. *Wear* **2019**, *426–427*, 1354–1361. [CrossRef]

247. Fleming, R.A.; Zou, M. The effects of confined core volume on the mechanical behavior of Al/a-Si core-shell nanostructures. *Acta Mater.* **2017**, *128*, 149–159. [CrossRef]

248. Steck, J.G.; Afshar-Mohajer, M.; Sun, Q.; Meng, X.; Zou, M. Fabrication and tribological characterization of deformation-resistant nano-textured surfaces produced by two-photon lithography and atomic layer deposition. *Tribol. Int.* **2019**, *132*, 75–84. [CrossRef]

249. Qian, M.; Xu, X.; Qin, Z.; Yan, S. Silicon carbide whiskers enhance mechanical and anti-wear properties of PA6 towards potential applications in aerospace and automobile fields. *Compos. Part B Eng.* **2019**, *175*, 107096. [CrossRef]

250. Suarez, S.; Rosenkranz, A.; Gachot, C.; Mücklich, F. Enhanced tribological properties of MWCNT/Ni bulk composites–Influence of processing on friction and wear behaviour. *Carbon* **2014**, *66*, 164–171. [CrossRef]

251. Reinert, L.; Suárez, S.; Rosenkranz, A. Tribo-mechanisms of carbon nanotubes: Friction and wear behavior of CNT-reinforced nickel matrix composites and CNT-coated bulk nickel. *Lubricants* **2016**, *4*, 11. [CrossRef]

252. Li, C.; Wang, Y.; Pan, Z. Wear resistance enhancement of electroless nanocomposite coatings via incorporation of alumina nanoparticles prepared by milling. *Mater. Des.* **2013**, *47*, 443–448. [CrossRef]

253. Gu, D.; Zhang, H.; Dai, D.; Xia, M.; Hong, C.; Poprawe, R. Laser additive manufacturing of nano-TiC reinforced Ni-based nanocomposites with tailored microstructure and performance. *Compos. Part B Eng.* **2019**, *163*, 585–597. [CrossRef]

254. Alizadeh, M.; Safaei, H. Characterization of Ni-Cu matrix, Al_2O_3 reinforced nano-composite coatings prepared by electrodeposition. *Appl. Surf. Sci.* **2018**, *456*, 195–203. [CrossRef]

255. Yang, K.; Shi, X.; Zou, J.; Shen, Q.; Zhai, W.; Huang, Y. The study of the preparation and tribological behavior of TiAl matrix composites containing 1 wt% multi-walled carbon nanotubes. *RSC Adv.* **2016**, *6*, 29334–29341. [CrossRef]

256. Deore, H.A.; Mishra, J.; Rao, A.G.; Mehtani, H.; Hiwarkar, V.D. Effect of filler material and post process ageing treatment on microstructure, mechanical properties and wear behaviour of friction stir processed AA 7075 surface composites. *Surf. Coat. Technol.* **2019**, *374*, 52–64. [CrossRef]

257. Huang, S.J.; Abbas, A.; Ballóková, B. Effect of CNT on microstructure, dry sliding wear and compressive mechanical properties of AZ61 magnesium alloy. *J. Mater. Res. Technol.* **2019**, *8*, 4273–4286. [CrossRef]

258. Chen, W.X.; Li, F.; Han, G.; Xia, J.B.; Wang, L.Y.; Tu, J.P.; Xu, Z.D. Tribological behavior of carbon-nanotube-filled PTFE composites. *Tribol. Lett.* **2003**, *15*, 275–278. [CrossRef]

259. Wu, H.; Zhu, L.N.; Yue, W.; Fu, Z.Q.; Kang, J.J. Wear-resistant and hydrophobic characteristics of PTFE/CF composite coatings. *Prog. Org. Coat.* **2019**, *128*, 90–98. [CrossRef]

260. Shi, Y.J.; Feng, X.; Wang, H.Y.; Lu, X.H. The effect of surface modification on the friction and wear behavior of carbon nanofiber-filled PTFE composites. *Wear* **2008**, *264*, 934–939. [CrossRef]

261. Baghdadchi, A.; Movahedi, M. Consumable pin-friction stir spot welding of Al-Mg-Si alloy via pre-created hole and refilling: Microstructure evolution, defects, and shear/tensile failure load. Proceedings of the Institution of Mechanical Engineers. *Part C J. Mech. Eng. Sci.* **2023**, *237*, 3861–3870. [CrossRef]

262. Dawari, C.K.; Haq, I.; Mönkkönen, K.; Suvanto, M.; Saarinen, J.J. Reduced sliding friction on flat and microstructured metal injection molded (MIM) WC-Co hard metals with MoS_2 composite lubricants. *Tribol. Int.* **2021**, *160*, 107020. [CrossRef]

263. Chen, L.; Liu, Z.; Shen, Q. Enhancing tribological performance by anodizing micro-textured surfaces with nano-MoS_2 coatings prepared on aluminum-silicon alloys. *Tribol. Int.* **2018**, *122*, 84–95. [CrossRef]

264. Li, X.; Deng, J.; Zhang, L.; Liu, Y.; Yue, H.; Duan, R.; Ge, D. Effect of surface textures and electrohydrodynamically atomized WS_2 films on the friction and wear properties of ZrO_2 coatings. *Ceram. Int.* **2019**, *45*, 1020–1030. [CrossRef]

265. Shi, Z.; Shum, P.; Wasy, A.; Zhou, Z.; Li, L.K.-Y. Tribological performance of few layer graphene on textured M2 steel surfaces. *Surf. Coat. Technol.* **2016**, *296*, 164–170. [CrossRef]

266. Xing, Y.; Wu, Z.; Yang, J.; Wang, X.; Liu, L. LIPSS combined with ALD MoS_2 nano-coatings for enhancing surface friction and hydrophobic performances. *Surf. Coat. Technol.* **2020**, *385*, 125396. [CrossRef]

267. Lu, G.; Shi, X.; Liu, X.; Zhou, H.; Chen, Y.; Yang, Z.; Huang, Y. Tribological performance of functionally gradient structure of graphene nanoplatelets reinforced Ni_3Al metal matrix composites prepared by laser melting deposition. *Wear* **2019**, *428–429*, 417–429. [CrossRef]

268. Liu, Q.-S.; Liu, X.-B.; Wang, G.; Liu, Y.-F.; Meng, Y.; Zhang, S.-H. Effect of Cu content on microstructure evolution and tribological behaviors of Ni60 composite coatings on 45# steel by laser cladding. *Opt. Laser Technol.* **2022**, *156*, 108549.

269. Wu, H.Y.; Gu, Z.B.; Lei, Y.; Li, Q.F.; Gong, C.J.; Shao, S.F.; Rao, W.F. Effects of Pt cylinder arrays on macro-tribological properties of graphene and the SiO_2/Si substrate. *Wear* **2015**, *332–333*, 1314–1321. [CrossRef]

270. Chen, S.; Qian, G.; Yang, L. Precise control of surface texture on carbon film by ion etching through filter: Optimization of texture size for improving tribological behavior. *Surf. Coat. Technol.* **2019**, *362*, 105–112. [CrossRef]

271. Ovchinnikov, S.; Kalashnikov, M. Structure and tribological properties of gradient-layered coatings (Ti, Al, Si, Cr, Mo, S) O, N. *Surf. Coat. Technol.* **2021**, *408*, 126807. [CrossRef]

272. Wu, G.; Xu, C.; Xiao, G.; Yi, M.; Chen, Z. Structure design of Al$_2$O$_3$/TiC/CaF$_2$ multicomponent gradient self-lubricating ceramic composite and its tribological behaviors. *Ceram. Int.* **2018**, *44*, 5550–5563. [CrossRef]

273. Naebe, M.; Shirvanimoghaddam, K. Functionally graded materials: A review of fabrication and properties. *Appl. Mater. Today* **2016**, *5*, 223–245. [CrossRef]

274. Carroll, B.E.; Otis, R.A.; Borgonia, J.P.; Suh, J.-O.; Dillon, R.P.; Shapiro, A.A.; Hofmann, D.C.; Liu, Z.-K.; Beese, A.M. Functionally graded material of 304L stainless steel and inconel 625 fabricated by directed energy deposition: Characterization and thermodynamic modeling. *Acta Mater.* **2016**, *108*, 46–54. [CrossRef]

275. Fakhrabadi, E.A.; Stickel, J.J.; Liberatore, M.W. Frictional contacts between individual woody biomass particles under wet and dry conditions. *Powder Technol.* **2022**, *408*, 117719. [CrossRef]

276. Tikanmäki, M.; Sainio, P. Experiments on friction of dry and wet ice. *Cold Reg. Sci. Technol.* **2020**, *172*, 102990. [CrossRef]

277. Hamilton, D.; Walowit, J.; Allen, C. A Theory of Lubrication by Micro-irregularities. In Proceedings of the ASME-ASLE Lubrication Conference; 1966.

278. Sreejith, P.; Ngoi, B. Dry machining: Machining of the future. *J. Mater. Process. Technol.* **2000**, *101*, 287–291. [CrossRef]

279. Costa, H.; Hutchings, I. Hydrodynamic lubrication of textured steel surfaces under reciprocating sliding conditions. *Tribol. Int.* **2007**, *40*, 1227–1238. [CrossRef]

280. Zhou, L.; Kato, K.; Umehara, N.; Miyake, Y. Nanometre scale island-type texture with controllable height and area ratio formed by ion-beam etching on hard-disk head sliders. *Nanotechnology* **1999**, *10*, 363. [CrossRef]

281. Kovalchenko, A.; Ajayi, O.; Erdemir, A.; Fenske, G.; Etsion, I. The effect of laser surface texturing on transitions in lubrication regimes during unidirectional sliding contact. *Tribol. Int.* **2005**, *38*, 219–225. [CrossRef]

282. Wu, B.; Qin, D.; Hu, J.; Liu, Y. Experimental data mining research on factors influencing friction coefficient of wet clutch. *J. Tribol.* **2021**, *143*, 121802. [CrossRef]

283. Wang, X.; Liu, J.; Wang, Y.; Fu, Y. Fabrication of friction-reducing texture surface by selective laser melting of ink-printed (SLM-IP) copper (Cu) nanoparticles(NPs). *Appl. Surf. Sci.* **2017**, *396*, 659–664. [CrossRef]

284. Wang, M.; Wang, X.; Liu, J.; Wei, J.; Shen, Z.; Wang, Y. 3-Dimensional ink printing of friction-reducing surface textures from copper nanoparticles. *Surf. Coat. Technol.* **2019**, *364*, 57–62. [CrossRef]

285. Zhou, L.; Fu, Y.; Yin, T.; Tian, X.; Qi, L. Building the silicon carbide nanowire network on the surface of carbon fibers: Enhanced interfacial adhesion and high-performance wear resistance. *Ceram. Int.* **2019**, *45*, 22571–22577. [CrossRef]

286. Moghadam, A.D.; Omrani, E.; Menezes, P.L.; Rohatgi, P.K. Mechanical and tribological properties of self-lubricating metal matrix nanocomposites reinforced by carbon nanotubes (CNTs) and graphene–A review. *Compos. Part B Eng.* **2015**, *77*, 402–420. [CrossRef]

287. Vail, J.R.; Burris, D.L.; Sawyer, W.G. Multifunctionality of single-walled carbon nanotube–polytetrafluoroethylene nanocomposites. *Wear* **2009**, *267*, 619–624. [CrossRef]

288. Kumar, R.M.; Sharma, S.K.; Kumar, B.V.M.; Lahiri, D. Effects of carbon nanotube aspect ratio on strengthening and tribological behavior of ultra high molecular weight polyethylene composite. *Compos. Part A Appl. Sci. Manuf.* **2015**, *76*, 62–72. [CrossRef]

289. Otitoju, T.A.; Okoye, P.U.; Chen, G.; Li, Y.; Okoye, M.O.; Li, S. Advanced ceramic components: Materials; fabrication; applications. *J. Ind. Eng. Chem.* **2020**, *85*, 34–65. [CrossRef]

290. Candelario, V.M.; Moreno, R.; Guiberteau, F.; Ortiz, A.L. Enhancing the sliding-wear resistance of SiC nanostructured ceramics by adding carbon nanotubes. *J. Eur. Ceram. Soc.* **2016**, *36*, 3083–3089. [CrossRef]

291. Jung, Y.C.; Bhushan, B. Contact angle; adhesion, and friction properties of micro- and nanopatterned polymers for superhydrophobicity. *Nanotechnol. Nanotechnol.* **2006**, *17*, 4970. [CrossRef]

292. Amiri, M.; Khonsari, M.M. On the thermodynamics of friction and wear—A review. *Entropy* **2010**, *12*, 1021–1049. [CrossRef]

293. Scharf, T.; Prasad, S. Solid lubricants: A review. *J. Mater. Sci.* **2013**, *48*, 511–531. [CrossRef]

294. Jin, B.; Zhao, J.; He, Y.; Chen, G.; Li, Y.; Zhang, C.; Luo, J. High-quality ultra-flat reduced graphene oxide nanosheets with super-robust lubrication performances. *Chem. Eng. J.* **2022**, *438*, 135620. [CrossRef]

295. Chhattal, M.; Kaihuan, Y.; Ali, S.; Zambrano, D.F.; Rosenkranz, A.; Grützmacher, P.G.; Gong, Z.; Zhang, J. Solid Lubrication Performance of Ti2CTx Coatings with Reduced Friction and Extended Durability. *Tribol. Int.* **2024**, *194*, 109535. [CrossRef]

296. Erdemir, A.; Ramirez, G.; Eryilmaz, O.L.; Narayanan, B.; Liao, Y.; Kamath, G.; Sankaranarayanan, S.K. Carbon-based tribofilms from lubricating oils. *Nature* **2016**, *536*, 67–71. [CrossRef] [PubMed]

297. Zhang, B.; Xue, Y.; Qiang, L.; Gao, K.; Liu, Q.; Yang, B.; Liang, A.; Zhang, J. Assembling of carbon nanotubes film responding to significant reduction wear and friction on steel surface. *Appl. Nanosci.* **2017**, *7*, 835–842. [CrossRef]

298. Ahmad, H.; Tamil, T. High responsivity, self-powered carbon–zinc oxide hybrid thin film based photodetector. *Appl. Nanosci.* **2018**, *8*, 1755–1765. [CrossRef]

299. Scagliotti, M.; Salvato, M.; De Crescenzi, M.; Boscardin, M.; Castrucci, P. Influence of the contact geometry on single-walled carbon nanotube/Si photodetector response. *Appl. Nanosci.* **2018**, *8*, 1053–1058. [CrossRef]

300. Robertson, J. Diamond-like amorphous carbon. *Mater. Sci. Eng. R Rep.* **2002**, *37*, 129–281. [CrossRef]

301. Erdemir, A.; Donnet, C. Tribology of diamond-like carbon films: Recent progress and future prospects. *J. Phys. D Appl. Phys.* **2006**, *39*, R311. [CrossRef]

302. Charitidis, C. Nanomechanical and nanotribological properties of carbon-based thin films: A review. *Int. J. Refract. Met. Hard Mater.* **2010**, *28*, 51–70. [CrossRef]

303. Bewilogua, K.; Hofmann, D. History of diamond-like carbon films—From first experiments to worldwide applications. *Surf. Coat. Technol.* **2014**, *242*, 214–225. [CrossRef]

304. Argibay, N.; Babuska, T.; Curry, J.; Dugger, M.; Lu, P.; Adams, D.; Nation, B.; Doyle, B.; Pham, M.; Pimentel, A. In-situ tribochemical formation of self-lubricating diamond-like carbon films. *Carbon* **2018**, *138*, 61–68. [CrossRef]

305. Arcieri, E.V.; Baragetti, S. Impact of DLC Coating Deposition on the Fatigue Strength of Al-7075-T6 Aluminum Alloy. *J. Mater. Sci. Technol. Res.* **2023**, *10*, 12–18. [CrossRef]

306. Song, R.; Chen, S.; Liu, Z.; Huo, C.; Chen, Q. Effect of W-doping on the structure and properties of DLC films prepared by combining physical and chemical vapor deposition. *Diam. Relat. Mater.* **2023**, *132*, 109687. [CrossRef]

307. Rawian, N.A.M.; Akasaka, H.; Liza, S.; Fukuda, K.; Zulkifli, N.A.; Tahir, N.A.M.; Yaakob, Y. Surface and tribological characterization of anodic aluminum oxide coating containing diamond-like carbon flakes. *Diam. Relat. Mater.* **2023**, *132*, 109674. [CrossRef]

308. Cao, Z.; Zhao, W.; Liang, A.; Zhang, J. A general engineering applicable superlubricity: Hydrogenated amorphous carbon film containing nano diamond particles. *Adv. Mater. Interfaces* **2017**, *4*, 1601224. [CrossRef]

309. Wang, Z.; Gong, Z.; Zhang, B.; Wang, Y.; Gao, K.; Zhang, J.; Liu, G. Heating induced nanostructure and superlubricity evolution of fullerene-like hydrogenated carbon films. *Solid State Sci.* **2019**, *90*, 29–33. [CrossRef]

310. Gong, Z.; Jia, X.; Ma, W.; Zhang, B.; Zhang, J. Hierarchical structure graphitic-like/MoS$_2$ film as superlubricity material. *Appl. Surf. Sci.* **2017**, *413*, 381–386. [CrossRef]

311. Li, R.; Yang, X.; Hou, D.; Wang, Y.; Zhang, J. Superlubricity of carbon nanostructural films enhanced by graphene nanoscrolls. *Mater. Lett.* **2020**, *271*, 127748. [CrossRef]

312. Martin, J.-M. Superlubricity of molybdenum disulfide. In *Superlubricity*; Elsevier: Amsterdam, The Netherlands, 2007; pp. 207–225.

313. Chhowalla, M.; Amaratunga, G.A. Thin films of fullerene-like MoS$_2$ nanoparticles with ultra-low friction and wear. *Nature* **2000**, *407*, 164–167. [CrossRef]

314. Jiang, J.-W.; Park, H.S. Mechanical properties of MoS$_2$/graphene heterostructures. *Appl. Phys. Lett.* **2014**, *105*, 33108. [CrossRef]

315. Liu, Z.; Yang, J.; Grey, F.; Liu, J.Z.; Liu, Y.; Wang, Y.; Yang, Y.; Cheng, Y.; Zheng, Q. Observation of microscale superlubricity in graphite. *Phys. Rev. Lett.* **2012**, *108*, 205503. [CrossRef] [PubMed]

316. Chen, X.; Li, J. Superlubricity of carbon nanostructures. *Carbon* **2020**, *158*, 1–23. [CrossRef]

317. Nurmi, H.A.; Yu, C.; Toptunov, D.; Ras, R.H.A.; Jokinen, V. Superhydrophobic Lubrication: Gas–Liquid Bilayer Reduces the Friction Between Two Solids. *Adv. Mater. Interfaces* **2022**, *9*, 2102132. [CrossRef]

318. Urbakh, M.; Klafter, J.; Gourdon, D.; Israelachvili, J. The nonlinear nature of friction. *Nature* **2004**, *430*, 525–528. [CrossRef] [PubMed]

319. Koster, D.A.; Croquette, V.; Dekker, C.; Shuman, S.; Dekker, N.H. Friction and torque govern the relaxation of DNA supercoils by eukaryotic topoisomerase IB. *Nature* **2005**, *434*, 671–674. [CrossRef] [PubMed]

320. Bowden, F.P.; Bowden, F.P.; Tabor, D. *The Friction and Lubrication of Solids*; Oxford University Press: Oxford, UK, 2001; Volume 1.

321. Alazemi, A.A.; Dysart, A.D.; Phuah, X.L.; Pol, V.G.; Sadeghi, F. MoS$_2$ nanolayer coated carbon spheres as an oil additive for enhanced tribological performance. *Carbon* **2016**, *110*, 367–377. [CrossRef]

322. Liu, S.; Gao, Q.; Hou, K.; Li, Z.; Wang, J.; Yang, S. Solvent-free covalent MXene nanofluid: A new lubricant combining the characteristics of solid and liquid lubricants. *Chem. Eng. J.* **2023**, *462*, 142238. [CrossRef]

323. Ahmed, A.; Masjuki, H.; Varman, M.; Kalam, M.; Habibullah, M.; Al Mahmud, K. An overview of geometrical parameters of surface texturing for piston/cylinder assembly and mechanical seals. *Meccanica* **2016**, *51*, 9–23. [CrossRef]

324. Shen, C.; Khonsari, M. Numerical optimization of texture shape for parallel surfaces under unidirectional and bidirectional sliding. *Tribol. Int.* **2015**, *82*, 1–11. [CrossRef]

325. Kligerman, Y.; Etsion, I.; Shinkarenko, A. Improving tribological performance of piston rings by partial surface texturing. *J. Trib.* **2005**, *127*, 632–638. [CrossRef]

326. Borghi, A.; Gualtieri, E.; Marchetto, D.; Moretti, L.; Valeri, S. Tribological effects of surface texturing on nitriding steel for high-performance engine applications. *Wear* **2008**, *265*, 1046–1051. [CrossRef]

327. Pillari, L.K.; Lessoway, K.; Bichler, L. Reciprocating dry sliding friction and wear behavior of B319 aluminum alloy-graphene composites. *Tribol. Int.* **2024**, *192*, 109334. [CrossRef]

328. Guo, W.; Bai, Q.; Deng, K.; Dou, Y.; Wang, T.; Wang, H. Comparison of lubrication mechanism and friction behavior of graphene on stainless steel substrate at different scales. *Appl. Surf. Sci.* **2024**, *649*, 159192. [CrossRef]

329. Zhang, Z.; Guo, Y.; Han, F.; Wang, D.; Zhang, S. Multilayer graphene for reducing friction and wear in water-based sand cleaning liquid. *Wear* **2021**, *470*, 203619. [CrossRef]

330. Flamina, A.; Raghavendra, R.; Gupta, A.; Subramaniam, A. Hydrogen storage in Nickel dispersed boron doped reduced graphene oxide. *Appl. Surf. Sci. Adv.* **2023**, *13*, 100371. [CrossRef]

331. Siochi, E.J.; Harrison, J.S. Structural nanocomposites for aerospace applications. *MRS Bull.* **2015**, *40*, 829–835. [CrossRef]

332. Dumitrica, T.; Hua, M.; Yakobson, B.I. Symmetry-, time-, and temperature-dependent strength of carbon nanotubes. *Proc. Natl. Acad. Sci. USA* **2006**, *103*, 6105–6109. [CrossRef] [PubMed]

333. Jin, L.; Bower, C.; Zhou, O. Alignment of carbon nanotubes in a polymer matrix by mechanical stretching. *Appl. Phys. Lett.* **1998**, *73*, 1197–1199. [CrossRef]

334. Wang, H.; Liu, Y.; Li, J.; Luo, J. Investigation of superlubricity achieved by polyalkylene glycol aqueous solutions. *Adv. Mater. Interfaces* **2016**, *3*, 1600531. [CrossRef]

335. Zhang, C.; Liu, Z.; Liu, Y.; Ren, J.; Cheng, Q.; Yang, C.; Cai, L. Novel tribological stability of the superlubricity poly (vinylphosphonic acid)(PVPA) coatings on Ti6Al4V: Velocity and load independence. *Appl. Surf. Sci.* **2017**, *392*, 19–26. [CrossRef]

336. Zhang, R.; Ning, Z.; Zhang, Y.; Zheng, Q.; Chen, Q.; Xie, H.; Zhang, Q.; Qian, W.; Wei, F. Superlubricity in centimetres-long double-walled carbon nanotubes under ambient conditions. *Nat. Nanotechnol.* **2013**, *8*, 912–916. [CrossRef] [PubMed]

337. Berman, D.; Deshmukh, S.A.; Sankaranarayanan, S.K.; Erdemir, A.; Sumant, A.V. Macroscale superlubricity enabled by graphene nanoscroll formation. *Science* **2015**, *348*, 1118–1122. [CrossRef] [PubMed]

338. Gong, Z.; Shi, J.; Zhang, B.; Zhang, J. Graphene nano scrolls responding to superlow friction of amorphous carbon. *Carbon* **2017**, *116*, 310–317. [CrossRef]

339. Erdemir, A.; Eryilmaz, O. Achieving superlubricity in DLC films by controlling bulk, surface, and tribochemistry. *Friction* **2014**, *2*, 140–155. [CrossRef]

340. Wang, C.; Yang, S.; Wang, Q.; Wang, Z.; Zhang, J. Super-low friction and super-elastic hydrogenated carbon films originated from a unique fullerene-like nanostructure. *Nanotechnology* **2008**, *19*, 225709. [CrossRef] [PubMed]

341. Gong, Z.; Shi, J.; Ma, W.; Zhang, B.; Zhang, J. Engineering-scale superlubricity of the fingerprint-like carbon films based on high power pulsed plasma enhanced chemical vapor deposition. *RSC Adv.* **2016**, *6*, 115092–115100. [CrossRef]

342. Teo, E.; Kulik, J.; Kauffmann, Y.; Kalish, R.; Lifshitz, Y. Nanostructured carbon films with oriented graphitic planes. *Appl. Phys. Lett.* **2011**, *98*, 123104. [CrossRef]

343. Liu, X.; Yang, J.; Hao, J.; Zheng, J.; Gong, Q.; Liu, W. A near-frictionless and extremely elastic hydrogenated amorphous carbon film with self-assembled dual nanostructure. *Adv. Mater.* **2012**, *24*, 4614–4617. [CrossRef]

344. Joly-Pottuz, L.; Bucholz, E.; Matsumoto, N.; Phillpot, S.; Sinnott, S.; Ohmae, N.; Martin, J. Friction properties of carbon nano-onions from experiment and computer simulations. *Tribol. Lett.* **2010**, *37*, 75–81. [CrossRef]